Growth and characterisation of quantum materials nanostructures

Piet Schönherr

Corpus Christi College

University of Oxford

A thesis submitted for the degree of

Doctor of Philosophy

Michaelmas 2016

If I had asked people what they wanted, they would have said faster horses.

—Henry Ford

Abstract

Research into new materials has been one of the driving forces that have contributed to the progress of civilisation from the Bronze Age four thousand years ago to the age of the semiconductor in the 20th century. At the turn to the 21st century novel materials, so-called *quantum materials*, started to emerge. The fundamental theories for the description of their properties were established at the beginning of the 20th century but expanded significantly during the last three decades based, for example, on a new interpretation of electronic states by topological invariants. Hence, topological insulator (TI) materials such as mercury-telluride are one manifestation of a *quantum material*. In theory, TIs are characterised by an insulating interior and a surface with spin-momentum locked conduction. In real crystals, however, the bulk can be conducting due to crystal imperfections. Nanowires suppress this bulk contribution inherently by their high surface-to-volume ratio. Additionally, trace impurity elements can be inserted into the crystal to decrease the conductance further. These optimised TI nanowires could provide building blocks for future electronic nanodevices such as transistors and sensors.

Initial synthesis efforts using vapour transport techniques and electronic transport studies showed that TI nanowires hold the promise of reduced bulk contribution. This thesis expands the current knowledge on synthesis strategies, crystal growth mechanisms, and new types of *quantum materials* nanowires. Traditionally, gold catalyst nanoparticles were used to grow TI nanowires. We demonstrate that they are suitable to produce large amounts of nanowires but have undesired side-effects. If a metal-oxide catalyst nanoparticle is used instead, quality and even quantity are significantly improved. This synthesis strategy was used to produce a new TI which is built from chains of atoms and not from atomic layers as in case of previously known TIs.

The growth of large nanowires with a layered crystal structure leads to step-flow growth,

an intriguing phenomenon in the growth mechanism: New layers grow on top of previous layers with a single growth front moving from the root to the tip. These wires are ideal for further electronic characterisation that requires large samples. The nanowire growth of tin-oxide will also be discussed, a side project that arose from my growth studies, which is useful for sensor applications. Under certain conditions it forms tree-like structures in a single synthesis step. All of the aforementioned growth studies are carried out at atmospheric pressure. A separate growth study is carried out in ultra-high vacuum to assess the transferability of the growth process towards the cleanliness requirements of the semiconductor industry.

If two *quantum materials* are joined together, exotic physics may emerge at the interface. One of the goals of TI research is the experimental observation of Majorana fermions, exotic particles which are their own antiparticles with potential applications in quantum computing that may appear in superconductor/TI hybrid structures. We have synthesised such structures and initial characterisation suggests that the resistivity increases when they are cooled below the critical temperature of the superconductor.

Beyond TIs, a new type of *quantum material*, called a topological Dirac semimetal, opens new realms of exotic physics to be discovered. Nanowires are grown from a material which has recently been discovered to be a topological Dirac semimetal. Their growth mechanism is characterised and an extremely high electron mobility at room temperature is measured.

The contribution of this thesis to the field is summarised in Fig. 1. Its core is the study of the growth mechanism of *quantum materials* which will be vital for future development of applications and fundamental research.

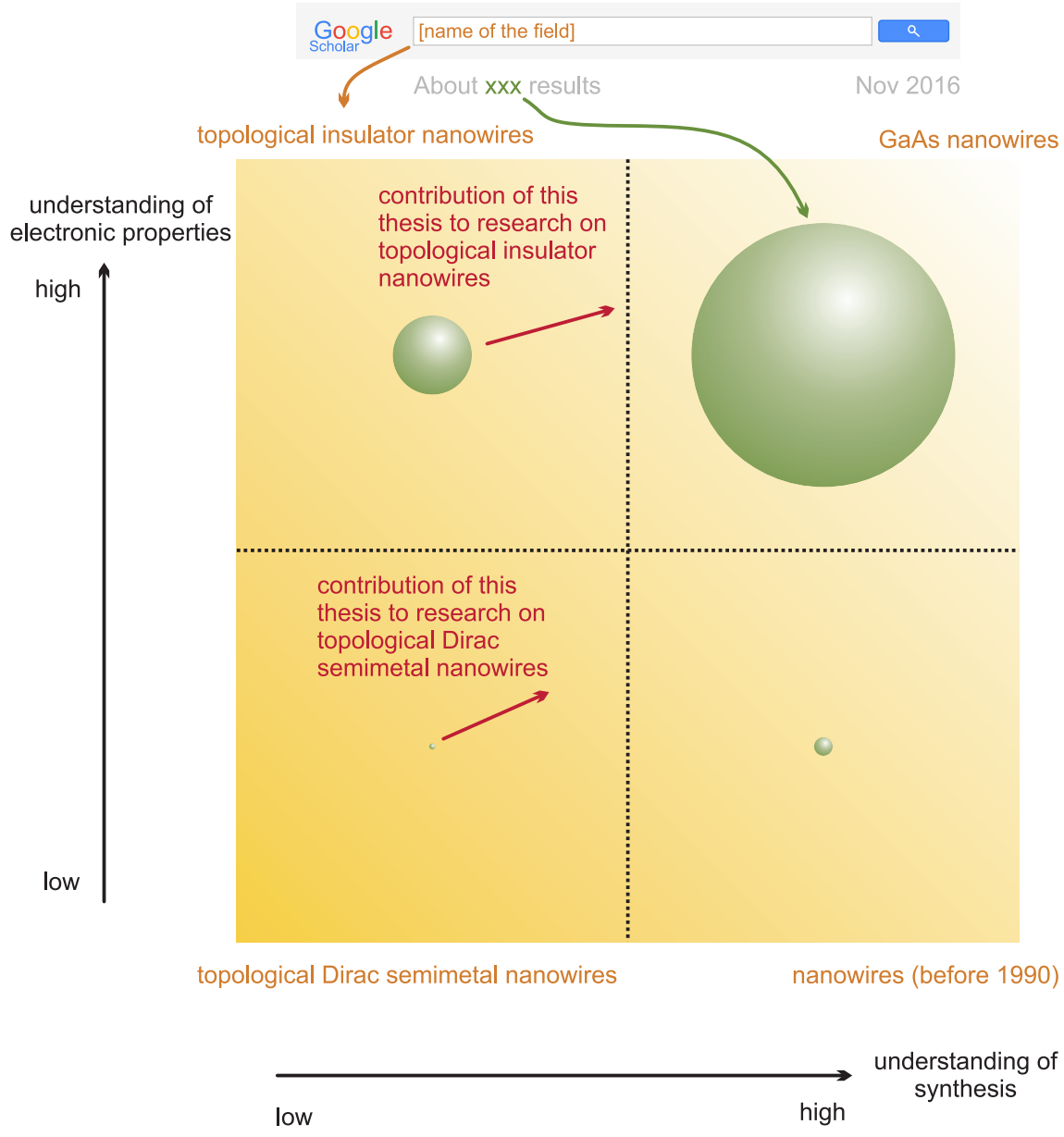

Fig. 1: GaAs is one of the most well understood nanowire systems in terms of materials synthesis and electronic properties. The number of publications found on Google Scholar using 'GaAs nanowires' as a search term is around 38 100. Relative to this field other nanowire systems are less well understood. In 1990, the more general term 'nanowire' only had 2 680 results. Topological insulator nanowires and topological Dirac semimetals which are the topic of this thesis are not very well understood in terms of synthesis yet. The contribution of this thesis to the two fields is indicated by red arrows.

Table of contents

1 Introduction

1.1 A short history of solid state physics

Solid state physics has influenced the 20th century unlike any other field of physics. A thrilling summary of the early days can be found in Hoddeson *et al.* [1]. Its roots are deeply connected with industrial research. Fundamental questions such as 'What is the difference between a metal and an insulator?' were answered by solid state physics. Accordingly, the demand for more research was huge and driven by industries such as the steel or lighting industry. Until that time science and technology were mainly independent and the number of physicists working in industry was small. Towards the end of the 19th century first research laboratories were founded and soon the majority of physicists was working in laboratories at companies such as Siemens or the Bell Telephone Company. Their main goal was the development of new materials and material testing methods.

What is called solid state physics nowadays was usually referred to as crystal physics during the early years. One of the central figures in its development was Max Born. In his book 'The Dynamics of Crystal Lattices' he developed a unified crystal theory including the mechanics and electrodynamics of crystal lattices [2].

A basic experiment to characterise materials was the measurement of heat capacity and resistance over temperature. Electrons add a factor to the heat capacity of metals which led to an understanding of these electrons as particles of an ideal gas that can move freely in the conduction band. Likewise, simple resistance measurements lead to the discovery of exciting new materials properties such as the huge difference in resistivity in metals and insulators. It was found that both materials conduct current more efficiently at low temperatures since electron scattering from phonons is decreased.

Silicon and germanium, however, showed the opposite behaviour. These new materials had a constant resistance until a critical temperature and their resistance de-

creased at high temperatures. Explanations were complicated by the fact that the critical temperature depended on the purity of the samples so it varied over different sets of samples of the same material. It was crucial to develop reliable methods for sample synthesis that ensured reproducible sample properties. The British physicist Alan Wilson suggested a model of electronic bands in 1931 which established Si-type materials as a new class between metals and insulators – the semiconductor [3].

Sixteen years later the first transistor was built from n-type doped germanium.[1] The advent of the semiconductor industry had begun. It shaped the 20$^{\text{th}}$ century, created millions of jobs, and influenced every other branch of industry from agriculture over car production to health services.

In the 21$^{\text{st}}$ century scientists will continue to study new materials, try to understand their physical properties, and predict potential applications. A broad current research effort is sub-summarised under the umbrella of *quantum materials* [4]. It includes emergent phenomena such as high temperature superconductivity, designer quantum matter such as cold atoms, and application of topology to electronic band theory. The topic of this thesis are two *quantum materials*, namely topological insulators (TIs) and topological Dirac semimetals, which are characterised by an intriguing electronic bandstructure due to topological effects. In principle any of these *quantum materials* has the potential to impact civilization to an extend semiconductors have done during the last century. Whether such materials are successful on their way from the discovery to an application crucially depends on the ability to provide high quality samples. Hence, fundamental research on the perfection of synthesis techniques is the vital enabling step.

[1] The p-type component arose from the surface treatment of the germanium bulk crystal. Brattain and Bardeen speculated about the nature of these surface states in a letter immediately following the cited paper.

1.2 Motivation

1.2.1 Spintronics

A study by a global leader in flash memory storage solutions suggests that a computer user in the UK spends an average of five working days per year waiting for their computer to perform the requested task [5]. It is certainly sensible to assume a digital downtime of a few minutes per day from checking emails in the morning to watching a video on Youtube in the evening. In other words, faster consumer electronics are essential to save time and to reduce stress in the digital age. The industry has been very successful in device development but the concept of the transistor has reached its limit with the demonstration of the single electron transistor [6]. Heat dissipation and quantum confinement are fundamental lines that cannot be crossed. Spintronics offers a new approach, e.g., by low-power transistors based on spin manipulation.

The initial impact from using the spin in electronic devices came from the discovery of giant magnetoresistance in the early 1980s, an effect that was subsequently used in read-head sensors for magnetic disk drives. The term spintronics was coined as an acronym for 'spin transport electronics'. It has three main branches [7]: optoelectronic devices, quantum spin effects (a branch leading towards quantum computing), and spin quantum devices (new devices based on existing semiconductor devices with the added value of the spin, e.g., polarised light-emitting diodes (LEDs) and transistors).

Spin-polarised materials are fundamental to make progress in creation, transport, manipulation, and detection of spin polarised currents. Examples include magnetic semiconductors that seek to combine the advantages of spin and charge properties of electrons in one material [8, 9], spin injection from a ferromagnetic material into a semiconductor [10], and more recently TIs that are naturally spin-polarised [11].

The ultimate goal for electronic devices is to have data processing and storage in one place in order to massively increase performance. In current computers data has to be uploaded from a permanent storage into the working memory – a process that takes unnecessary time. If the data was handled at the same location as it is stored, software would not have to be loaded at all and the computer would start up in the same state as it was left when shut down.

1.2.2 Majorana fermions

Besides bosons and fermions, non-Abelian systems form a third type of composite particle that is a zero-energy excitation with a degenerated ground state [12]. The creation or annihilation of such a state are identical operations called Majorana operators. So the particle is its own antiparticle. Originally, this concept was discovered by the particle physicist Ettore Majorana in 1937 as a purely real-valued solution to the Dirac equation. Now, solid state physicists have joined in the experimental quest with the ultimate goal to harness the Majorana fermion for quantum computing.

Experiments on semiconductor nanowires have shown evidence of Majorana modes but are not considered as a definitive proof of its existence because subsequent theoretical work pointed out more trivial explanations of the experimental results [13–15]. Broadly speaking the experimental setup requires a nanowire to be placed flat on a substrate prepared with gates and to be contacted from above by a metallic and a superconducting contact. Majorana particles are expected to appear at both ends of the wire under a small magnetic field applied along the wire axis. Their signature would be a zero-bias conductance peak. The biggest challenge to realise this system in semiconductor nanowires is that the chemical potential has to be adjusted with great accuracy to create the right topological phase. If a three-dimensional (3D) TI nanowire is used instead, however, this is not necessary [15]. Alternative approaches, e.g., by using thin films exist but progress has stagnated since the initial successes [16]. Ex-

perimental implementation of the nanowire approach is mainly hindered by the fact that nanowire growth of TI systems is still in its infancy compared to the growth of III-V semiconductor nanowires.

1.2.3 Thermoelectrics

A significant amount of energy is used in heaters, furnaces, and boilers. Waste heat of these system is usually discharged into the environment. Studies suggest that this amounts to 22.5% of the total energy produced [17]. Thermoelectric materials provide an avenue to generate power from waste heat based on the Seebeck effect [18,19]. The efficiency of this process is quantified by the figure of merit ZT which is a function of the electrical and thermal conductivity and the Seebeck coefficient of the thermoelectric material. Given that good electrical conductors are usually also good thermal conductors and vice-versa, it is hard to optimise materials with respect to their figure of merit. Hence, thermoelectric materials lack efficiency compared to the majority of energy generation technologies so that it is challenging for them to become economically viable despite decades of research. Engineered quantum materials nanostructures hold the promise to benefit this field by increasing the electrical conductivity and suppressing heat transfer at the same time [20,21].

1.2.4 Cancer treatment

According to the World Health Organisation 8.2 million deaths in 2012 worldwide were caused by cancer; researchers are challenged by a disease that is highly heterogeneous and adaptive [22]. It is imperative to constantly develop new diagnostic and therapeutic imaging capabilities in order to save lives. The integration of both as 'theranostics' combines definition of disease states and their treatment which is promising in the context of personalised medicine [23]. Nanoparticles are an efficient

platform for theranostics which outperforms single particle contrast agents and drug delivery systems. An example of such a nanoparticle is Bi_2Se_3 [24]. The role of the contrast agent is played by Bi which has a higher photoelectric absorption coefficient than iodinated contrast agents due to its high atomic number. The role of the therapeutic agent is taken by Se which is a trace element that is known to reduce the occurence of several types of cancers by inhibiting reactive oxygen species [25]. Zhang *et al.* demonstrated the low toxicity of Bi_2Se_3 on mice which opens potential applications for cancer treatment using Bi_2Se_3 nanoparticles in human medicine [26].

2 Quantum materials, nanowires, and nanowires of quantum materials

Introduction

Nanotechnology plays an important role in the research effort to realise the overarching goals described in Chapter 1. It comprises aspects from building to utilising functional structures with at least one dimension being on the nanoscale. Different physical laws rule at this scale compared to bulk materials. Nanowires are regarded as building blocks of future nanodevices such as sensors [27]. The combination of nanostructures and *quantum materials* is a less explored subfield which offers promising exciting physics and new applications. In the following, an introduction to *quantum materials* is given mainly based on Hasan and Kane's review of the field [28]; the growth methods for nanowires are described based on Hornyak *et al.* [29], Rao *et al.* [30], and Lieber *et al.* [31]; and the benefits of the combination of both worlds are discussed.

2.1 Quantum materials: treasures in band theory

The quantum Hall state was the first example of a condensed matter system that was explained using the concept of topology (Nobel Prize in Physics 2016 [32]). This discovery has inspired a research area that deals with a novel classification paradigm of phases of matter based on topological order. The field comprises the study of related materials, application of topology to band theory, and exotic physical phenomena. One of the most stunning outcomes of this has been the prediction and subsequent discovery of TIs in two and three dimensions [28]. These materials have an insulating bulk and metallic surface states protected by time-reversal symmetry which facilitate spin-momentum interlocked electronic transport without backscattering, as shown in Fig. 2.1.1(a,b). The search for new materials is still ongoing. More recent discoveries include topological Dirac semimetals, whose valence and conduction band meet in a single point, the Dirac point, which are shown in Fig. 2.1.1(c,d) [33, 34].

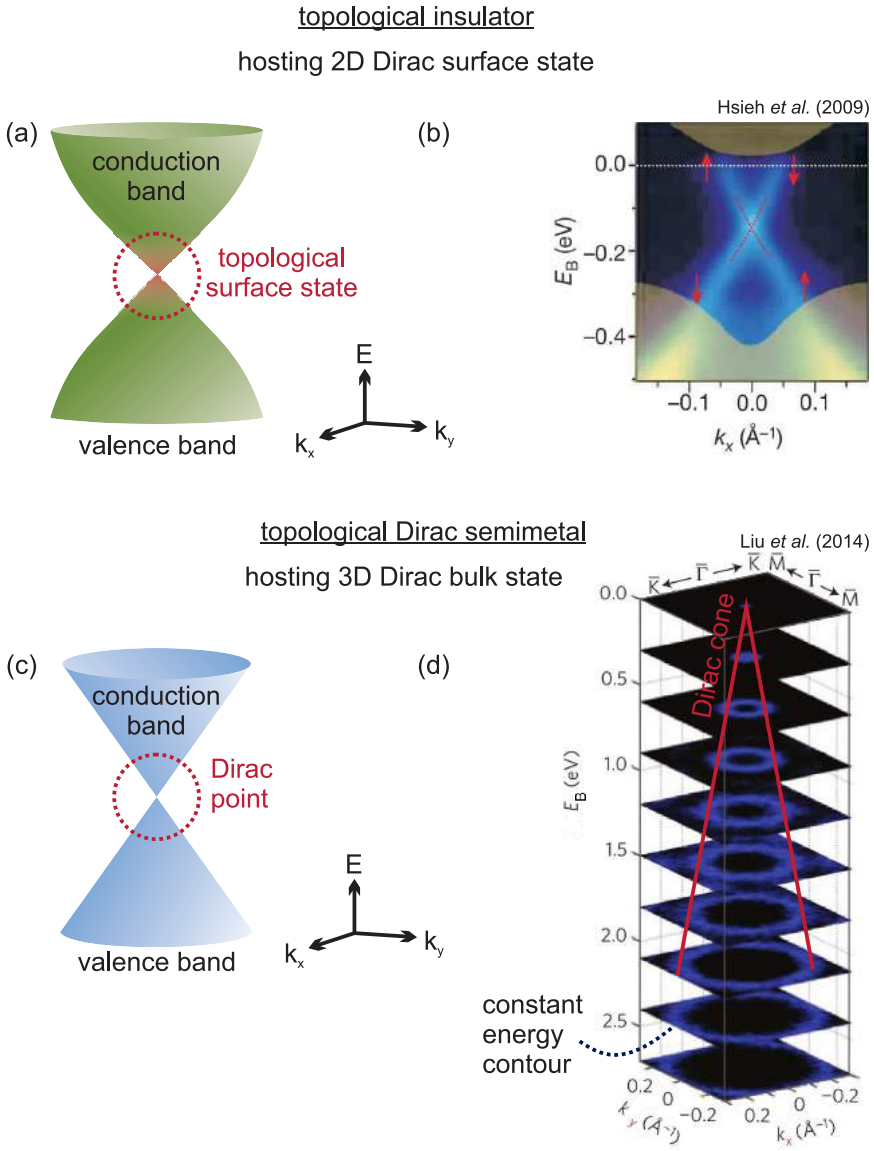

Fig. 2.1.1: TIs and topological Dirac semimetals belong to a new class of *quantum materials* that exhibits exotic electronic states. (a) The bandstructure of a TI hosts spin-momentum interlocked, linearly dispersing surface states inside the bandgap between the bulk valence and conduction band. (b) Direct experimental evidence of the spin-dependent topological surface states measured on the TI Bi_2Se_3. Image taken from Ref. [35]. (c) The conduction and valence band of a topological Dirac semimetal overlap in a single point – the Dirac point. (d) Direct experimental evidence of the Dirac cone in Cd_3As_2. Image taken from Ref. [34].

2.1.1 Topological insulators

TIs have a bandstructure which is topologically different from the bandstructure of an ordinary insulator. What is the relation between topology, a field of mathematics, and condensed matter physics? A topological classification is, e.g., the classification of objects by the number of holes. In this picture a sphere is in a different topological phase than a torus and there is no smooth deformation that could transform the sphere into a torus. The bandstructure of a TI is in the same sense *topologically different* from an ordinary insulator, hence the name.

The underlying physics of TIs can be conceptually understood with reference to the quantum Hall state. This state can be created in a two-dimensional (2D) electron gas at low temperatures by a strong magnetic field. The field forces the electrons onto cyclotron orbits. At the edges the orbits are not closed, as shown in Fig. 2.1.2(a), which leads to conducting edge channels that are illustrated in Fig. 2.1.2(b). One can imagine electronic carriers taking a 'detour' if impurities are present. Backscattering is forbidden. Note that conducting edge or surface states in a semiconductor are rather common. They could be caused by certain surface configurations of the crystal structure that lead to conducting surface electrons. Such configurations would, however, not be robust against surface doping. Quantum Hall states, on the other hand, exist purely due to the topology of the crystal.

The quantum Hall state is odd under time-reversal since the external magnetic field breaks time-reversal symmetry. This can be seen in Fig. 2.1.2(c): If the arrow of time is reversed the direction of motion of spin-up and spin-down electrons is reversed, too, because the magnetic field flips.

A system which is not odd under time reversal symmetry is a spin quantum Hall state system. It can be realised in 2D TIs and emerges from the interplay between strong spin-orbit coupling and the electronic spin. It can be thought of as two separate quan-

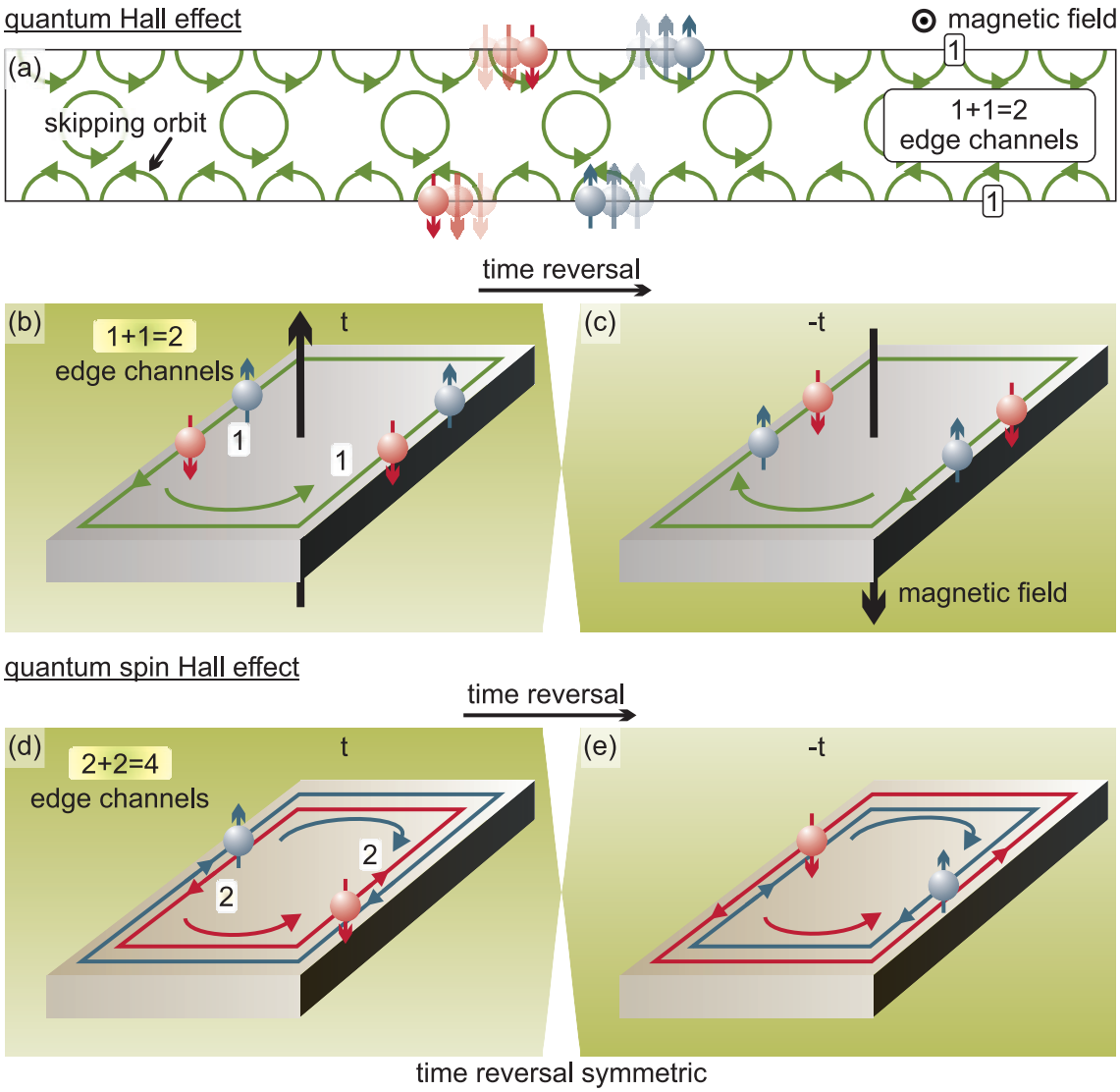

Fig. 2.1.2: (a) Illustration of electron localisation into cyclotron orbits and edge states that establish two lossless conducting channels in both directions (left and right). (b) In the quantum Hall effect spin-up and spin-down electrons both only occupy the counter-clockwise edge channel as required by the external magnetic field. (c) Upon time-reversal the electronic current flows clockwise. The magnetic field and spin are reversed. (d) In the quantum spin Hall effect the direction of the electronic current in the edge channels depends on the spin of the electrons. There are four edge channels. (e) Upon time-reversal the current direction in both channels is reversed and the spins flip. The system is time-reversal invariant.

tum Hall systems for spin-up and spin-down electrons whereby opposite spins travel in opposite directions, as shown in Fig. 2.1.2(d). One could argue that backscattering is possible now since there are states for a reversal of the direction of motion available if the spin flips. It is true that these scattering paths exist, as shown in Fig. 2.1.3, but they destructively interfere so that the probability of backscattering is zero [20].

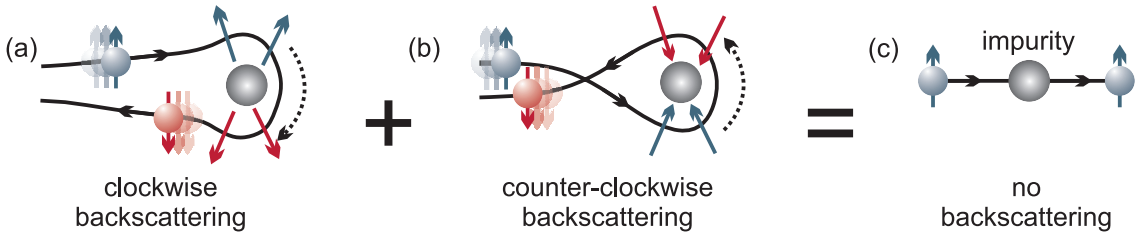

Fig. 2.1.3: A quantum spin Hall edge state has two paths available to backscatter from an impurity. (a) The clockwise path implies a rotation of the spin by $+\pi$; (b) the counter-clockwise path implies a rotation by $-\pi$. (c) The two paths interfere with each other destructively so that the overall probability for backscattering is zero. Picture adapted from Ref. [20].

Only a magnetic impurity would break time reversal symmetry, as shown for the external magnetic field for the quantum Hall effect in Fig. 2.1.2(c). Thus, the quantum spin Hall state is robust because of its time-reversal symmetry. If time is reversed, the system maps to itself, as shown in Fig. 2.1.2(e).

It should be clear now why the edge states of a quantum spin Hall state are metallic whilst the inside is an insulator. The spin-momentum interlock follows from time-reversal invariance via Kramers' theorem which states [28]:

$$E(\vec{k},\uparrow) = E(-\vec{k},\downarrow), \tag{2.1.1}$$

where $\vec{k}$ is the electronic wavevector, $\uparrow$ spin-up, $\downarrow$ spin-down, and E the energy of the electronic state. If the electron direction of motion is reversed ($\vec{k} \longrightarrow -\vec{k}$), the spin has to flip ($\uparrow \longrightarrow \downarrow$), while the energy of the electronic state stays the same. Kramers' theorem is not trivial for materials with a strong spin-orbit coupling since the energy of the electronic states may vary between up-spin and down-spin. A consequence of this is a characteristic linear dispersion with a time-reversal invariant crossing point.

The above considerations can be extended to include 3D TIs, bulk materials with metallic surface states that are protected by time-reversal symmetry. The dispersion of the topological surface states (TSSs) forms a Dirac cone in 3D with the direction of the electron spin locked to the electron momentum k_x and k_y, as shown above in Fig. 2.1.1(a). The representations of *quantum matter* can be arranged into a periodic table of TIs and superconductors compiled by Schnyder *et al.* which is a showcase of the richness of this newly emerging field [28, 36]. Note that a one-dimensional (1D) TI does not exist.

2.1.2 Materials and applications

The first experimental demonstration of a strong 2D TI as it was described above was in the form of HgTe/(Hg,Cd)Te quantum wells [37]. Later, the 3D TI phase was demonstrated in a Bi_xSb_{1-x} metal alloy [38]. TIs consisting of two elements with fixed atomic ratio (binary compounds) belong to the second generation of TI materials. The most well-studied representatives are Bi_2Te_3 [39, 40] and Bi_2Se_3 [35, 40], two small-bandgap, group V-VI semiconductors which exhibit a single Dirac cone on the surface [35]. Both are also well-known thermoelectric materials [41, 42]. Their unit cells are very similar with Se or Te at the respective positions in the lattice. Figure 2.1.4(a) shows the crystal structure of Bi_2Se_3 with its rhombohedral unit cell. Each layer consists of five Bi and Se atomic planes that are covalently bound in a stacking sequence Se-Bi-Se-Bi-Se (quintuple layer). Van der Waals interaction between Se layers bonds quintuple layers together. The conventional unit cell is formed of three quintuple layers, and has lattice parameters $a = 4.14$ Å and $c = 28.64$ Å. Bi_2Se_3 is well suited for TI research because of the TSS being almost ideal in the center of the bulk bandgap (see Fig. 2.1.4(b)), whereas the TSS of Bi_2Te_3 is close to the bulk valence band and therefore more challenging to investigate [28].

However, the dibismuth trichalcogenides are plagued by chalcogen vacancies lead-

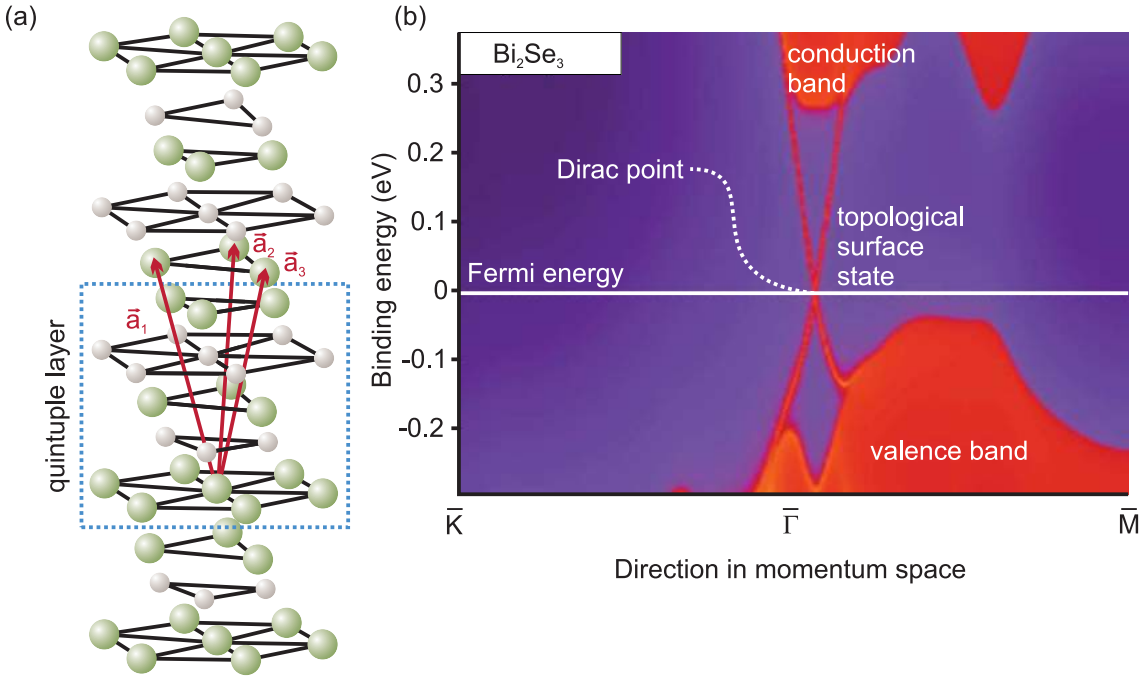

Fig. 2.1.4: (a) Layered crystal structure of Bi_2Se_3. Five atomic planes with the stacking sequence Se-Bi-Se-Bi-Se form a quintuple layer. The van-der-Waals force between the quintuple layers is responsible for their mutual interaction. Illustrated after Ref. [43]. (b) The bandstructure of Bi_2Se_3 shows linearly dispersing surface states in the bulk bandgap. Image adapted from Ref. [44].

ing to intrinsic n-type doping, and thus to an increase of the Fermi level above the Dirac point [45, 46]. Dopant atoms can be used to reduce the intrinsically high electron concentration. Sb doping was reported to suppress Se vacancies by substitution of Bi atoms [47] and lead to a reduced bulk carrier density from $n \approx 30 \cdot 10^{16}$ cm^{-3} to $n \approx 2.9 \cdot 10^{16}$ cm^{-3} [48]. Similar improvements are possible in nanowires although an orthogonal Sb_2Se_3 guest lattice is formed in the rhombohedral Bi_2Se_3 host crystal at a doping level of 10% Sb and no further substitution on Bi sites is possible [49, 50]. At this critical point the TI becomes a trivial insulator.

$Bi_2(Se_xTe_{1-x})_3$ is a ternary compound with a tetradymite structure that displays TI surface states [51]. The stoichiometric compositions Bi_2Te_2Se (BTS) and Bi_2Se_2Te (BST) have identical crystal structures [52, 53]. Ternary compounds have a lower bulk resistivity due to suppression of vacancies and antisite defects [54]. Accordingly Bi_2Se_2Te was recently found to have dominant topological surface transport properties [55].

A more exotic topological material is Ag_2Te, where a metastable topological phase can

be stabilised by strain [56]. Strain can also be used to open a bandgap in Bi_2Se_2 [34] and other topological materials such as α-Sn [57] and HgTe [58].

Recently, chemists synthesised the first weak TI, a 3D configuration that can be understood as a stack of 2D quantum spin Hall states [59, 60]. The discovery of quasi 1D TIs (in the sense of crystal structure) is an interesting extension to the periodic table of TIs and topological superconductors. They were observed in Sb-doped Bi_2Se_3 and β-Bi_4I_4 [61, 62]. Topological crystalline insulators represent another concept of topology that is protected by symmetry of the space group instead of time-reversal symmetry [63].

Topological Dirac semimetals are a 3D analogue to graphene with an even number of Dirac points and linearly dispersing states in all three dimensions of k-space, stabilised by crystal symmetry [64]. Dirac nodes can also be regarded as two overlapping Weyl nodes that have opposite chirality. In a Weyl semimetal they are separated by either breaking time-reversal symmetry or inversion symmetry which leads to characteristic Fermi arcs on the surface [65, 66].

2.2 Foundations of nanowire growth

Assembly methods are a particularly interesting side of nanotechnology. There seems to be a lot to learn considering how large a production facility has to be to produce a nanoscale electric circuit and how small an organism can be that produces the most intricate molecular machines.

Nanowires have been synthesised using a wide range of materials and techniques. Examples include elemental materials such as Si or Ag, metal compounds such as oxides or carbides, semiconductors such as the III-V compounds (GaAs, Cd_3As_2 etc), and metal chalcogenides. The geometry of these structures can be varied in terms of shape of the cross-section (e.g. hexagonal), width-to-height ratio (e.g. flat), and di-

mensions (e.g. one dimension on the nanoscale), whereby the nomenclature reflects this diversity. The term 'nanowire' is generally understood as a micron long wire with a circular cross-section on the nanoscale, i.e., 100-200 nm, as shown in Fig. 2.2.1(a). This term will be used throughout this thesis in the interest of readability although most of the objects it refers to do not have exactly these dimensions. In the literature some of them are labelled nanocables (Fig. 2.2.1(b); circular cross-section, diameter on the nanoscale, hundreds of microns long), nanoribbons (Fig. 2.2.1(c); rectangular cross-section, tens of nanometre thin, tens of nanometre broad, and several micron long ribbon-like structures) and sub-micron belts (Fig. 2.2.1(d); tens of nanometre thin, several micron broad, and hundreds of micron long).

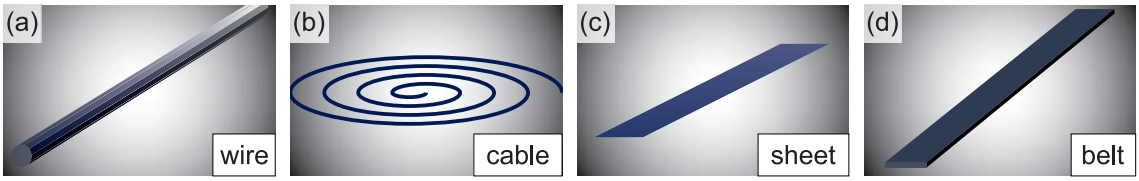

Fig. 2.2.1: Types of quasi-one dimensional structures are (a) wire, (b) cable, (c) sheet, and (d) belt.

2.2.1 Growth mechanisms

Nanowire production can broadly be divided into two methods: top-down and bottom-up synthesis. Top-down methods are more diverse than bottom-up methods as they include physical methods (aerosol), high-energy methods (laser ablation), lithographic methods (focused ion beam lithography), and also natural methods such as erosion [29]. As an example, laser ablation can be used for device engineering and to modify nanostructures after the growth is finished to remove unwanted residues. The basic idea is depicted in Fig. 2.2.2(a).

Bottom-up methods can be loosely categorised into gas, liquid, solid phase, and biological methods depending on the active medium or material. Examples for liquid and solid phase fabrication are single-crystal growth and scanning tunneling mi-

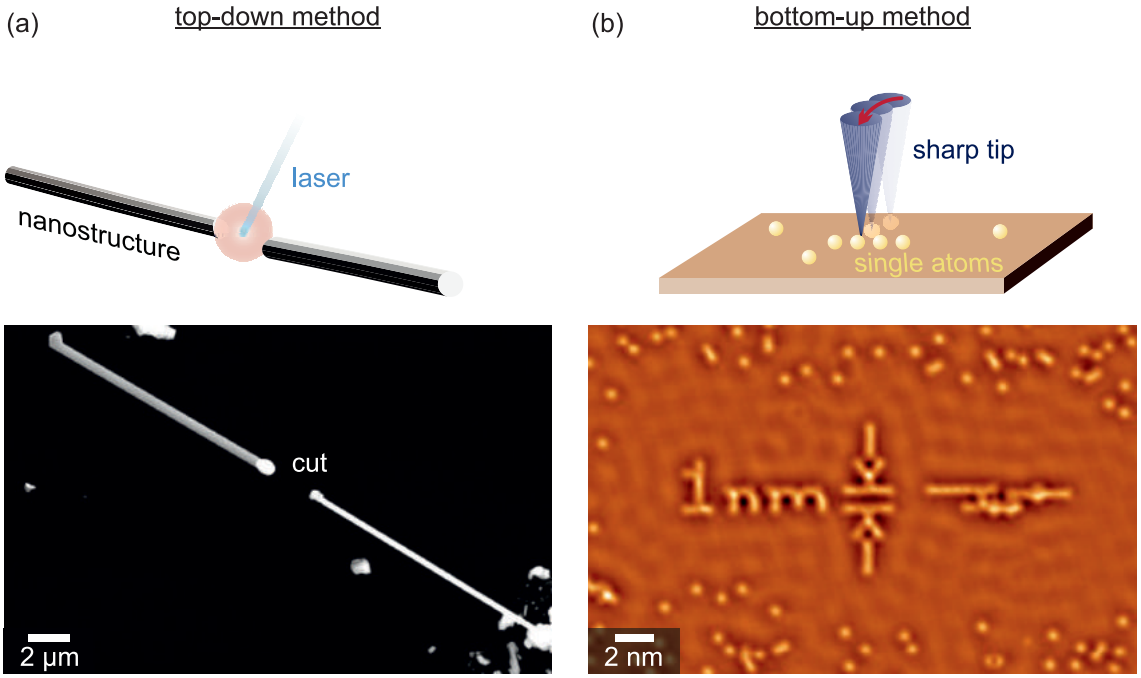

Fig. 2.2.2: Two approaches for nanomanufacturing. (a) Top-down method: A laser is used to cut a Bi_2Se_3 nanowire in the center [67]. (b) Bottom-up method: An atomic tip can be used to fabricate arbitrary structures by arranging single atoms. Picture taken from Ref. [68].

croscopy writing by direct manipulation of atoms which can be used to create arbitrary structures in a very slow process, as shown in Fig. 2.2.2(b).

Gas-phase bottom-up methods are the core techniques employed in this thesis. An advantage is that they allow for *in-situ* control of the growth conditions so that heterostructures with atomically sharp interfaces can be grown. Most materials would not naturally grow into nanowires. This is not only a matter of tuning the experimental parameters but also of providing the right support for nanowires to grow. A catalyst-coated substrate can promote quasi 1D growth. This leads to two fundamental growth mechanisms: vapour-liquid-solid (VLS) and vapour-solid.

VLS growth is a well established growth mechanism demonstrated for the first time in 1964 in the Bell Labs [69] and it is still used for the catalysed growth of nanowires today [70]. It involves three steps as illustrated in Fig. 2.2.3. At high temperatures, precursor atoms or molecules form a vapour with a carrier gas. When brought into contact with the catalyst, they alloy with the catalyst particle forming liquid droplets.

The nucleation process is initiated at the liquid-solid interface when the liquid alloy saturates. Further condensation of vapour on the particle supports the axial growth at the liquid-solid interface. In tip-catalysed growth, the catalyst particles are lifted up by the growing nanowire, as shown in Fig. 2.2.3. In root-catalysed growth they are found at the bottom of the nanowire. In vapour-solid growth the vapour resublimates without forming an intermediate liquid phase with a catalyst [71]. Both mechanisms were reported for nanowire growth of the material class studied in this thesis [72, 73].

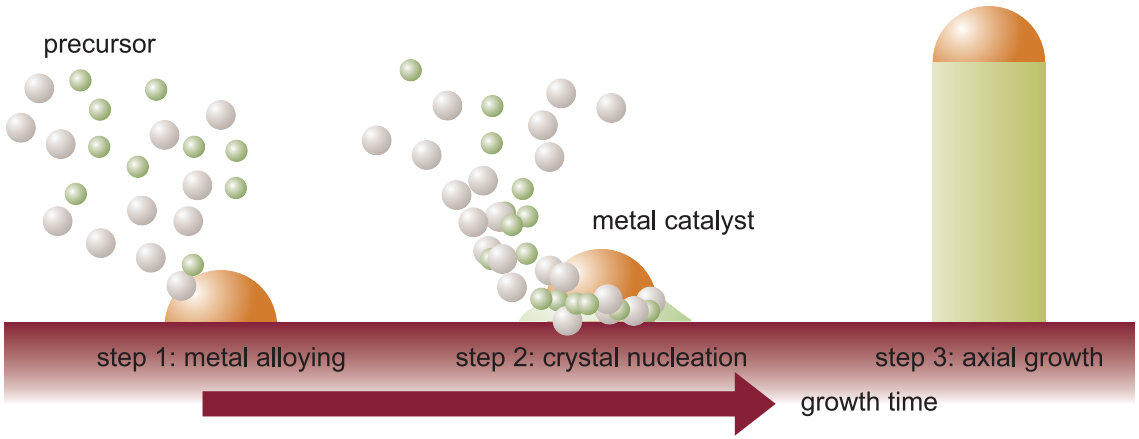

Fig. 2.2.3: The three steps of the vapour-liquid-solid growth mechanism. First, the precursor is interacting with the metal catalyst and forms an alloy. Upon saturation of the alloy, crystal nucleation starts. The catalyst particle is pushed upwards by the growing nanowire. This growth mode is called axial growth.

2.2.2 Role of the catalyst

It is important to analyse the role of the catalyst during growth, as the dimension and distribution of the nanowires on the substrate are closely related to the preparation and choice of the catalyst. There are reports about growth from various metal catalysts [74, 75]. Typically, nanowires are grown from Au nanoparticles between 5 nm and 30 nm in diameter, or Au films that split up into particles upon heating.

Au particle-assisted growth starts with depositing Au nanoparticles on a cleaned substrate. The nanoparticles are bound to the surface by coating the substrate with the

binding agent poly-L-lysine (PLL). PLL is an adhesive agent with a cationic end group originally employed for protein coating [76]. This process is called functionalisation of the substrate.

Once the surface is covered with the polymer film, a solution of Au nanoparticles is applied to the substrate. The diameter of the Au nanoparticles is 5 nm with a very narrow size distribution according to the vendor, *Nanocs*. More information on the size distribution will be presented in Chapter 4. The negatively charged Au nanoparticles adhere to the positively charged film and are homogenously distributed over the surface [77]. Since Au nanoparticles tend to form clusters, they are protected by a protecting agent polymer shell. During the growth, the shell burns away, and larger Au particles are formed by absorbing surrounding smaller ones. This process is known as Ostwald ripening and leads to an increase of the mean particle size [78]. Carbon residue from the polymer shell can be found on the substrate.

The advantages of Au are its capability to form low-temperature liquid alloys with inorganic precursor materials, chemical inertness, and thermal stability [74]. However, there are great disadvantages in the use of Au from the perspective of application of VLS grown nanowires for electrical devices. Depending on the solubility limit of the catalyst in the material, a small amount of the catalyst diffuses into the crystalline matrix of the nanowire. In case of Au this unintentional doping is particularly undesirable for electronic applications as it provides carrier recombination sites [79–81]. It was also found that Au migrates over the surface of nanowires contaminating the sidewalls [82,83]. Removal of these unwanted particles after the growth requires post-processing such as etching which in turn degrades the quality of the nanowires.

Research on alternative metal catalysts is driven by the prospect of electronic applications of nanowires, of which Si nanowires are by far the most well studied system [78]. Extensive comparative studies on various catalysts show that some metal catalysts such as Fe or Ni can achieve a similar yield and quality as Au-catalysed nano-

wires [84, 85]. Metal-oxide catalysts have not been reported at present. Therefore alternative catalysts like TiO_2 are investigated with the goal to improve electrical transport properties. TiO_2 nanoparticles with a diameter of 20 nm are the subject of intense research into their photocatalytic capabilities [86]. Depending on the arrangement of the four O atoms around a central Ti atom, one distinguishes three crystalline modifications: rutile, anatase, and brookite [87].

2.3 Small is good for quantum materials

The conducting surface states of TIs are usually masked by conduction through the bulk states caused by defects [88]. In order to study the TI surface states in an electrical transport measurement it is essential to suppress the bulk carrier density. TI nanomaterials fulfil precisely this prerequisite: Nanomaterials have a large surface-to-volume ratio, such that conducting surface states are dominant compared to the bulk states in electronic transport measurements. Electrical characterisation of nanowires and nanoribbons of the TI Bi_2Se_3 has shown evidence of enhanced surface conduction [72]. From an engineering point of view, nanowires are ideal building blocks in future spintronic and quantum devices [67].

There are four essential elements to spintronics: generation, preservation, manipulation, and detection of spin-polarised electrons. TIs are the obvious choice for spin preservation, taking advantage of spin-polarized edge channels that conduct carriers with low resistance [89]. However, decreased resistance is not only an advantage in terms of effective current transport, but likewise solves the problem of overheating in interconnects in ever smaller devices [90].

The materials studied in this thesis display the characteristics of an ideal thermoelectric material. Such materials exhibit a large temperature difference under an applied electric potential difference. This effect is enhanced by good electrical conductivity

(like a metal), high thermovoltage (like a semiconductor), and thermal insulation (like an insulator) [91]. This set of seemingly contradictory characteristics is found in TIs. They are semiconductors that are insulating in their bulk but host a conducting surface state. The thermoelectric properties of nanowires benefit from their high aspect ratio as electronic carrier transport has to go through the surface, while heat transport through the bulk is decreased as a function of nanowire diameter. Further, phonon transport is strongly reduced due to size effects. Recent studies aim to improve thermoelectric power and integration in thermoelectric cooling devices [92].

In general, applications that rely on surface reactions (such as catalysis, batteries, and sensors) benefit from the high surface area of nanowires. From a material growth perspective nanowires are interesting objects to study because they grow as nearly perfect single crystals. Defects like stacking faults as well as lattice strain, are dramatically reduced compared to bulk materials whereas mechanical properties such as elasticity are enhanced [93].

For integration in future devices it is essential to provide growth recipes for a clean and pure synthesis of single crystalline nanowires.

3 Experimental methods

Introduction

Crystal growth is a field that can be intuitively understood by thinking of examples such as stalactites that are formed by droplets dripping from a cave ceiling. VLS growth, however, requires more than mineral water. The topic of the first part of this chapter will be vapour deposition techniques which provide much faster growth rates, *in-situ* control of the precursor material, and highly pure crystals. The second part will focus on the analysis techniques of crystal properties such as shape and lattice geometry and touch upon selected analysis techniques for electronic properties.

3.1 Vapour deposition

Vapour deposition techniques now used for nanowire growth were originally developed for thin film growth. They have achieved a great level of maturity in the semiconductor industry and can be divided into two classes [94]. One is physical vapour deposition which is characterised by the use of a solid source to generate the precursor. It comprises techniques such as molecular beam epitaxy (MBE) and sputtering. The other class is chemical vapour deposition (CVD) which is characterised by gas phase reactions or gaseous decomposition to generate the precursor. The two physical vapour deposition techniques vapour transport and MBE are described in more detail below. CVD is more flexible than vapour transport in terms of control over the growth parameters but it was not used in this thesis because it requires expensive gaseous precursors and cannot compete with the cleanliness of an MBE. The substrate should satisfy certain requirements that will be discussed at the end of the section.

3.1.1 Vapour transport

The most simple form of vapour deposition is direct evaporation. A prominent example is tungsten evaporating from the wire in a light bulb to deposit a thin film of tungsten on the inner walls of the bulb. However, this process is extremely slow and the source will mostly be heated beyond its melting temperature to achieve a sensible deposition rate. A typical vapour pressure is above 10^{-3} mbar. Materials either evaporate as atoms, clusters of atoms, or molecules. Binary compounds such as Bi_2Se_3 dissociate so that the deposited material can have a different composition than the source. Selenium, in particular, has a much higher vapour pressure than Bi and this will lead to a stronger decrease of Se content relatively to Bi in the source material. In simple evaporation the flow of atoms is purely a function of temperature and amount of precursor material.

In vapour transport growth a constant gas flow of N_2 can be applied in the direction from the source material to the substrate in order to better control the precursor flow. The precursor material then forms a vapour with the carrier gas and the flow of precursor material provided at the substrate location becomes a function of the gas flow.

A horizontal, 60 cm long tube furnace (Nabertherm B180) equipped with a quartz tube of 22 mm inner diameter is used for vapour transport growth (Fig. 3.1.1). Substrates and precursor material are placed in quartz boats inside the tube. The precursor is prepared by grinding single crystals with a suitable stoichiometry into a powder. A few grams are placed on a quartz boat in the furnace centre, which is the point of highest temperature. The system is pumped to low vacuum using a membrane pump before loading the substrates in order to create a dry N_2 atmosphere in the tube. Substrates are loaded under maximum N_2 flow and placed at the cold end of the furnace. The substrate temperature is a function of furnace temperature and location of the substrate in the furnace, however, the vapour composition is also a function of location in the furnace since some elements have a lower vapour pressure than others.

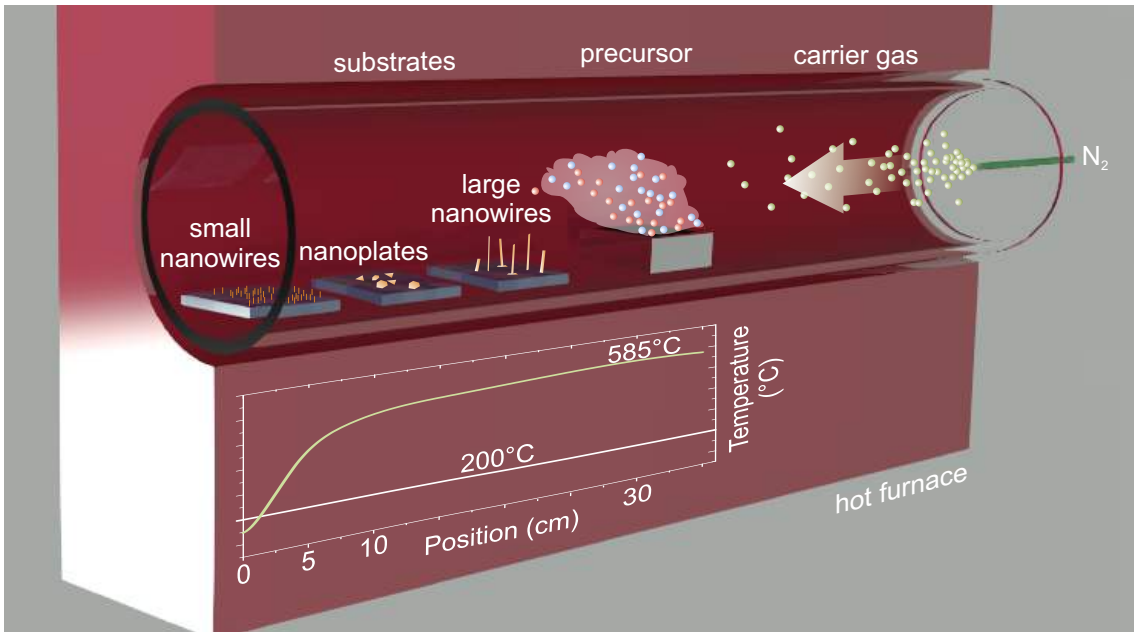

Fig. 3.1.1: Vapour transport growth setup. Nitrogen gas flows through a quartz tube that is placed inside a hot furnace (temperature profile for furnace temperature of 585°C). In the centre of the furnace the gas forms a vapour with the precursor material. Substrates are placed further downstream in a colder section of the furnace to allow for substrate temperature dependent nanowire growth.

3.1.2 Molecular beam epitaxy

MBE is the most precise and versatile technique for crystal growth available to semiconductor research. Its revolutionary ability to grow atomically sharp interfaces was, e.g., used to grow the first device that enabled blue laser emission from GaN (Nobel Prize in Physics 2014) [95].

The materials are evaporated into ultra-high vacuum (10^{-10} mbar background pressure) from 'small furnaces', as shown in Fig. 3.1.2, which allows to grow from multiple precursors simultaneously. These so-called Knudsen effusion cells are bottle-shaped ceramic crucibles that constantly evaporate material when heated. They are cut off from exposure of the substrate by shutters that can be opened instantaneously.

The atomic or molecular beams coming out of an effusion cell are quantified by a beam equivalent pressure called flux. The flux is a function of cell temperature and can be measured by unit of pressure *in-situ* using an ionisation-gauge that is placed

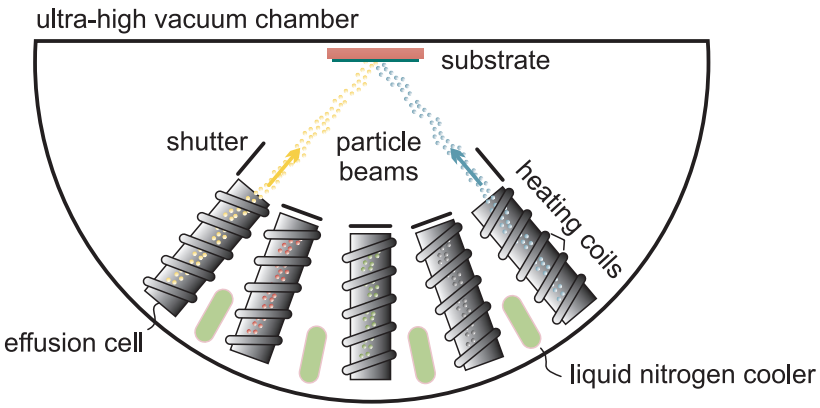

Fig. 3.1.2: Experimental setup for molecular beam epitaxy growth. Precursor elements are heated in effusion cells by heating coils until they evaporate. A shutter controls the particle beams toward the substrate. Liquid N_2 is used to cool the machine since the temperatures involved are very high and to increase the vacuum level by pumping water molecules. Picture re-drawn after Ref. [94].

at the substrate position. Typical values are 10^{-9} mbar (doping) to 10^{-6} mbar (very high pressure, e.g., used for Bi_2Se_3).

MBE offers full control over substrate temperature, source temperature, and vapour composition independently, whereas vapour transport growth is a rather 'empirical method guided by thermodynamics' [94], since each of these parameters depends on the others.

3.1.3 Substrates suitable for nanowire growth

A key factor for the choice of substrate is its reactivity with the deposited materials. In Fig. 3.1.3 three commonly used substrates are compared with respect to the growth of Bi_2Te_3 nanostructures. Ge and GaAs both react with either Te or Bi so that the nanostructures are not necessarily of the intended composition. Si, however, is not incorporated in the nanostructures because its melting point is much higher than Ge and, unlike GaAs, it does not decompose at the growth temperature. A thin oxidation layer is formed on its surface when exposed to air which further prevents any reaction. This layer is essentially an amorphous surface that also hinders epitaxial growth. Si is employed for most experiments in this thesis as a platform to grow nanowires on. An

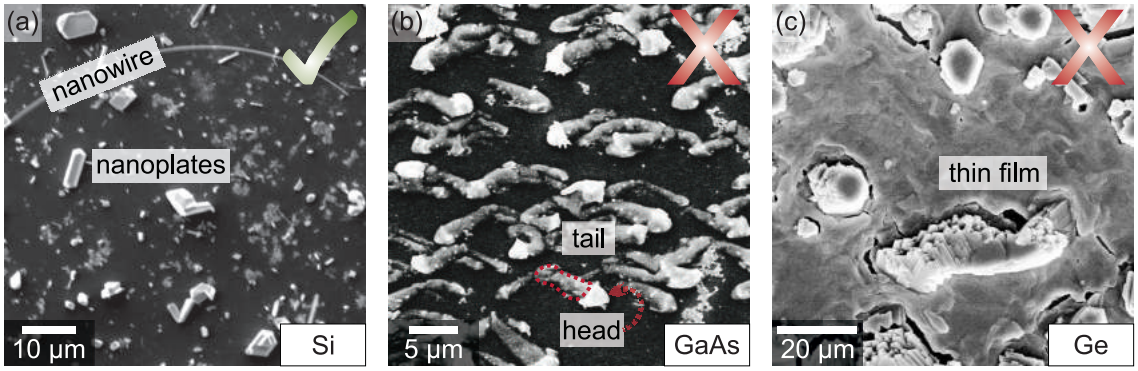

Fig. 3.1.3: Bi_2Te_3 nanostructures grown on three different substrates. (a) On Si randomly oriented clusters, plates, and nanowires are grown. Acceleration voltage: 20 kV. (b) On GaAs the precursors react with the substrate forming clusters (heads) that apparently 'creep' over the surface leaving traces (tail) during the growth. Acceleration voltage: 20 kV. (c) On Ge a thin film of Bi, Te, and Ge is grown. Acceleration voltage: 30 kV. Instrument: Jeol JSM-6610LV.

advantage is that Si is widely used in the semiconductor industry and as-grown samples could be used for backgating if necessary.

Substrates are prepared before the growth using a standard cleaning procedure and catalyst coating if applicable [96]:

1. boil in trichlorethylene (3 min);
2. cold dip in isopropanol;
3. boil in isopropanol (3 min);
4. cold dip in methanol;
5. boil in methanol (3 min);
6. rinse methanol with water;
7. blow drying using nitrogen;
8. apply diluted PLL solution with ratio 1:10 (3 min);
9. rinse PLL with water;
10. apply catalyst solution with ratio 1:10 (3 min);
11. rinse catalyst with water;
12. blow drying using nitrogen.

3.2 Characterisation techniques

When a sample is removed from the furnace it is initially inspected by eye. The polished Si substrate reflects most light. The catalyst coating is either invisible (Au nanoparticles) or appears as white spots (TiO_2) in case there are clusters. Experience is able to tell the size and shape of the structures that have formed on the surface during growth, e.g., $(Bi,Sb)_2(Se,Te)_3$ nanoclusters and sparsely distributed nanowires appear as a grey coating that is getting darker if the density is high. The most extreme example of this is Cd_3As_2 which shows black spots because the nanowire density is very high. Microplatelets, ribbons, and sub-micron belts cause additional reflections leading to a glittering sample.

More advanced tools to characterise nanowire samples are described below.

3.2.1 Crystal properties

Atomic force microscopy

Atomic force microscopy (AFM) is useful to obtain a height profile of the sample and is even able to resolve atomic steps. In order to scan the sample surface the movement of a cantilever with a sharp tip at its end is traced by the reflection of a laser from the back of the cantilever onto a four-quadrant photodiode. The sample is mounted on a piezo stage to allow for precise control in all direction. In tapping mode the cantilever is excited to oscillate near its resonance frequency. When it approaches the surface, a distance-dependent interaction between the tip and the surface causes the resonance frequency to change. The surface topography is examined in linescans of the tip over the surface by adapting the excitation frequency with the aim to keep the oscillation amplitude constant. Shortcomings of an AFM inlude its slow scan rate and tip-sample convolution leading to inaccurate slopes at step edges.

Raman spectroscopy

Molecular vibrations and rotations can be excited and absorbed by light. This phenomenon is called Raman effect and was discovered almost a century ago. If the frequency of the incident light is ν_0, the elastically scattered so-called Rayleigh light is emitted at ν_0. This is a result of a dipole moment induced by the electric field into the static molecule by the incident wave. Vibrations change the polarizability of the molecule. This gives rise to a second component of inelastically scattered light which can be detected at $\nu_0 \pm \nu_{\text{vib}}$, the so-called Stokes (−) and anti-Stokes (+) line. The Stokes line represents an excitation of a vibration, whereas the anti-Stokes line represents the absorption of a vibration. The vibrational frequency ν_{vib} can be regarded as a fingerprint of the molecule since it depends on bonding length, moment of inertia, and mass of the molecule. This makes Raman spectroscopy a versatile tool in security application for the non-destructive identification of drugs, explosives, and toxics.

In solids, the degradation (increase) of the frequency of the incoming light is caused by the creation (annihilation) of transverse optical or longitudinal optical phonons via a three-step process: (i) An electron-hole pair is created by an incoming photon. (ii) The electron-hole pair interacts with the lattice and creates or absorbs a phonon. (iii) A photon is emitted through recombination of the electron-hole pair. Intensity and frequency of the emitted light provide a wealth of information about the physical properties of the crystal such as elemental composition, electron-phonon interaction, or surface plasmons.

An experimental setup requires three components: light source, monochromator, and detector. A laser is used as a light source to maximise intensity. The monochromator filters out the strong Rayleigh light since it surpasses the Stokes light by several orders of magnitude and since $\nu_0 \gg \nu_{\text{vib}}$, i.e., the two lines are close together. A band pass filter can be used if the laser wavelength is fixed.

Individual nanowires can be studied if the laser spot is sufficiently small (500 nm), the nanowire is deposited on a suitable substrate with a low background (e.g. CaF), and optimum focus on the nanowire is achieved. This requires a micro-Raman experiment in which the laser is guided through a microscope objective onto the sample which was achieved using the following two instruments:

- Renishaw inVia confocal Raman microscope (RCaH, Didcot, UK) equipped with a Ti:sapphire laser (λ = 830 nm)

- Horiba T64000 Raman spectrometer system (Freie Universität Berlin, Germany) in combination with a He-Ne (λ = 633 nm) or a tunable titanium-sapphire laser (λ = 800 nm) and a triple grating spectrometer with a spectral resolution of 1 cm^{-1}. The spectrometer was calibrated using a Ne standard.

The polarisation of the laser light was parallel to the nanowire axis to maximise the intensity. All measurements were carried out at room temperature. The data is typically presented as intensity over frequency shift with respect to the Rayleigh light in units of wavenumbers, as shown in Fig. 3.2.1.

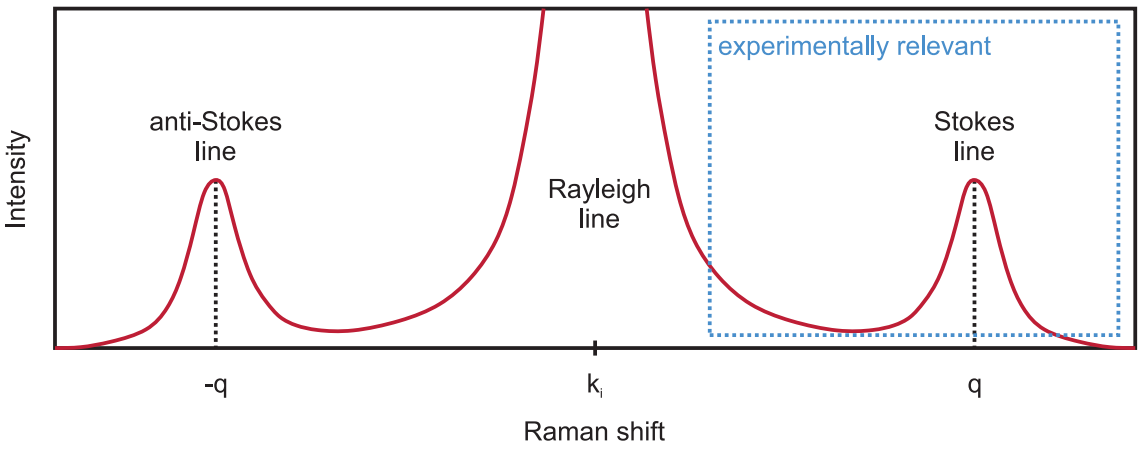

Fig. 3.2.1: A Raman spectrum consists of the Rayleigh line of elastically scattered light and two lines of inelastically scattered light symmetrically arranged at lower and higher wavenumbers. The wavenumber q is related to the energy of a lattice vibration. The anti-Stokes line is typically weaker than the Stokes line so that it is sufficient to present the part highlighted by a blue rectangle in the experimental analysis.

Electron microscopy

The resolution of optical microscopy is limited to structures on the scale of hundreds of nanometres by the wavelength of light. A smaller probe wavelength is required in order to study catalytic tips, atomic steps, or the crystal structure of nanowire samples. Electron microscopy utilises electrons for sample imaging which have a wavelength of 9 pm at 20 keV so that nanostructures can be resolved. A scanning electron microscope (SEM) covers a magnification range from ×20 to ×100,000 and is suitable for the study of as-grown samples. A transmission electron microscope (TEM) covers a magnification range from ×100,000 to ×25,000,000 and requires specific sample preparation. Both instruments can also be equipped with the capability to determine the elemental composition of samples by energy-dispersive x-ray spectroscopy (EDS).

SEM utilises secondary electrons to image the sample surface [97]. Electrons are extracted from a source (tungsten filament or lanthanum hexaboride crystal) with an accelerating voltage of up to 30 kV. Electromagnetic lenses focus the beam and images are recorded by scanning the beam over the surface. For every point an electron detector measures the intensity of secondary electrons that are excited by the incoming beam. Secondary electrons stem from shallow near-surface regions with a depth depending on the energy of the incoming electrons. Steep features of the sample give rise to a higher amount of scattered electrons and appear brighter than flat areas. The final image represents a topography of the surface. The following microscopes were used:

- Jeol JSM-6610LV equipped with a tungsten hairpin filament (RCaH, Didcot, UK)
- FEI Quanta 600 FEG equipped with a lanthanum hexaboride cathode (Oxford, UK)
- FEI Magellan 400 XHR SEM (Stanford, US)

The working principle of a TEM is similar to an optical microscope, but instead of

light it employs electrons to image the sample [98]. Electrons are extracted from a filament, accelerated, and focused onto the specimen through electromagnetic lenses. A TEM is typically operated at ten times the electron energies of a SEM, since the electrons that are transmitted through the sample are used for imaging. In order to allow the beam to pass through the sample, the sample thickness must not exceed several hundreds of nanometres. The image can be displayed on a phosphorus screen. It is a static image of electron intensity variations. The intensity depends on the absorption of the material. A TEM can be modified to scan the beam over the specimen, a technique which is called scanning transmission electron microscopy (STEM). The two main advantages are elemental mapping and imaging of individual atomic columns with the contrast being related to the atomic number. Conventional TEM relies on the phase contrast between the transmitted and diffracted waves which is more challenging to interpret than STEM images.

Two sample preparation techniques are employed: One way is to break nanowires from the substrate and deposit them onto carbon-coated copper grids. To transfer the nanowires onto the grid, a drop of water is placed on the as-grown substrate. The drop is frozen using liquid N_2 and transferred onto the grid. Upon evaporation of the water nanowires that were broken from the substrate and fixed in the ice are found on the grid. Using this preparation technique a large number of nanowires can be studied at once and imaged from the tip to the base.

Another way is to deposit a single nanowire flat on a Si substrate, cut a thin slice from the center, and image the cross-section. The nanowire can either be transferred from the as-grown substrate via the freezing method or using a micro-chisel if it is large enough. The droplet method has the advantage that nanowires are deposited flat on the substrate when the water evaporates but they might not be located in the center. With the chisel method a nanowire can be precisely deposited, but it might form kinks that prevent it from resting fully on the substrate. A slice is cut using focused ion beam

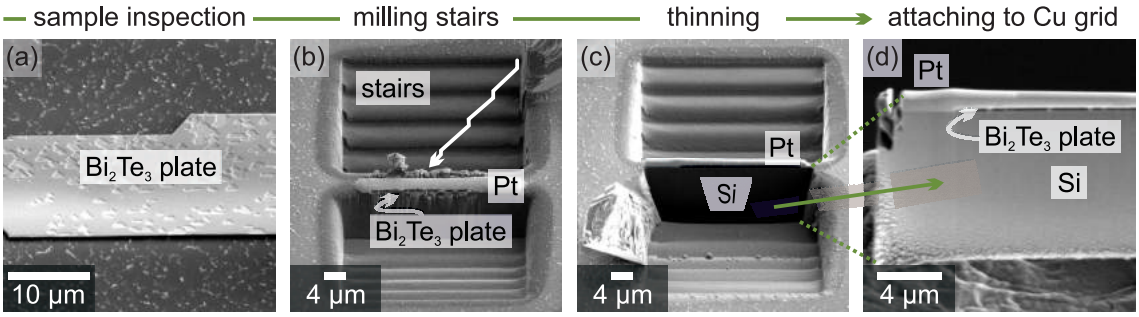

Fig. 3.2.2: Sample preparation using FIB. (a) The sample is a broad Bi_2Te_3 plate on the as-grown substrate (Si). (b) Steps are carved out after the plate has been covered by a Pt layer. (c) The slice is cleaned and thinned. (d) The slice is attached to a copper holder. The sample is sandwiched between the Pt layer and the Si substrate. Instrument: FEI DualBeam FIB-SEM systems; acceleration voltage: 5 keV.

(FIB), as shown in Fig. 3.2.2(a-d) for the example of a plate. The sample is covered by a Pt layer to protect the surface and dissipate heat during the Ga ion beam etching. Steps are carved out into the substrate to create the slice. The region containing the sample cross-section is further thinned to several tens of nanometres. Finally, the slice is attached to a copper holder that can be mounted in the microscope. Cross-sectional TEM gives a more precise image of the outline of the sample than AFM or SEM could do. It is particularly suited to study heterostructures and nanostructures that would be too thick for imaging on copper grids.

The following two instruments were used at an acceleration voltage of 200 keV:

- Jeol 2100 (TEM, RCaH, Didcot, UK)
- Jeol ARM200F (STEM) equipped with a high-angle annular dark field detector (StEM, Stuttgart, Germany)

Electrons of the incoming electron beam in an SEM or TEM excite inner shell electrons. The recombination proceeds through the emission of x-ray photons. The resulting emission spectrum is characteristic for each element and can be used to identify the composition of the sample material using EDS. Both the SEM and TEM are equipped with an X-MAX Silicon Drift Detector from Oxford Instruments for EDS measurements. TEM-EDS measurements of nanowires are a valuable tool for the

analysis of the stoichiometry with high lateral resolution. Since measurements of the x-ray photons are a statistical process, the accuracy depends on the counting time.

X-ray diffraction

Radiation with a wavelength similar to the interatomic distances is required for structural studies on crystals. This makes x-rays an essential tool in crystallography since their wavelength is approximately between 0.01 Å and 100 Å [99]. Scattering of x-rays with a wavelength λ from crystal lattice planes with a spacing d leads to constructive interference at certain angles θ that can be calculated using the Bragg equation

$$n\lambda = 2d\sin\theta \tag{3.2.1}$$

with the diffraction order $n = 1,2,3\ldots$. We are interested in the position of the intensity maxima at an angle 2θ with respect to the incident beam. For a single crystal the diffraction pattern consists of discrete spots that reflect the periodicity of the reciprocal lattice and real lattice. If a powder with random crystal orientations is used instead, the diffraction spots become concentric rings that are located at a certain distance from the main spot that corresponds to 2θ. An analysis of the integrated diffraction pattern can be used to identify the crystal structure and to determine the lattice parameters of the sample. It provides comprehensive structural information including atomic occupancies and atomic positions.

The following two experimental setups were used for x-ray diffraction:

- Beamline I15 at Diamond Light Source using an incident monochromatic wavelength of 0.33459 Å that was collimated with a 30 µm pinhole. The sample material was removed from the growth substrate using a micro-chisel and placed into a diamond anvil cell. Powder diffraction patterns are recorded using a MAR345 image plate or a Perkin Elmer detector and integrated using the software Fit2D

[100]. The integrated data was analysed using the software Topas [101].

- Agilent Supernova using copper or molybdenum x-ray sources. The sample material is mounted in a drop of oil on a microloop. Powder diffraction patterns are recorded using an Atlas CCD detector and integrated using CrysAlisPro [102].

3.2.2 Electronic properties

Angle-resolved photoemission spectroscopy

Metal plates become positively charged when light (short-wavelength visible or ultraviolet) is shone upon them. The underlying photoelectric effect and its discovery was such a significant milestone in quantum physics that it was awarded a Nobel Prize in 1921 [103]. There are three steps to the photoemission process [104]:

1. A photoelectron is excited inside the bulk by an incoming photon.
2. The photoelectron travels to the surface.
3. The electron is emitted into the vacuum.

The photoelectric effect can be used to probe the electronic binding energy E_B if the workfunction Φ and the photon energy hν are known and the kinetic energy E_K of the photoelectron is measured experimentally.

$$E_B = h\nu - E_K - \Phi \tag{3.2.2}$$

One can go further by dissecting the length of the photoelectron's wave vector $k = \sqrt{2mE_K}/\hbar$ into its components parallel and perpendicular to the surface of the sample. The perpendicular component changes during the emission process due to electric fields on the surface but the parallel component is conserved:

$$k_{\parallel,\text{bulk}} = k_{\parallel,\text{vacuum}}. \tag{3.2.3}$$

The x and y component of $k_{\parallel\text{bulk}}$ can be extracted by measuring the polar angle θ and the azimuthal angle ϕ, as shown in Fig. 3.2.3(a):

$$k_{\parallel,\text{bulk},x} = \frac{\sqrt{2mE_K}}{\hbar} \cdot \sin\theta\cos\phi \tag{3.2.4}$$

$$k_{\parallel,\mathrm{bulk},y} = \frac{\sqrt{2mE_K}}{\hbar} \cdot \sin\theta \sin\phi. \tag{3.2.5}$$

This simplicity makes angle-resolved photoemission spectroscopy (ARPES) the most direct tool to probe the bandstructure of solids. The experimental setup requires ultra-high vacuum, a light source, e.g., a He lamp or synchrotron light, and a detector. A famous example for this is the measurement of a Dirac cone, the signature of a TI as shown in Fig. 3.2.3(b).

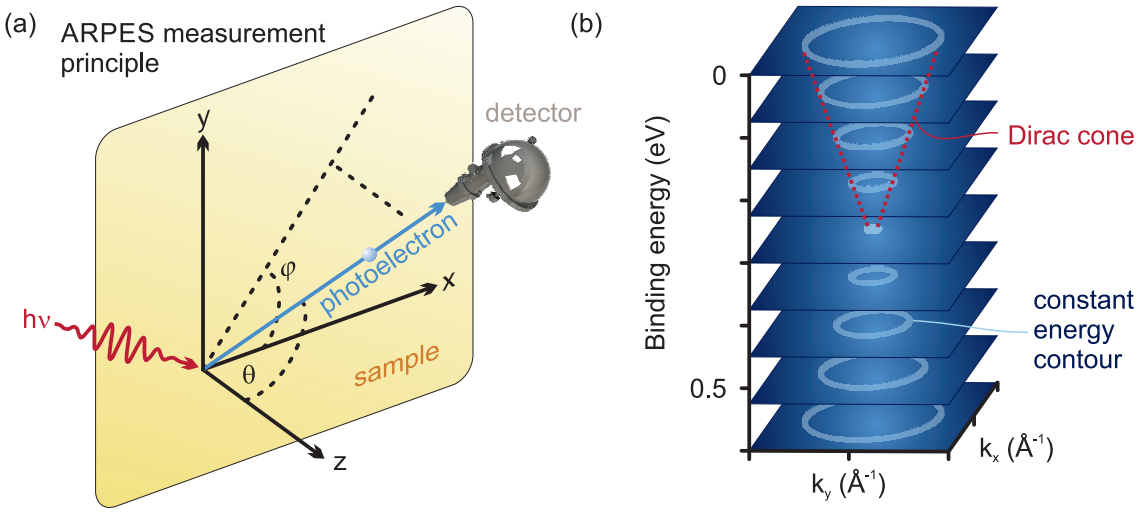

Fig. 3.2.3: (a) The most essential parameters in an ARPES experiment are the angles ϕ and θ that describe the detector position with respect to the sample and the energy $h\nu$ of the photoexcitation light. (b) Mapping the electronic binding energy of the surface electrons of a TI over k_x and k_y shows a cone-like energy dispersion. Picture re-drawn after Ref. [105]. The image of the detector is at the courtesy of Cheng Chen (University of Oxford).

ARPES has been the main driving force behind the discovery of new topological *quantum materials* during the last couple of years [105]. Nano-ARPES and spin-resolved ARPES are recent advances in the field that will contribute to the significance of ARPES in next decade [106].

Electronic transport measurements

Electronic transport measurements were carried out on individual sub-micron belts by Dr Danny Kojda at the Humboldt-Universität zu Berlin. The belts were transferred from the as-grown sample onto a clean Si wafer covered with a 300 nm oxide layer.

Each belt was picked up individually using a piezo controlled micro-needle under a microscope [107]. Electrical contacting follows a standard procedure including spin-coating of photoresist (using AZ3007 photoresist), laser photolithography, and 50 nm Au deposition. Au contact pads are connected to a chip carrier by Al wires.

The chip carrier is loaded into a flow cryostat to measure temperature-dependent resistance curves by current-voltage sweeps in four-point configuration (using a Keithley 6221 current source and Keithley 2182A nanovoltmeter). Four-point contacts ensure that the contact resistance can be excluded from the measurement by using the two outer contacts to inject a current and the two inner contacts to measure the voltage over the belt.

Subsequently to the transport measurements, cross-sections were obtained using a Nova 600 NanoLab (FEI). First, the belt is covered with a platinum layer deposited at an electron voltage of 5 kV and a beam current of 0.4 nA. The platinum layer serves as protection layer and as thermal bridge to sink the heat during the focused ion beam etching. A gallium ion current of 50 pA is used at a voltage of 10 kV for etching.

Synchrotron sources

Synchrotrons provide focused light with high intensity, brilliance, and variable wavelength. Electrons are accelerated in a linear accelerator and booster ring before they are injected into the storage ring. At a velocity close to the speed of light the particles are forced onto a circular trajectory by a series of bending magnets. Through the interaction with the magnetic field the particles emit x-rays with low angular divergence in the forward direction. On beamlines that are attached tangentially to the storage ring this radiation is employed for diffraction experiments, among others. The entire synchrotron system is kept under ultra-high vacuum. Synchrotron light was used for ARPES experiments and powder XRD.

Terahertz spectroscopy

Optical pump-THz probe spectroscopy is used to extract mobility and lifetime of electronic carriers through the determination of the photoconductivity of a nanowire [108]. The sample is photoexcited by 35 fs pulses of a 800 nm laser with a fluence between 1 and 805 µJ·cm^{-2}. This generates short-lived electron-hole pairs that change the photoinduced conductivity σ of the sample. The change $\Delta\sigma$ can be probed by a THz pulse by comparing the transmission of the pulse in the ground state E with the change ΔE that is induced by the photoexcitation via [109]

$$\Delta\sigma = \epsilon_0 \left(\frac{1}{\frac{1}{f_w}\frac{\Delta E}{E} + 1} - 1 \right) \left[\frac{2c}{d} - i\omega(1+\epsilon_w) \right], \tag{3.2.6}$$

where d is the diameter of the nanowires, f_w the effective areal fill factor of the nanowires on quartz, ϵ_0 the permittivity of free space, ϵ_w the permittivity of the sample, c the speed of light in vacuum, and ω the THz frequency.

4 Nanostructure growth mechanisms

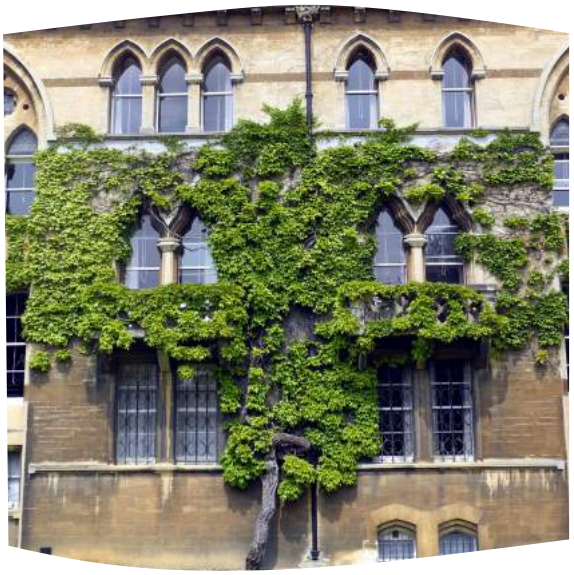

Introduction

In the following four chapters, I present the results and discussion from experimental work on *quantum materials* nanostructures. Chapter 5 to Chapter 7 focus on specific materials each including a showcase of their electrical properties. This chapter gives an overview over the growth mechanisms of selected nanowire systems. Some of them cannot be explained within the VLS model as introduced in Chapter 2. The first part will analyse the role of the catalyst, from Au catalysed growth over TiO_2-catalysed growth, to catalyst-free growth in Bi-based materials. The second part discusses the growth mechanism of three non-layered systems. I start with a review of the use of Au in the growth of TI nanowires.

4.1 Au-catalysed growth

Au nanoparticles have been used in the vapour transport growth of TI nanowires very early on [49, 88, 110]. The VLS growth mechanism requires the formation of a catalyst-precursor alloy and the subsequent crystallisation out of the supersaturated solution [71]. Hamdou *et al.* mapped the pre-growth location of Au-catalyst particles and compared them to the position of the grown nanoribbons [111]. Typically, the metal alloy particle is either found at the tip or the root of the nanowire [112, 113]. So far, the Au-assisted growth of chalcogenide nanowires is mainly explained with reference to tip-catalysed VLS growth [45, 46, 73, 111, 114]. Specifically, tip-catalysed VLS growth was observed for Bi_2Se_3 nanowires by Kong *et al.* using 20-nm-diameter Au particles [72]. Alegria *et al.* conversely reported root-based growth of Bi_2Se_3 nanostructures from an annealed, 5-nm-thick Au layer using metal-organic CVD [73]. The differing growth mechanisms were explained by the use of a metal-organic gas source instead of a solid precursor.

4.1.1 Role of catalyst size

In this section it will become clear that it is not the growth technique that determines the type of VLS growth mechanism but rather the size of the catalytic particle. A sample was removed at an early stage of the growth process to gain an insight into the early working of the catalyst particle . The parameters are shown in Table 4.1.1.

Table 4.1.1: Experimental parameters for the growth of mounds around catalyst particles.

Parameter		**Value**
growth method		vapour transport
substrate	type	Si(100)
	preparation	standard cleaning
	functionalisation	PLL solution
	catalyst coating	Au
precursor		Bi_2Te_2Se
N_2 flow rate		150 sccm
growth temperature		585 °C
growth time		5 min
substrate temperature		545 °C

AFM scans reveal rounded mounds with an indentation in their centre as shown in Fig. 4.1.1(a). The width of the structure in the centre of the indentation is 5 nm – the same as the diameter of the Au catalyst particles, as shown in Fig. 4.1.1(b). The

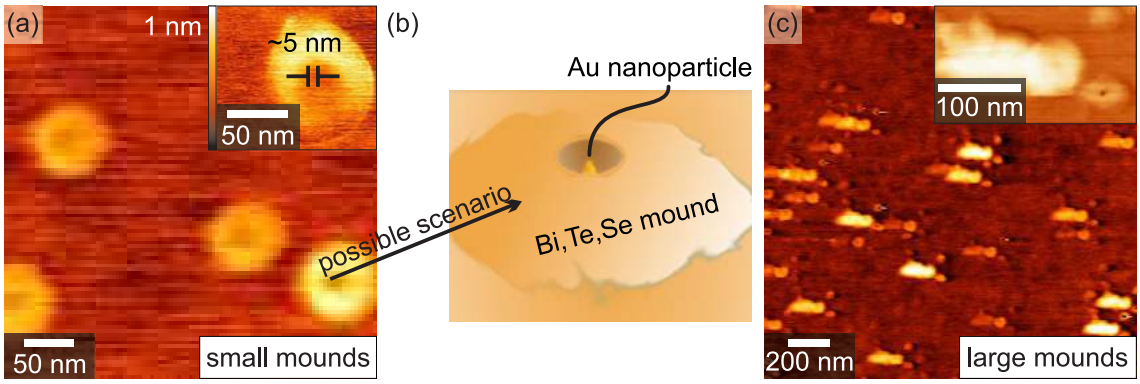

Fig. 4.1.1: AFM images of the Au catalyst and the deposited Bi_2Te_2Se precursor material at an early stage of the VLS growth process. (a) Precursor mounds with a ditch in the center. Inset: The width of the ditch is on the scale of a 5 nm Au catalyst nanoparticle. (b) Sketch of an Au nanoparticle in the center of the ditch. (c) Some mounds accumulate more precursor than others.

hillocks have no apparent structure and do not show any symmetry or characteristic quintuple-layer-high steps, as shown in Fig. 4.1.1(c). Structures with a similar shape were reported to appear in studies of SiO_2 encapsulation of Au nanoparticles on Si substrates upon annealing in oxygen atmosphere [115]. The observed mounds are too small to identify their composition unambiguously using EDS. It is unlikely that they are SiO_2, since the experiments were carried out under N_2 atmosphere. If the unspecified material is the precursor, it gives evidence of an early stage of the alloy particle. Firstly, the Au particle does not facilitate a permanent metal-precursor formation. Secondly, Au particles merely provide nucleation centres that promote precursor deposition, but are subsequently buried. This also agrees with the possibility of catalyst-free synthesis of Bi_2Se_3 nanostructures [116].

This effect of a transition from root- to tip-catalysed growth can be explained by a catalyst-substrate interaction that depends on the size of the catalyst particle. If the Au catalyst alloys with the SiO_2/Si substrate, e.g., driven by size-dependent melting point reduction, it will not be lifted up by the growing wire but stay at the interface with the substrate. For larger catalyst particles, alloying is still expected at the boundary of the particle, but the overall anchoring to the substrate is too weak and the particle is lifted up as the wire grows. An example of the former situation is shown in Fig. 4.1.2. This AFM scan shows the example of a catalytic particle sticking to the root of the nanowire (white circle).

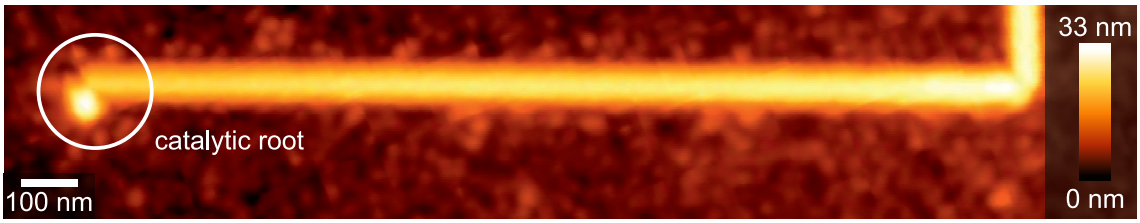

Fig. 4.1.2: AFM micrograph of a Bi_2Se_2Te nanowire on Si. The catalytic root is highlighted by a white circle. A second nanowire sticks to the tip of the wire.

4.1.2 Contamination by gold nanoparticles

Au is the first choice as a catalyst for nanowire growth due to the fact that it can alloy with most precursor materials [74, 117]. However, in recent years, it became clear that Au has several drawbacks such as a preference for certain facets, [81, 83] unintentional doping, [79, 80, 85, 118] and limitation of the growth through diffusion [82].

In the previous section, we have seen that Au can be used for chalcogenide nanowire growth too. The drawbacks, however, are that the Au catalyst is found to be spread along the nanowire axis, as can be seen on the example of a Bi_2Se_3 nanowire in Fig. 4.1.3.

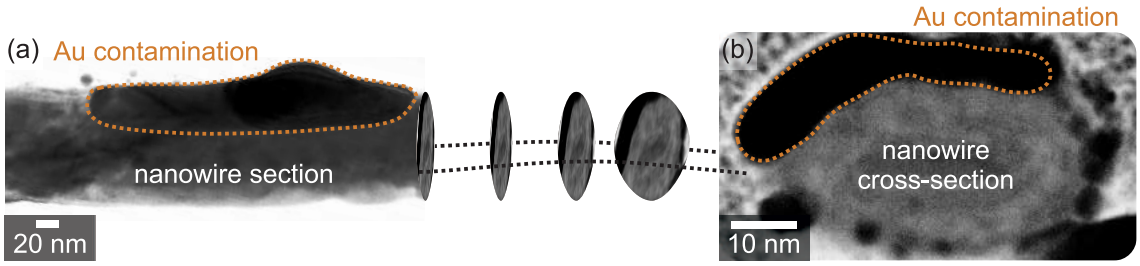

Fig. 4.1.3: (a) TEM micrograph of a Bi_2Se_3 nanowire on a Cu-grid grown at a substrate temperature of 450°C and a flow rate of 150 sccm. The sidewall is contaminated by the Au catalyst (orange dashed envelope). Instrument: Jeol 2100. (b) TEM micrograph of a Bi_2Se_3 nanowire cross-section prepared by FIB. The contamination (orange dashed envelope) covers part of the sidewall. There are several clusters of Au attached to the nanowire. Instrument: Jeol ARM200F.

Such a contamination strongly limits the potential of TI nanowires for applications in the semiconductor industry, but it provides an interesting insight into the Au-assisted growth mechanism: First, the catalyst-precursor alloy must be liquid during the growth. Otherwise, it would not be able to spread over the sidewalls [119]. Second, Au-rich particles are formed of an Au-Se alloy without Bi. This helps to explain the catalyst-precursor interaction in greater detail: Se is provided in excess due to its high vapour pressure. Since the growth temperature is below the eutectic point of an alloy consisting of Bi_2Se_3 and Au (635°C), no ternary alloy is formed [120]. The binary alloy Au-Se, however, is liquid at the growth temperature (bulk melting point: 425°C) [121]. Hence, Bi initiates the nucleation from the Au-Se alloy.

The role of Au in chalcogenide nanowire growth is rather ambivalent. On the one side, it has been successfully applied in several works that also included transport measurements [45, 46, 49, 73, 88, 111, 114]. We have shown that 5-nm-sized nanoparticles facilitate bottom-catalysed VLS growth and explained the interplay between Au and the precursor vapour. On the other side, it has severe drawbacks from the perspective of an application in device production due to the contamination issues. In the next section, I will present an alternative catalyst to remedy this problem.

4.2 TiO_2-catalysed growth

Research on alternative catalysts for nanowire growth is relatively rare because of the popularity of Au [74, 122]. Starting from TiO_2-supported Au nanoparticles we have carried out a study on the performance of TiO_2 nanoparticle based catalysts in comparison with Au for the growth of Sb-doped Bi_2Se_3 nanowires. The key finding is that a special mixture TiO_2 catalyst outperforms Au in terms of material and growth quality. In the second part of this section the TiO_2-catalysed growth of Bi_2Te_3 sub-micron belts is presented and a rigorous description of the growth mechanism is developed.

4.2.1 Bi_2Se_3

Nanowires were grown following the recipe given in Table 4.2.1 using conventional Au nanoparticles with a diameter of (7±1) nm as shown in Fig. 4.2.1(a) and the two polymorphs of TiO_2, rutile with a diameter of (375±165) nm as shown in Fig. 4.2.1(b) and anatase with a diameter of (30±7) nm as shown in Fig. 4.2.1(c). In order to investigate the dependence on TiO_2 catalyst size, we also studied the growth using high surface area (HSA) anatase nanoparticles with a diameter of (5±1) nm as shown in Fig. 4.2.1(d). It is known from photocatalytic experiments that mixed-phase catalysts outperform pure polymorphs [123]. P-25, shown in Fig. 4.2.1(e), is a commercial,

mixed-phase TiO_2 powder (Degussa) with a diameter of (20±6) nm, and well-known as a photocatalyst with very high activity [124]. It consists of the two TiO_2 phases anatase and rutile in a ratio of 3:1, with a small amount of the amorphous phase [125, 126]. Finally, a heterogeneous catalyst combining Au with a diameter of (3±1) nm and TiO_2 P-25 in a ratio of 1:20 as shown in Fig. 4.2.1(f) prepared using the sol-immobilization method by Dr Wilm Jones (UK Catalysis Hub) was investigated to explore a potential enhancement of the catalytic activity that is known from, e.g., carbon monoxide oxidation [127]. The two P-25 based catalysts (pure and P-25 supported Au) form smaller

Table 4.2.1: Growth parameters for a comparative study on Au and TiO_2-based catalysts.

Parameter		**Value**
growth method		vapour transport
substrate	type preparation functionalisation catalyst coating	Si(100) standard cleaning PLL solution Au, TiO_2 (P-25, anatase, rutile), Au/TiO_2
precursor		Sb-doped Bi_2Se_3
N_2 flow rate		150 sccm
growth temperature		585 °C
ramp time		1 h
growth time		1 h
substrate temperature		450 °C
analysis methods		SEM, EDS, TEM

clusters of particles, compared to anatase, rutile, and HSA. When growing without PLL we observed the formation of catalyst particle clusters for TiO_2 and a decrease in growth quality for both Au and TiO_2. This shows that the TiO_2 nanoparticles bind to PLL in a similar way as Au.

In the following, we describe the growth of Sb-doped Bi_2Se_3 nanowires for each of the six catalyst types. Length, diameter, and density are determined from SEM scans in top-view and summarised in Fig. 4.2.2. Figure 4.2.3(a) shows Au catalysed nanowires (inset), overall however, the growth is dominated equally by nanowires and nanoplates.

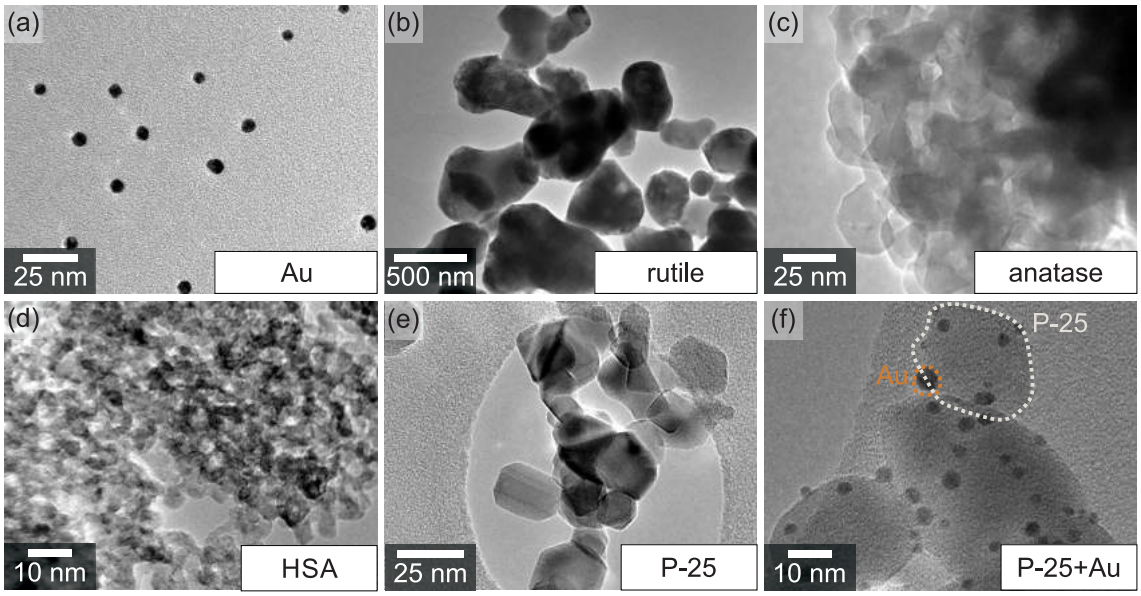

Fig. 4.2.1: TEM images of the catalyst particles. Mean particle sizes are: (a) Au (7±1) nm, (b) rutile (375±165) nm, (c) anatase (30±7) nm, (d) HSA (5±1) nm, (e) P-25 TiO_2 (anatase and rutile mixture) (20±6) nm, and (f) Au nanoparticles of size (3±1) nm on P-25 supports. Instrument: Jeol 2100.

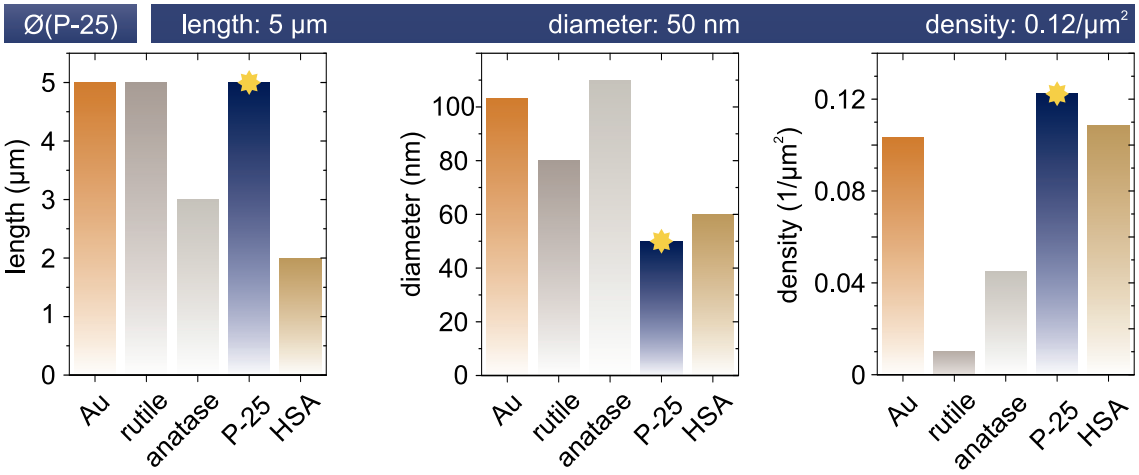

Fig. 4.2.2: Dimensions and density (number of nanowires per unit area) of Sb-doped Bi_2Se_3 nanowires grown using various catalysts as determined by top-view SEM imaging. P-25 performs well in all three categories: Nanowires grown using this catalyst are long, thin, and dense. The nanowire yield for P-25-Au is too low to gather sufficient statistics on the growth.

For rutile grown nanowires, as shown in Fig. 4.2.3(b), catalyst particles cover the surface homogeneously with clusters of approximately 0.5–3 µm in diameter forming a visible white layer already when the solution is washed from the substrate. The use of anatase, as shown in Fig. 4.2.3(c), results in nanowires, many compact clusters, and ribbons. Undesired growth products (clusters and nanosheets) are smaller, but more abundant than for rutile. The yield for anatase is higher compared to rutile. Most likely there is a lack of rutile particles with a sufficiently small diameter to grow nanowires due to clustering.

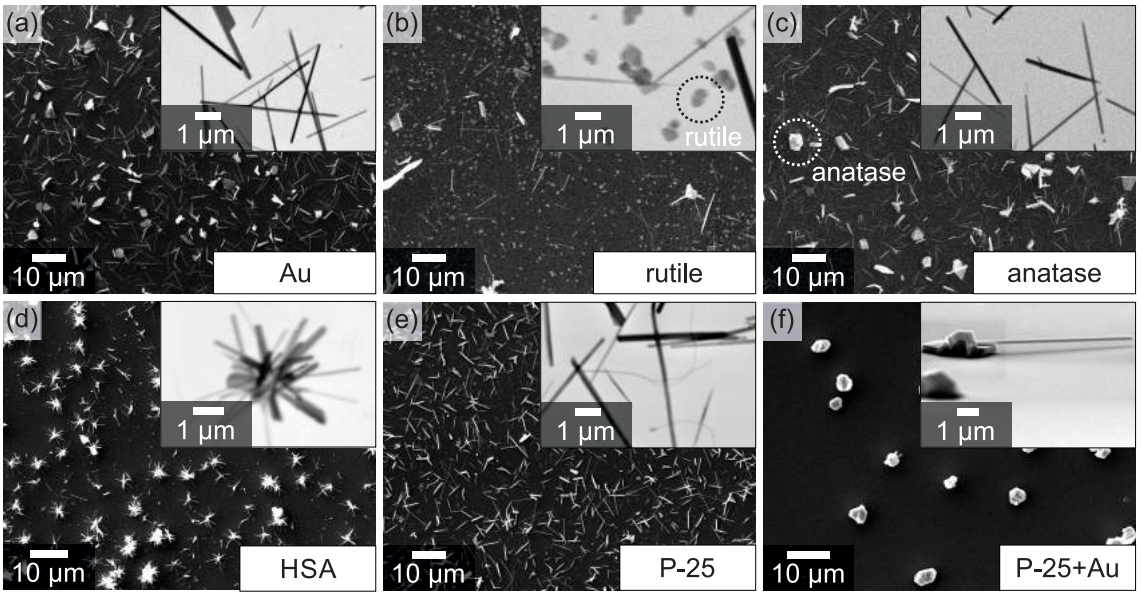

Fig. 4.2.3: SEM micrographs of as-grown $(Bi_{1-x}Sb_x)_2Se_3$ nanowires on Si substrates using (a) Au, (b) rutile (circle in inset indicates rutile agglomerate), (c) anatase (circle indicates anatase agglomerate), (d) HSA, (e) type P-25 TiO_2 powder, and (f) Au nanoparticles on P-25 supports. Instrument: Jeol JSM-6610LV; acceleration voltage: 20 keV.

The HSA catalyst results in many small nanowires that grow flat on the surface similar to P-25 as shown in Fig. 4.2.3(d). HSA nanoparticles are only ~4 nm in diameter and tend to form catalytically active agglomerations that lead to nanowire growth in a hedgehog-like structure (see inset) with the catalyst in the center.

Type P-25 TiO_2 grown nanowires in Fig. 4.2.3(e) have a more uniform length than pure anatase and rutile based nanowires. A detailed TEM study of this type is discussed below. Fewer other nanostructures are grown, since this catalyst mixture does not

agglomerate as much as the pure constituents.

The heterogeneous catalyst consists of 5-nm-diameter Au particles deposited on 20-nm-diameter P-25. The growth is homogeneous and plate-dominated, as shown in Fig. 4.2.3(f). Few nanowires protrude from plates either lying flat on the surface or growing under an angle. These nanowires are likely catalysed by individual Au nanoparticles.

The four, purely TiO_2 based catalyst solutions lead to results that have a quality comparable to the Au reference sample in terms of yield and homogenity. P-25 catalyst mixtures outperform the others in terms of surface coverage and nanowire purity (meaning less secondary nanostructures). Growth using the combined TiO_2-supported Au catalyst did not result in high density nanowires. However, for all other catalyst solutions we noticed many activated catalyst sites between the larger structures that had grown into nanodots. The heterogeneous catalyst hardly shows any such structures. It seems rather suited for mesa-to-mesa growth of nanowires spanning a gap as required for electrical transport measurements, as shown in the inset in Fig. 4.2.3(f).

The type of the catalyst particle not only affects the nanowire morphology, but also their stoichiometry. SEM-EDS measurements on as-grown nanowires are summarised in Table 4.2.2. Au catalyst results in binary Bi_2Se_3 nanowires, whereas all TiO_2 based catalysts enable the incorporation of Sb. Rutile and anatase grow nanowires with a similar stoichiometry. HSA anatase and P-25 grown nanowires have a much higher Sb concentration. The Se concentration is always higher than expected from the Bi_2Se_3 stoichiometry since Se deposits on the surface during the cool-down of the furnace are detected in EDS as well.

Next, nanowires obtained from Au and P-25 catalysed growth are compared in greater detail using TEM (see Fig. 4.2.4). TEM micrographs of the nanowire ends (tip and root) show the location of the catalyst particle. Figure 4.2.4(a) shows the root and the tip of an Au catalyst grown nanowire. The elemental composition is binary Bi_2Se_3 without

Table 4.2.2: Elemental nanowire composition for various catalysts determined by EDS (all concentrations in atomic-% with a systematic error of ±1%). TiO_2 catalyst supports the Sb incorporation, whereas no Sb could be found in Au catalysed nanowires.

	Au	rutile	anatase	HSA	P-25
			atomic-%		
Bi	22	39	34	19	28
Sb	0	1	2	16	7
Se	78	60	62	65	65

Sb dopants and the crystalline quality is poor. Au clusters are found that spread along the sidewalls of the nanowire similar to Fig. 4.1.3 above. Se precursor material is detected inside the Au cluster, but no Bi.

The composition of P-25 grown nanowires was determined by a 20-point average along the wire to be $(Bi_{0.81\pm0.08}Sb_{0.19\pm0.10})_2Se_3$ using TEM-EDS. Sb is distributed almost homogeneously along the body of the wire. The details of the distribution will be discussed in Section 4.4.1. Catalyst particles could not be found in most cases. A rare exception is shown in Fig. 4.2.4(b) where TiO_2 clusters stick to the root of a Bi_2Se_3 nanowire. EDS maps show that the nanowire body and nanoparticles are completely separated, as can be seen by comparing regions of high intensity in the map for Bi and Se with Ti.

Conclusion

Different types of catalyst particles were characterised by TEM and were used to grow $(Bi_{1-x}Sb_x)_2Se_3$ nanowires. The nanowires were analysed using SEM, EDS, and TEM. It was found that the quality of the nanowires grown using the TiO_2 catalyst P-25 is much greater than for all other catalyst types in terms of substrate coverage, uniformity, and crystallinity due to reduced coalescence of the particles. The mixed phase catalyst seems a promising discovery, but nanowire yield is too low to be further considered in this thesis. The key finding is that the TiO_2 catalyst P-25 stays well separated from the nanowire enabling contamination free growth. We have thus found and characterised

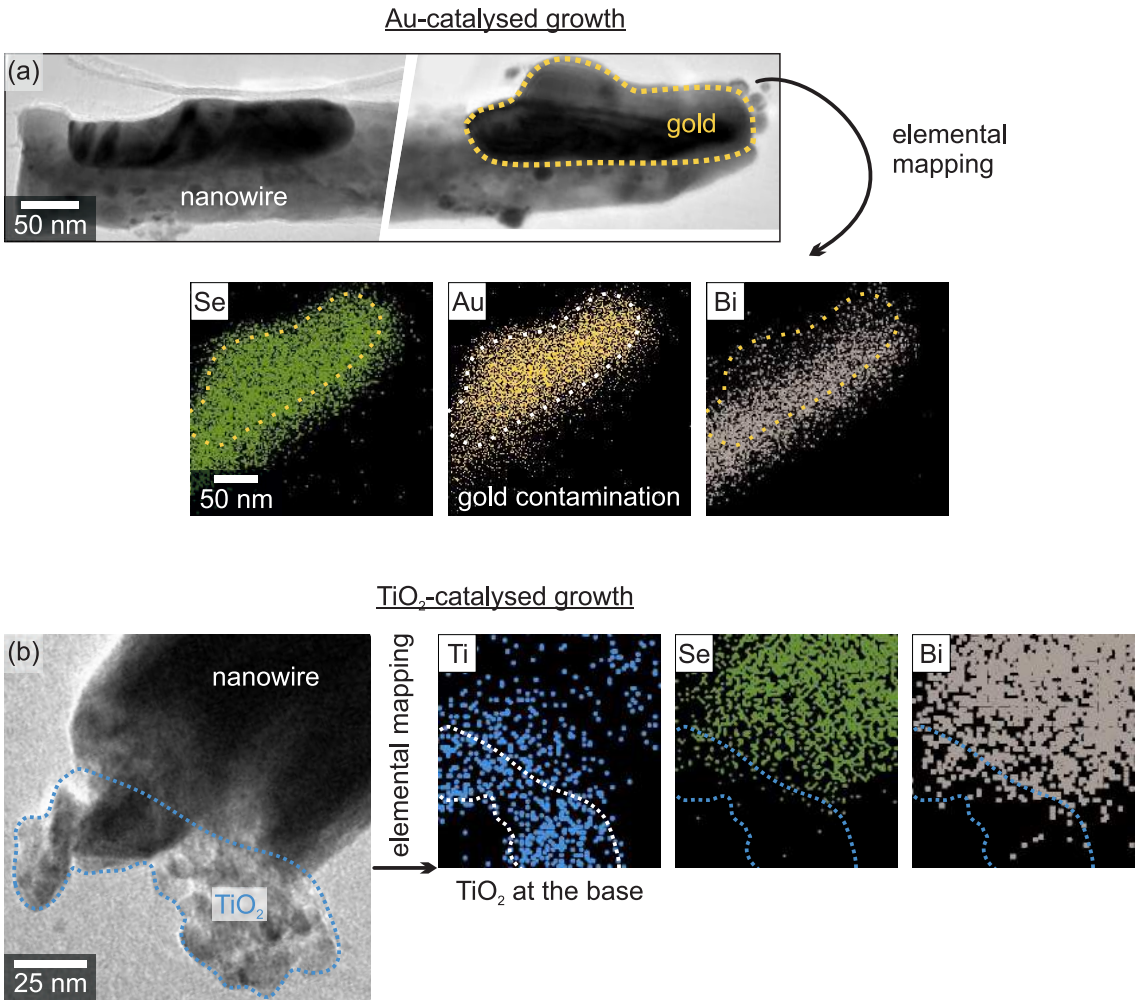

Fig. 4.2.4: (a) TEM micrographs taken of the root (left) and the tip (right) of a Bi_2Se_3 nanowire grown using Au catalyst. The region indicated by dots is a cluster of the initially 5-nm-diameter Au nanoparticles. It was further analysed using EDS. Color maps show the distribution of the three elements Se, Au, and Bi. Se is found inside the Au cluster, while Bi is not present. (b) Bi_2Se_3 nanowire grown using P-25 as a catalyst. Catalyst particles stick to the base and show no interaction with Bi or Se. Instrument: Jeol 2100.

an efficient and economic catalyst for nanowire growth.

4.2.2 Bi_2Te_3

The second part of this section about TiO_2-catalysed growth presents the growth mechanism of Bi_2Te_3 nano- and sub-micron belts and ribbons. In general, belt-like nanostructures show a rectangular cross-section with a height on the nanoscale range and a width from hundreds of nanometers to several μm. Nanobelts of semiconductors and metal oxides were intensely studied over the past two decades with electronic and sensor applications in mind [46, 128–133]. Materials with a layered crystal structure such as Bi_2Te_3 are ideal candidates for nanobelt growth since they preferentially grow parallel to the layers [46]. Adatoms prefer to attach to the *c*-plane to minimise their free energy. Chalcogenide nanobelts have been employed as building blocks for flexible and transparent electrode applications, hybrid Dirac materials (in combination with graphene), and photodetectors [134–136], however, little attention has been paid to a thorough understanding of the growth mechanism [137].

For thin film growth, one would intuitively assume that the preferential saturation of the stronger in-plane bonds results in a smooth, layer-by-layer step-flow growth, as shown in Fig. 4.2.5(a). In contrast, however, film growth is dominated by island growth from spiral-like features that progresses along the *c*-axis [47, 138, 139]. Nanowires and nanobelts, on the other hand, exhibit smooth surfaces and grow essentially single crystalline parallel to the plane, as shown in Fig. 4.2.5(b) [46]. Recent advances in research on chalcogenide nanowires, nanoribbons, and sub-micron belts call for an in-depth analysis of the growth of these structures [49, 140]. The common growth technique is catalysed vapour-transport. Atmospheric pressure (compared to low-vacuum vapour transport) and high carrier gas flow rates (100-300 sccm) are crucial for the growth of these Bi_2Te_3 structures [141, 142]. Catalysts such as sputtered Au thin films [46, 73, 143], colloidal Au nanoparticles with diameters between 5 nm and

20 nm [72, 77, 110], or TiO_2 nanoparticles [142, 144] can be employed to increase the yield and length of these structures. The growth conditions we used to carry out the following growth experiment are listed in Table 4.2.3. Growth is initialised by nucle-

Table 4.2.3: Parameters for the growth of Bi_2Te_3 sub-micron belts using TiO_2 nanoparticles as catalyst.

Parameter		**Value**
growth method		vapour transport
substrate	type	Si(100)
	catalyst coating	TiO_2 P-25
precursor		Bi_2Te_3
N_2 flow rate		150-300 sccm
growth temperature		585°C
ramp time		0
growth time		1 h
substrate temperature		~480°C
analysis methods		SEM, TEM, EDS

ation on the TiO_2 particles, proceeding via the formation of the first quintuple layers that grow away from the seeds, until finally the direct vapour-solid growth of further layers becomes possible. Two examples of unique growth morphologies are highlighted to pin down the epitaxial van-der-Merwe growth mode as a model for thin film growth. The results are equally applicable to Bi_2Se_3 and Sb_2Te_3 belts due to the similarity in the crystal structure.

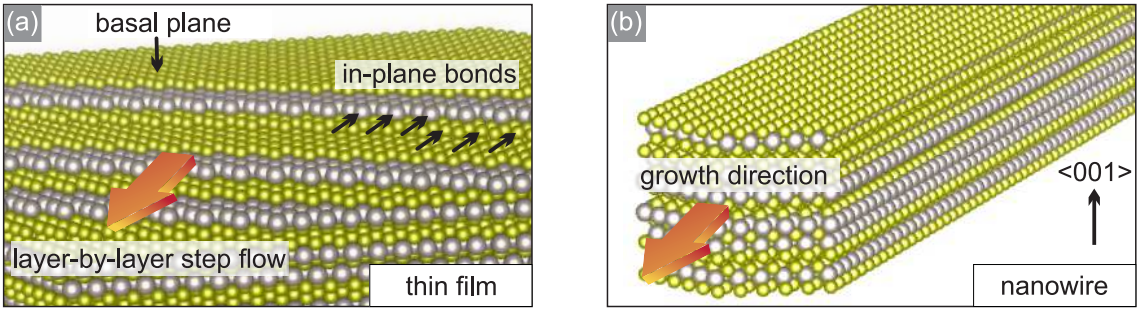

Fig. 4.2.5: (a) Side-view of a Bi_2Te_3 thin film. In-plane bonds are preferentially saturated relatively to bonds in the direction of the basal plane. (b) Nanowires grow perpendicular to the basal plane.

Microscopic picture of the growth

The microscopic model of Bi_2Te_3 belt growth consists of four steps: (1) chemical decomposition of the precursor molecules (at higher temperature) and transport to the substrate, see Fig. 4.2.6(a), (2) cluster formation on the substrate, (3) nucleation, and (4) crystallisation. Bi_2Te_3 vapour decomposes according to

$$2\,Bi_2Te_3 \longrightarrow 4\,Bi + 3\,Te_2$$

when evaporated as described above. Bi atoms and Te_2 molecules that are adsorbed onto the Si substrate either desorb again or migrate over the surface within their diffusion length, forming clusters as shown in the inset to Figure 4.2.6(b).

The stability of these clusters depends on temperature, cluster size, and binding energies. Bi_2Te_3 clusters are stable at a radius of about 10 nm at 300°C, as known from thin film growth [146]. The substrate temperatures for belt growth are 30–40% higher, leading to a higher density of smaller clusters. These initial liquid nucleation centers must be formed by Te molecules since at the growth temperature, the Bi_2Te_3 phase is only accessible via a Te-rich melt, as can be seen in the binary phase diagram in Figure 4.2.6(b). A Bi-rich melt, on the other hand, only forms Bi_2Te_3 at a growth temperature between 562°C and 586°C. Therefore, Bi-rich particles do not play a role in the growth of Bi_2Te_3 nanostructures presented here.

Note that we also observed Bi-rich Bi_2Te clusters on TiO_2 nanoparticles, as shown in Fig. 4.2.6(c), using EDS. This phase requires a Bi-rich melt and a temperature lower than 420°C. A possible reason for their formation is during cool-down of the furnace. The TiO_2 nanoparticles are embedded in the incoming material, therefore indicating a catalytic function during the nucleation phase. These clusters have not led to the formation of nanostructures and are found on substrates that also contain a variety of Bi_2Te_3 nanostructures. This behavior is similar to the formation of Bi_2Te_2Se islands that were identified as a product of catalytic interaction with Au nanoparticles [110].

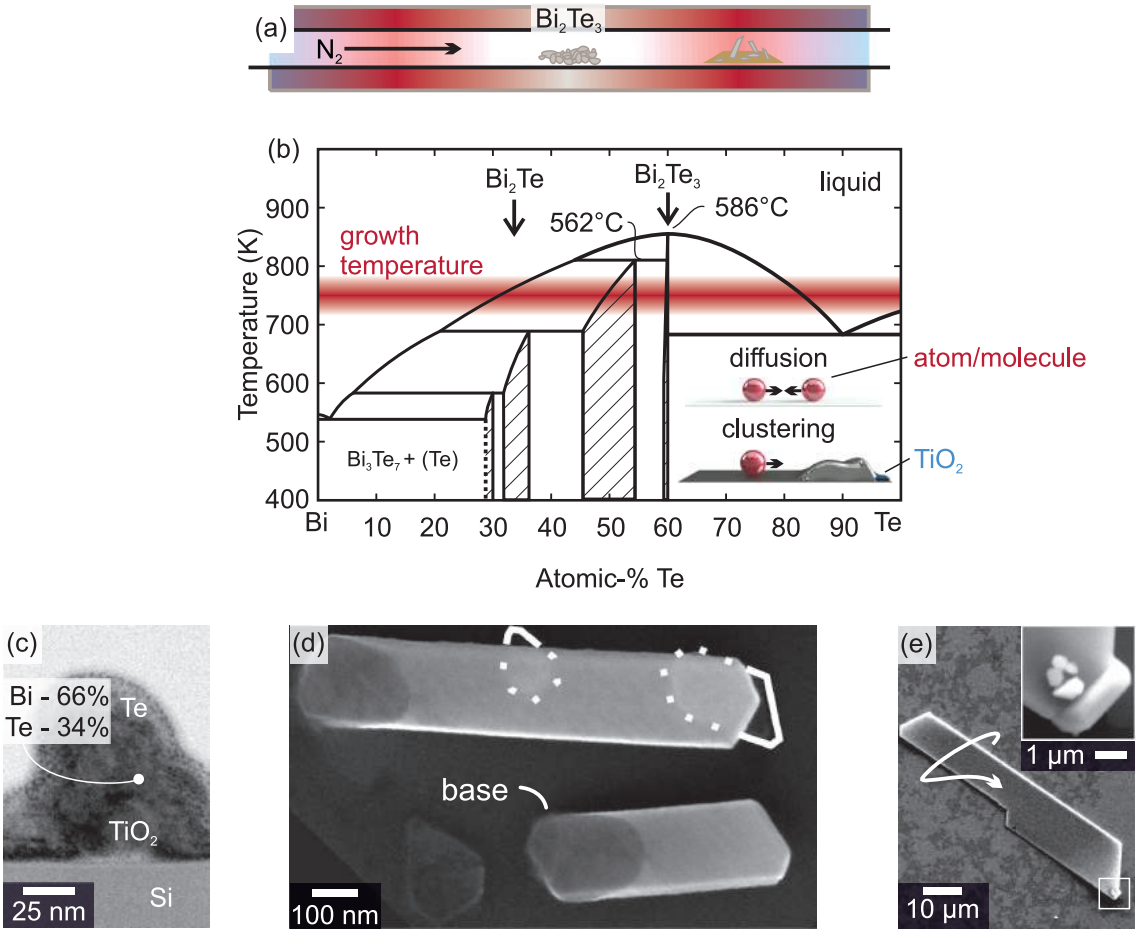

Fig. 4.2.6: (a) Bi_2Te_3 is evaporated in the center of the furnace and decomposes before reaching the substrate placed downstream at its cold end. (b) Simplified Bi-Te phase diagram after Ref. [145]. The growth temperature is marked by a red bar. The inset shows diffusion of atoms and molecules (red spheres) towards TiO_2 nanoparticles. (c) TEM image of a cluster that incorporates a TiO_2 catalyst particle (brighter circular areas), as can be seen in the TEM image. The composition is Bi_2Te (darker region), surrounded by an outer Te shell (brighter region). The composition is given in atomic-%, as measured by EDS. Instrument: Jeol ARM200F. (d) Free-standing belts (SEM micrograph) grown from a flat base (dark). The belts are transparent so that underlying plates (indicated by white outlines) are visible. Instrument: FEI Quanta 600 FEG; acceleration voltage: 30 keV. (e) Image of the base of a belt showing several particles at its root (inset) which potentially act as initial nucleation center. The belt has been rotated manually by 180° about its long axis (white arrow). Instrument: FEI Quanta 600 FEG; acceleration voltage: 30 keV.

TiO_2 catalyst particles were reported to increase belt yield and decrease the number of clusters in comparison with catalyst-free and Au-catalysed growth [142, 144]. Their role during the growth is less obvious than with Au nanoparticles since TiO_2 nanoparticles do not form large droplets at the tip of the belts during their catalytic activity. So, they either 'aide' self-catalysed growth and stay at the root of the belts or move forward with the tip without accumulating spherical precursor droplets. In particular, the tips of the two belts in an initial growth stage, pictured in Fig. 4.2.6(d), are free of any spherical clusters. Note, however, that VLS-type belts with amorphous catalytic tips have been reported in the literature [72, 137]. The thickness of the belts here is on the order of tens of nanometers since they are transparent to the electron beam. The root, on the other hand, is usually formed by a Bi_2Te_3 plate that is small compared to the size of the belt and visible in top-view images of the as-grown samples.

The belts grow in general from clusters and platelets at an angle to the substrate. Thus the following relationship is valid for the surface energy γ_{LS}(Si/droplet) between the substrate and a liquid Bi_2Te_3 droplet and the surface energy γ_{GS}(droplet/vapour) between the droplet and the gaseous vapour phase:

$$\gamma_{LS}(\text{Si/droplet}) > \gamma_{GS}(\text{droplet/vapour}). \tag{4.2.1}$$

Evidence from Bi_2Te clusters suggests that TiO_2 plays a role in the initial phase of the nanostructure growth, but beyond that, the belts grow in a self-catalysed process. Clusters and small plates are found at the root of belts in most cases, as shown in Fig. 4.2.6(e).

The effect of the crystal structure on the belt shape

When adsorbates diffuse over the surface of the belt, edges present an energy barrier since the number of nearest neighbors at the edge is reduced. These edges are multi-dimensional Ehrlich-Schwöbel barriers and they are important to consider for under-

standing the belt growth described below. The transition across an Ehrlich-Schwöbel barrier reduces the kinetic energy of the adsorbate. The space behind an Ehrlich-Schwöbel barrier is effectively a sink for adsorbates as they are more likely to settle once they are beyond the barrier. In this sense, an Ehrlich-Schwöbel barrier can also be seen as a reflective wall that contains adsorbates between boundaries. There are three types of edges, depending on their dimension, namely kinks (1D), steps (2D), and terraces (3D), as illustrated in Fig. 4.2.7 [147].

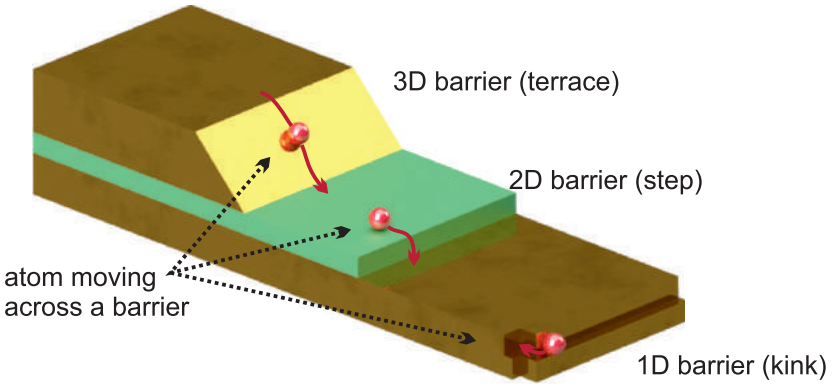

Fig. 4.2.7: Ehrlich-Schwöbel barrier in one, two, and three dimensions. Re-drawn after Ref. [147].

The shape of the tip of Bi_2Te_3 belts reflects the hexagonal crystal structure in the plane. Two growth directions, along the [210]- and [110]-direction, are commonly observed. The [110]-direction is energetically more favourable and therefore dominating [148]. The [210] growth direction is depicted in Fig. 4.2.8(a) and the tip shape observed in Fig. 4.2.6(e) is mapped onto the in-plane hexagonal coordinate system. The ratio between the (100) and (110) face fraction varies from belt to belt, whereby the complete absence of one of the faces was observed as well. A typical ratio is shown in the figure. The Bi and Te atoms appear ordered in a rectangular fashion along the projection in the [210]-direction. The varying fraction of the two growth front faces could be the result of a dynamic process aiming at lowering the energy by moving the tip position. Also, it is energetically favourable to avoid sharp tips since they offer less binding sites for adsorbates. This, however, also depends on the material. It was observed by others that Sn forms rather flat tips in nanobelts and that GaN nanobelts are terminated by

sharp tips [129, 149]. The growth along the [110]-direction is depicted in Fig. 4.2.8(b). In this case, the tip is formed of (210) and (120) faces, which again have a ratio that varies from belt to belt. The projection along the [110]-direction reveals columns of Bi-Te units tilted by 30° to the surface normal of the belt.

The growth directions were confirmed by analysing a thin lamella extracted from the Bi_2Te_3 belt, as shown in Fig. 4.2.8(c). Moreover, looking at the cross-section of the belt allows us to connect the shape of the belt with its microstructure. The cross-section of the belt measures 1.15 µm in width and 43 nm in height, as shown in Fig. 4.2.8(d) and Fig. 4.2.8(e), respectively. The tip is dominated by the (120) face, and has therefore a triangular shape. The sidewalls are partly aligned with the faces that are to be expected for [110]-oriented structures, however, tilted by 30° with respect to the surface normal, as shown in Fig. 4.2.8(e). Interestingly, the shape is not perfectly rhombohedral, as expected from Fig. 4.2.8(b), but more compact, similar to the outline of SnO_2 nanoribbons, which could be a result of the growth mechanism discussed in the following [150].

Step-flow growth mode for overgrowth

Larger Bi_2Te_3 belts consist of multiple layer stacks. The primary layer is the longest layer which forms the tip, as shown in Fig. 4.2.9(a). Secondary and tertiary layers grow on top, matching the width of the primary layer exactly, i.e., they do not extend beyond the boundaries of the primary layer. The reason for the difference in length could be the reduced supply of precursor material coming from the substrate due to the crossing of 2D Ehrlich-Schwöbel barriers on their way towards the tips. Thus, only adsorbates with the largest kinetic energy reach the tip, thereby slowing down the growth rate of the primary layer compared to the tertiary and secondary layer and increasing the belt's height or thickness. The layer-by-layer growth mode is known in the context of thin film growth as Frank-van-der-Merwe growth [151]. Most belts

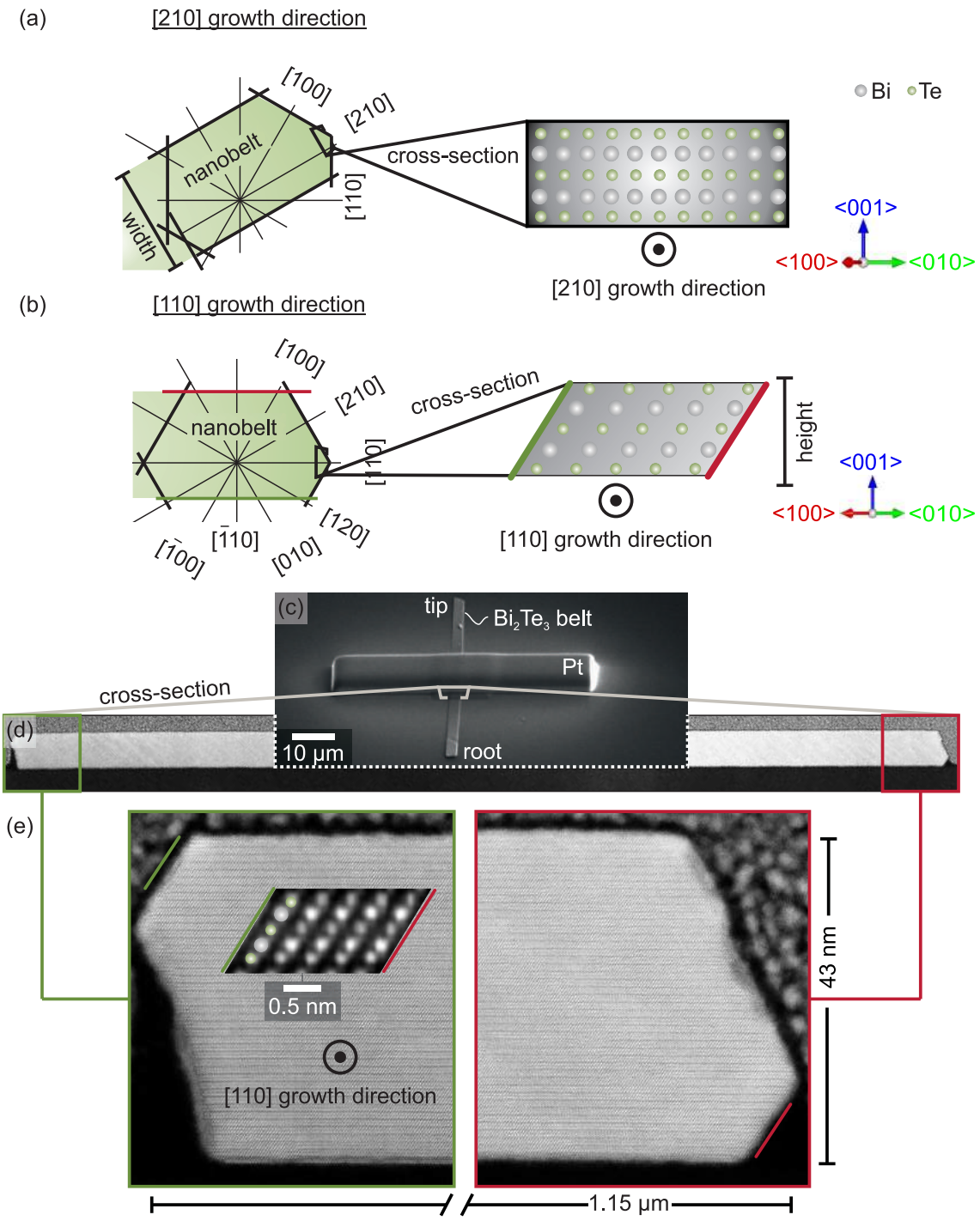

Fig. 4.2.8: (a) Belt (green) growing along the [210]-direction with in-plane hexagonal coordinate system superimposed on the tip. The (100) and (110) planes frame the tip. The projection down the [210]-direction shows the rectangular arrangement of Bi (grey circles) and Te (green circles) atoms on the right. (b) Belt growing along the [110]-direction. The (210) and (120) plane frame the tip. The projection down the [110]-direction shows a slanted arrangement of Bi (grey) and Te (green) atoms on the right. (c) SEM micrograph of a Bi_2Te_3 belt prepared for FIB machining with a Pt protection layer. A lamella is extracted from the region indicated by the rectangle. (d) Low-magnification TEM micrograph of the cross-section of the belt. (e) Magnified edges of the belt in cross-section. Lines (green and red) indicate faces that are parallel to atomic rows, as shown in the inset. The quintuple layers (bright), separated by the van der Waals gap (dark), are clearly visible. Instrument (c): FEI Quanta 600 FEG; acceleration voltage: 30 keV. Instrument (d,e): Jeol ARM200F.

grow straight as quasi 1D crystals, as shown in Fig. 4.2.9(b).

In the following, I will discuss two examples that are different and quite unique in terms of size and intriguing growth features. The first one is a branched belt. The branching point is located near the base, forming an angle of 60° with the direction of the main belt, as shown in Fig. 4.2.9(c). This corresponds to the [100]- or [010]-direction (which are indistinguishable), if the growth direction of the belt is [110].

The branch only measures half of the length of the main belt, despite the fact that the growth rates for both crystal directions should be identical. Here, the reason for the reduced growth rate of the branch is a cluster at its very tip, as shown in Fig. 4.2.9(d). Right at the base of the cluster, the width of the belt is strictly limited by the width of cluster. In-plane growth perpendicular to the growth direction on both sidewalls of the belt has led to a rough tapering similar to BiTe belts grown by Hsin *et al.* [152]. The sidewalls extrude on multiple locations at the same time, leading to the formation of indented triangles that gradually fill up at intersection points of two extrusions. These triangles are characteristic for broadening of belts. In fact, the branch itself is an extreme example of broadening, as indicated by a green line in Fig. 4.2.9(e), mapping to the edge of a triangle, i.e., the edge of an extension of the sidewall (bottom-side of the main part). Several layers extend from the branch intersection. Adsorbates attach to corners at the growth front so that the layers extend in a very compact growth front, as shown in Fig. 4.2.9(f).

Figure 4.2.9(g) shows triangles and steps with varying heights between 50 nm and 300 nm. Steps are slanted and smoothen the three-dimensional Ehrlich-Schwöbel barrier. The initial height of the primary layer can be estimated from the distance between the position of a triangle and the lower position of the primary layer to be ~300 nm, which agrees with a tripling of the thickness through layer-by-layer growth.

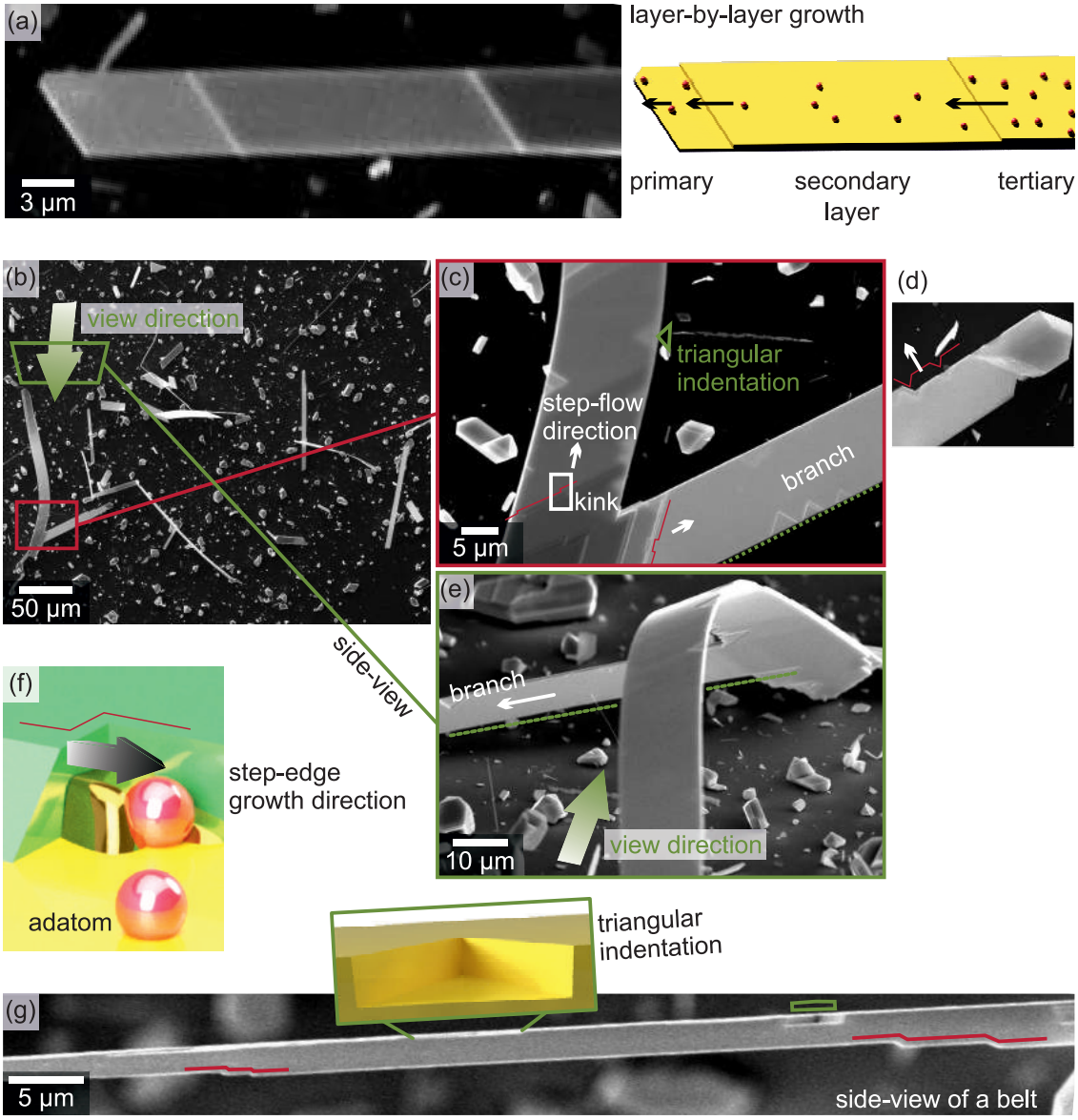

Fig. 4.2.9: (a) SEM image of the tip of a Bi_2Te_3 belt. Three layers, labelled primary, secondary, and tertiary layer, can be distinguished as gradually darker terraces. Adsorbate density decreases from tertiary to primary layer (metallic spheres). (b) As-grown sample with several belts and many clusters. The red rectangle indicates the branched belt in (c). The green rectangle indicates the side-view in (e). (c) Top view of the branching point. The angle between the branch and the main part is 60° (measured angle smaller due to tilt of the belt). Red lines indicated step edges. A white rectangle indicates the location of the process shown in (f). (d) The tip of the branch is formed by a cluster. The sidewall of the topmost layer is roughly tapered (red line). (e) View from underneath. The branch is an extension of one of the growth fronts towards the sidewalls (green line maps to green line in (c)). (f) Schematic drawing of the growth process. The secondary layer (green) grows on top of the primary layer (yellow) by migration of adatoms to an edge in the growth front indicated by an amorphous cluster (yellow) that moves parallel to the terrace step edge. (g) Side-view of a belt showing step edges (red) and triangular indentations (green) resulting from step-flow and broadening. Note that the triangular indentations appear as rectangles in side view. Instrument (b-d): FEI Quanta 600 FEG; acceleration voltage: 30 keV. Instrument(a,e,g): Jeol JSM-6610LV; acceleration voltage: 20 keV.

Step-flow growth against the adsorbate flow

The second unique example is a belt with a plate protruding perpendicular to its growth direction, as shown in Fig. 4.2.10(a). Precursor atoms adsorb onto the plate directly, i.e., not supplied by diffusion along the belt, since the layers on the plate grow against the diffusion direction, as can be seen in Fig. 4.2.10(b). A droplet is found on the surface of the belt in Fig. 4.2.10(b) which could be an example of a catalytic particle that initiates growth and is responsible for protrusions.

The tip of the belt is thinner than the bottom part, consistent with growth of additional layers at the bottom. A secondary layer grows with a growth front at an angle of 60° to the main face of the tip, as shown in Fig. 4.2.10(c). Thus, parallel alignment of primary and secondary layers, as seen in Fig. 4.2.9(a), is not necessarily the case which is another evidence for alternating growth fronts assuming that the starting orientation is the same for all layers. A droplet similar to the one shown in Fig. 4.2.10(b) is located at the tip. This could be a catalytic particle responsible for growth at the tip similar to the growth mode of the layers on top, as it is pictured schematically also in Fig. 4.2.9(f) (circle).

The sidewalls of the belt are strongly disrupted near the upper intersection of the plate with the belt. First, the width of the belt halves compared to the width at the lower end. Second, layers of various length and width extrude from the sidewalls. Third, the step-flow growth observed above is replaced by an island-type growth mode, fueled by material supplied from the edge of the plate. This is analogous to high flow growth experiments with Bi_2Te_3 that yield many small platelets instead of few long belts.

The situation is completely different at the other end of the intersection, i.e., between the plate and the belt, as shown in Fig. 4.2.10(e). Layers on the belt grow in step-flow growth towards the base. A wavy terrace edge is characteristic of 'growth against the adsorbate flow', i.e., a higher adatom flow from the lower steps than from the higher

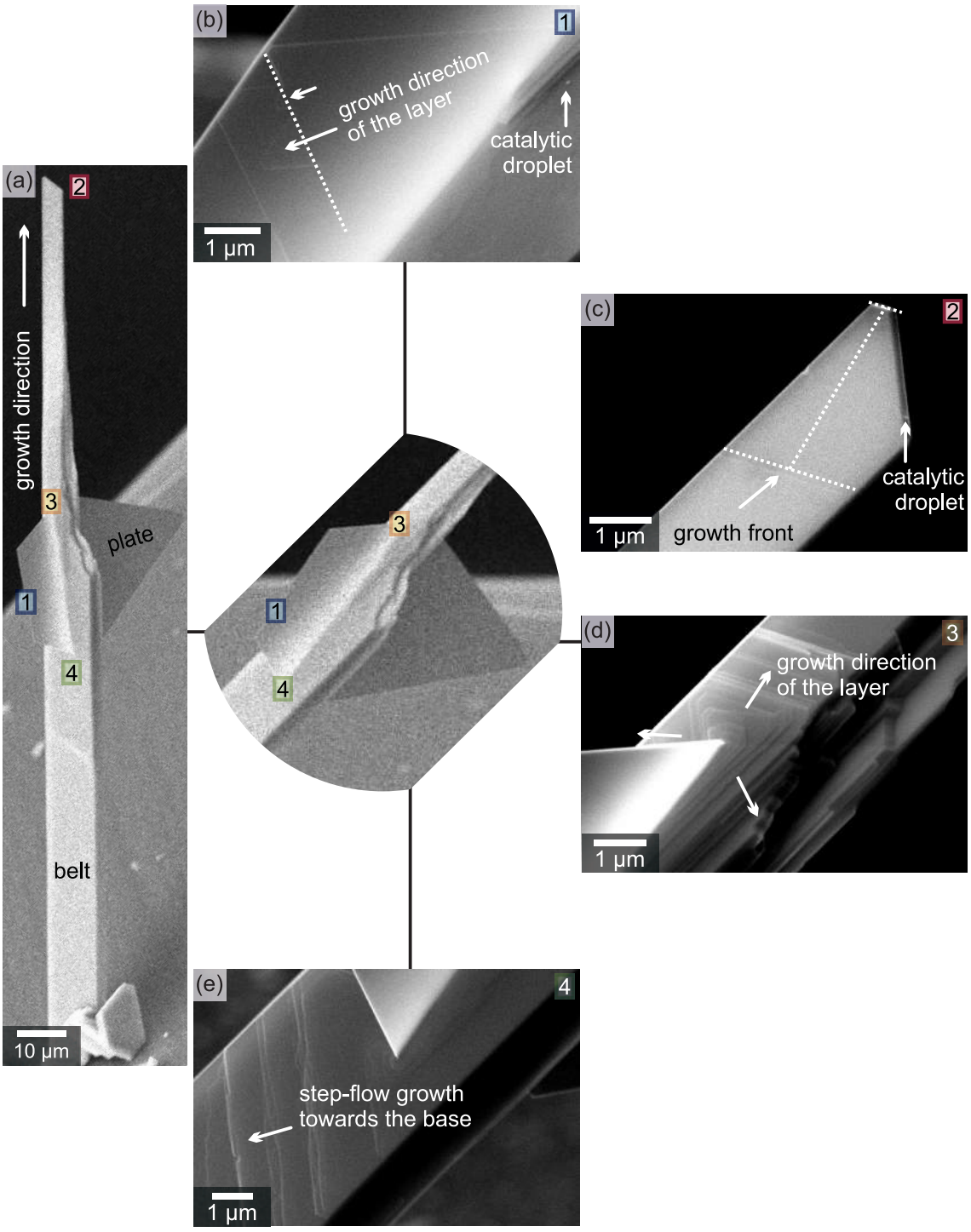

Fig. 4.2.10: (a) Bi_2Te_3 belt with a perpendicularly protruding plate (SEM micrograph). The growth direction is indicated by an arrow. Numbers indicate points of interest. (b) Layer-by-layer growth in triangular shapes (dotted line and white arrows) on top of the plate. The white arrow on the right indicates the formation of a droplet, which could act as a catalyst for the formation of protrusions. (c) The tip has two growth faces, as indicated. A spot on the wider growth front is indicated by a white arrow. The layer indicated by the dotted line grows with its growth front parallel to the narrower edge of the tip. (d) At the base of the plate additional layers grow in all directions, away from the intersection point (white arrows), and not only in one direction. (e) Towards the lower base of the plate wavy step-edges are observed, propagating towards the base of the belt. Instrument: Jeol JSM-6610LV; acceleration voltage: 20 keV.

steps [153].

Conclusion

Bi_2Te_3 belts grow in layers in a step-flow mode, starting from the root of the structure. Several layers can form simultaneously. Step edges are slanted and either parallel or rotated by 120° with respect to the tip, apparently alternating between the two orientations. The growth direction of the belts is [110]. Their width increases through broadening – a mechanism that leads to extrusions and triangular defects on the flat surfaces of the structures. TiO_2 catalyst particles play the role of a nucleation center for the adsorbates on the Si substrate. The catalyst may be present at the tip as well, potentially leading to tip-catalysed growth.

The demonstration of step-flow growth of Bi_2Te_3 nanobelts is an important finding since epitaxial growth is a key ingredient for the production of device materials. This growth mode has not been realised in MBE growth of Bi_2Te_3 thin films, which are dominated by the merging of growth 'islands'. Compared to MBE growth, vapour transport growth occurs at atmospheric pressure and for substrate temperatures twice as high as for MBE growth. The single-crystalline nature of the belts makes them potentially better suited for transport experiments and interesting candidates for the growth of heterostructure devices.

4.3 Catalyst-free growth

The use of Au, as observed for $(Bi,Sb)_2Se_3$ TIs above, is undesirable for electronic transport applications since Au contaminates the nanowire and catalyst atoms might become incorporated into the nanostructure during growth. The best alternative to using other catalyst materials such as TiO_2 is catalyst-free growth as it is the cleanest synthesis route for TI nanostructures [144]. This section demonstrates the catalyst-

free growth of Bi_2Te_3 nanostructures by MBE as a function of substrate temperature using the recipe outlined in Table 4.3.1. This is one of the first two reports of MBE grown TI nanowires [154, 155]. Samples were grown using a mini-MBE.

Table 4.3.1: Parameters for the MBE-growth of Bi_2Te_3 nanostructures from thin films of the same material.

Parameter		**Value**
growth method		MBE
base pressure		~5×10^{-10} Torr
substrate type		*c*-plane Al_2O_3
temperature	Bi cell	490°C
	Te cell	470°C
	Te hotlip	700°C
	substrate	208–256°C
Bi:Te flux ratio		1:10
growth	rate	~70 Å/min
	time	15 min
analysis methods		SEM, TEM, AFM

4.3.1 Tuning the growth conditions

Thin films of the $(Bi,Sb)_2(Se,Te)_3$ family are characterised by an island growth that is spiral-like [156]. The islands are mostly hexagonal which reflects the underlying rhombohedral crystal structure for a growth direction along the c-axis. Most islands ultimately grow into triangles. This is a result of the distance between the corners of the triangle being larger than the diffusion length of the surface adatoms [146]. Adjacent terraces are separated by step heights of ~1 nm, which correspond to one quintuple layer. The explanation for this counter-intuitive growth mechanism is the pinning of 2D growth fronts at irregular substrate steps or domain boundaries [157].

Flux and substrate temperature are the two main growth parameters for tuning the quality and growth type of MBE grown TI samples [158, 159]. The Bi flux controls the growth rate, whilst Te is supplied at an overpressure to suppress re-evaporation.

Nanostructures are formed at high substrate temperatures compared to temperatures typically used for thin film growth. When the substrate temperature is too low, film growth is characterised by small orientationally disordered growth domains [138].

The temperature series in Fig. 4.3.1 shows how the density and shape of the nanostructures are tuned within the substrate temperature range of 180–260°C. The composition of the film and the vertical structures on top is Bi_2Te_3, as measured by TEM-EDS. Other parameters such as the growth rate, which was varied between ~7–70 Å/min, do not change the growth results as much as the substrate temperature.

Two types of structures are observed at 208°C in Fig. 4.3.1(a). One type are wedge-shaped rods that are aligned with the steps of the underlying thin film (zoom 1, red). The other type are long sheets that resemble thin film segments that have grown perpendicular to the surface (zoom 2, green). Nanoribbons with a tunable width between 50 nm and several 100 nm can be grown above this temperature. A lower temperature leads to broader nanoribbons, as can be seen in Fig. 4.3.1(b) in comparison to Fig. 4.3.1(c). The substrate coverage is smallest for the highest temperature, 260°C, as shown in Fig. 4.3.1(d). The width of some of these nanoribbons is below 50 nm. Their tips are usually terminated by a 30° inclined edge consistent with the catalysed growth by vapour transport.

4.3.2 A nanoscale look at the structures

The base plays an important role in the nanostructure growth since the tip shows no evidence of catalytic activity. AFM was performed in order to investigate the base in more detail. Figure 4.3.2(a) shows an AFM image of the low-temperature sample presented in Fig. 4.3.1(a), which was selected for AFM analysis because the typical nanostructure heights were small enough to allow for imaging without significant tip damage.

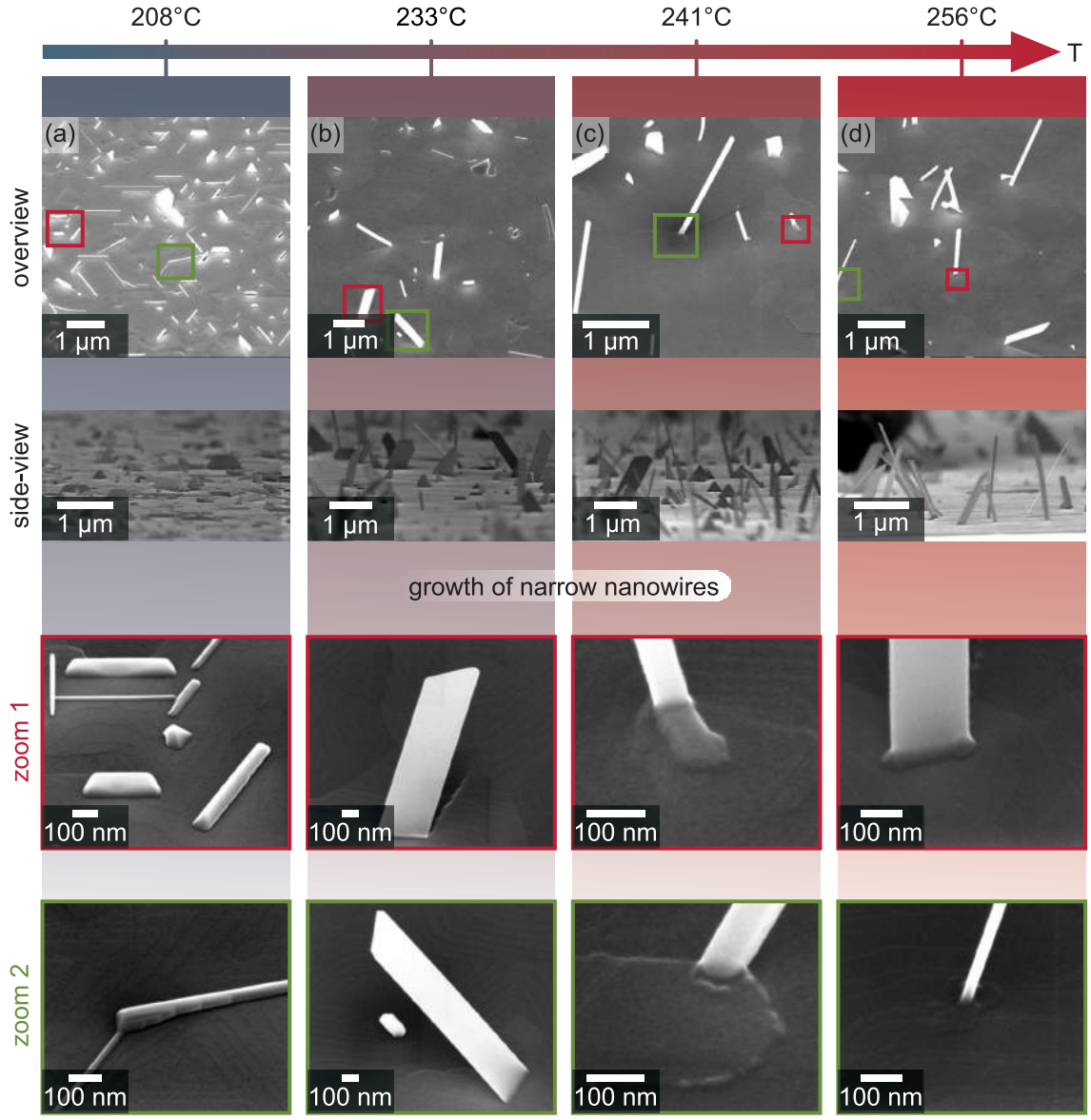

Fig. 4.3.1: Temperature dependence of the Bi_2Te_3 nanostructure growth. The growth conditions are otherwise the same for all four temperatures. The two upper rows contain top- and side-view images of the nanostructures for each temperature, respectively. The two lower rows show top-view zooms of selected areas. (a) Growth at 208°C shows flat nanostructures. (b) Growth at 233°C shows broad nanoribbons. (c) Growth at 241°C shows a mixture of broader and narrower nanostructures. (d) Growth at 256°C shows mainly narrow nanowires. Instrument: FEI Magellan 400 XHR SEM; acceleration voltage: 5 keV.

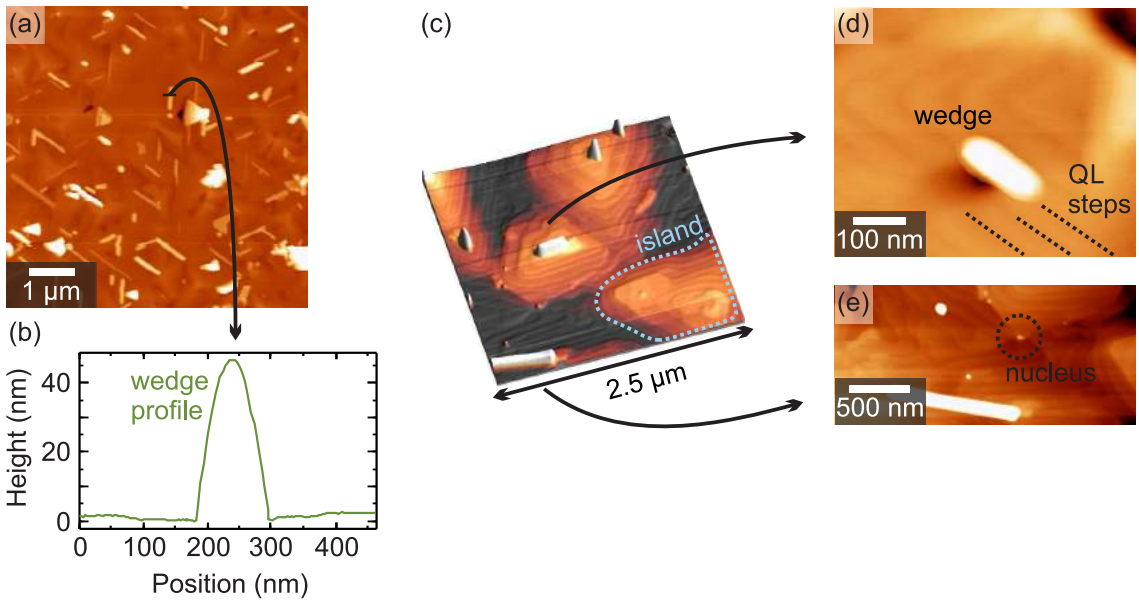

Fig. 4.3.2: (a) AFM overview image of the Bi_2Te_3 sample grown at 208°C corresponding to Fig. 4.3.1(a). (b) Line scan across a wedge. (c) Pseudo-3D image showing nanostructures and spiral-like islands. (d) Close-up of a wedge as indicated in (c). The black dotted lines mark quintuple layer steps. (e) Nucleus (black dashed circle) that might be a starting point for further nanostructure growth.

Two features dominate the image: wedge-shaped structures and thinner, plate-like structures. The height profile across a wedge structure in Fig. 4.3.2(b) shows a height of ~40 nm and a width of ~100 nm. The pseudo-3D image in (c) shows the hexagonal islands typical for the Bi_2Te_3 thin film. Wedge-shaped structures, as shown in (d), were found to occupy a single terrace in width. The growing wedge strongly disturbs the spiral-like island growth of the underlying film and appears to be consuming material from the lower terraces. The plate-like structures in Fig. 4.3.2(e) that can also be seen in Fig. 4.3.1(a) (red frame) are most common for low-temperature growth and are multilayered with a stepped surface morphology.

Nuclei which have not seeded nanostructure growth, and have yet to be overgrown by the converging islands, are commonly found at the lowest point of the surface morphology. They appear as bright features in the AFM images as in Fig. 4.3.2(e) and resemble small 'defects' that sit on the film's surface.

TEM was used to provide detailed structural information on the sample grown at the

highest growth temperature. Figure 4.3.3 shows TEM (top-view) micrographs of two ~140 nm wide nanoribbons grown at 256°C. The growth is along the [110]-direction, as indicated in (a).

Again, the nanoribbon tip has a slanted edge which is inclined by 30° with respect to the top plane. An additional, shorter edge indicated by the small arrow in (a), reflects the symmetry of the crystal structure and resembles the transition from hexagonal to triangular islands known from film growth. The high-resolution TEM image in Fig. 4.3.3(b) reveals the high-quality, single-crystalline nature of the structures. The distance between the lattice planes shown in (b) is ~2.2 Å, which corresponds to the spacing of the (110) planes. The lattice parameters for hexagonal Bi_2Te_3 are $a = 4.395$ Å and $c = 30.44$ Å (JCPDS 82-0358). The Fourier transform is shown in (c) and reveals the hexagonal symmetry of the crystal structure ($R\bar{3}m$ for Bi_2Te_3).

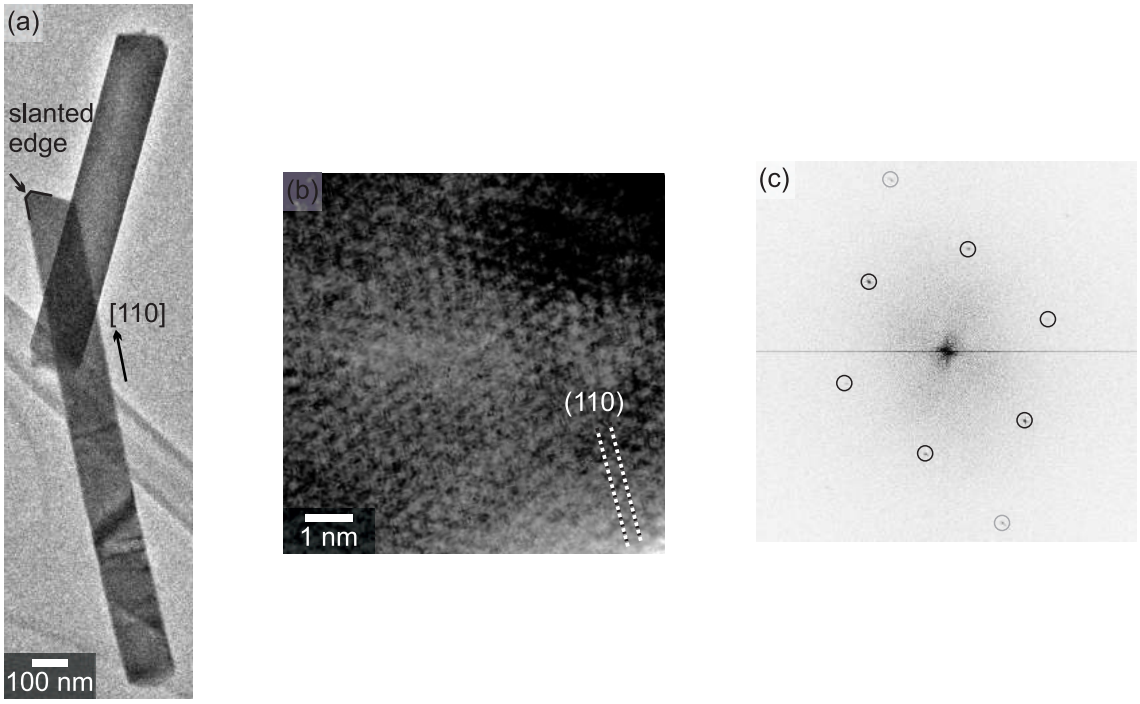

Fig. 4.3.3: (a) TEM image of Bi_2Te_3 nanoribbons growing along the [110]-direction. (b) High-resolution TEM image with the (110) lattice planes indicated by the dotted lines. (c) Fourier transform of (b) showing the hexagonal symmetry. Instrument: Jeol 2100.

4.3.3 Growth mechanism

The above analysis warrants a discussion of the possible growth mechanism for the nanoribbons. As shown in the temperature series in Fig. 4.3.1 (specifically for the higher resolution images in the lower rows) as the temperature is increased, the nanostructures undergo a continuous transformation from densely populated predominately wedge and plate-like growth at low temperatures, to a reduced density consisting of wide nanoribbon features at intermediate temperatures, and finally to sparely populated narrow nanoribbon growth at the higher temperature limit. These results suggest that the seed must play a critical role in the growth of the nanostructures and determine their shape.

Careful analysis of the roots of the nanoribbons in the temperature series in Fig. 4.3.1 (lower rows) and the AFM study in Fig. 4.3.2(c,d) reveals that the nanoribbons grow from step edges as in Fig. 4.3.1(c), *zoom 2*, or originate from the center of the islands as in Fig. 4.3.1(c), *zoom 1*. AFM imaging further indicates the presence of several small seeds on the film surface (Fig. 4.3.2(c,e)) which are preferentially arranged at step-edges, the centers of islands, and the intersection of grain boundaries. The exposed seeds nucleate a laterally-confined sheet growth, which occurs simultaneously with the island film growth but will result in the formation of a nanostructure. When the laterally growing sheet reaches the step edge to a lower-lying terrace, the growth direction changes from in-plane to out-of-plane and vertical nanoribbons emerge. Growth of the nanoribbons then continues along the [110]-direction as the base of the nanoribbons are aligned with the step edges of the underlying terraces. This growth scenario is schematically illustrated in Fig. 4.3.4(a), and supporting SEM data is shown in Fig. 4.3.4(b).

While the origin of the driving force for the upward bending is not yet clear, it is not likely the result of stress due to lattice or thermal expansion mismatch between the film and the ribbon, however, a thermal gradient may develop due to their different

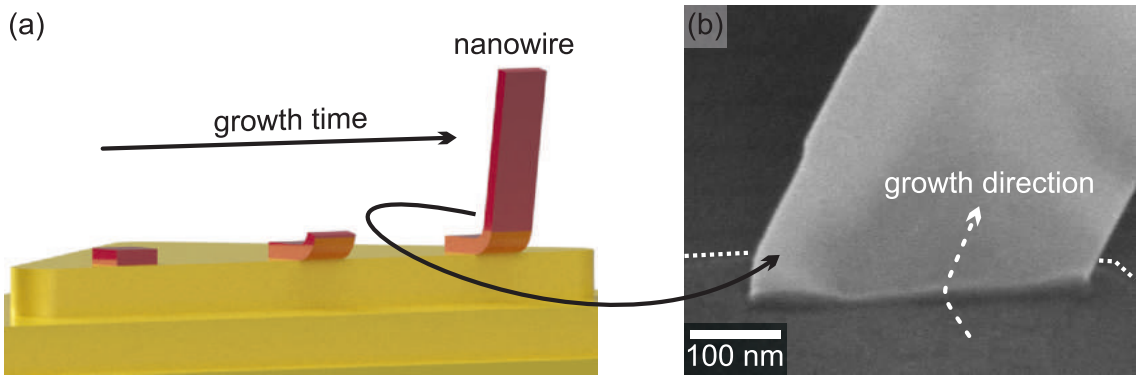

Fig. 4.3.4: (a) Illustration of the nanoribbon growth as a function of time t. (b) SEM image of the root of a nanoribbon. The step edge is indicated by a dashed line. The arrow indicates the growth direction, first in the film plane, and then, after bending, in the vertical direction. Instrument: FEI Magellan 400 XHR SEM; acceleration voltage: 5 keV.

thermal radiation characteristics.

Conclusion

A systematic study of the catalyst-free MBE growth of high-quality single-crystalline Bi_2Te_3 nanostructures on c-plane sapphire was carried out. By keeping the flux ratios of Bi and Te and the growth time constant, nanostructure growth was found to be controlled via substrate temperature. At low temperatures, a high seed density leads to the formation of short and wide nanostructures. At high temperatures, where the seed density is much lower, long and narrow nanoribbons growing along the [110]-direction were observed.

4.4 Growth mechanisms of non-layered materials

VLS is in some cases a good starting point to explain the growth of nanowires but it is usually not representing the whole picture. In the following, I will describe the details of the growth mechanism in Sb-doped Bi_2Se_3, Cd_3As_2, and SnO_2 nanowires.

4.4.1 Sb:Bi_2Se_3 nanowires

This section expands on the material used in Section 4.2.1 based on the following observations:

- Sb-doped Bi_2Se_3 can have an orthorhombic crystal structure, which is characterised by quasi 1D, conducting atomic chains, as will be demonstrated in Chapter 5. So the growth mechanism of such a material cannot be explained within the models developed in Section 4.2.2 for layered materials.
- No alloyed particle is located at the tip or the base as required by VLS, as shown in Fig. 4.4.1(a).
- The tip shape is slanted towards a Sb-rich region, as shown in Fig. 4.4.1(b).

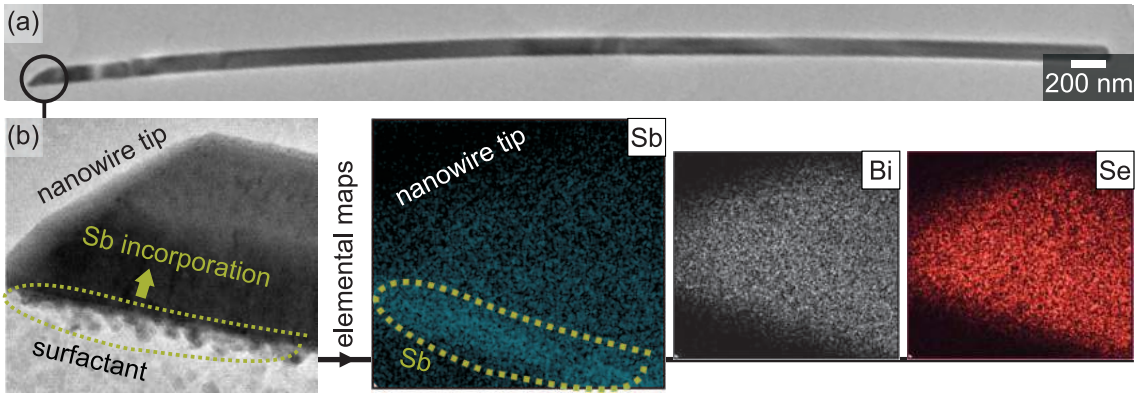

Fig. 4.4.1: (a) TEM micrograph of a Sb-doped Bi_2Se_3 nanowire. No spherical catalyst particle is found at the tip (black circle) and root. (b) EDS maps of the tip show a Sb-rich region at the longer side of the body. Instrument: Jeol 2100.

Hence, the growth can be described in the framework of solid-phase seeded vapour-solid growth, whereby the role of Sb has to be further analysed [122, 160].

Through EDS measurements on catalyst sites that did not yield nanowires we know that the TiO_2 is Se-rich, i.e., it accumulates more Se than expected by the 2:3 Bi:Se ratio of Bi_2Se_3. This suggests that initially a Se containing liquid is formed on the surface of TiO_2. The absorption of Bi atoms drives nucleation as in the case of Au above. One-dimensional growth is achieved through Sb surfactant action in the vicinity of the tip, as illustrated in Fig. 4.4.2. The role of a surfactant in MBE is to support diffusion of other atoms impinging on the surface [161, 162]. When these adatoms reach a proper site they are incorporated by exchange with a surfactant atom. In the present case Sb passivates the top sidewalls. Adatoms are driven up to the tip of the nanowire and the nanowire grows from the top which results in a slanted tip shape. Sb is incorporated during this process as a dopant.

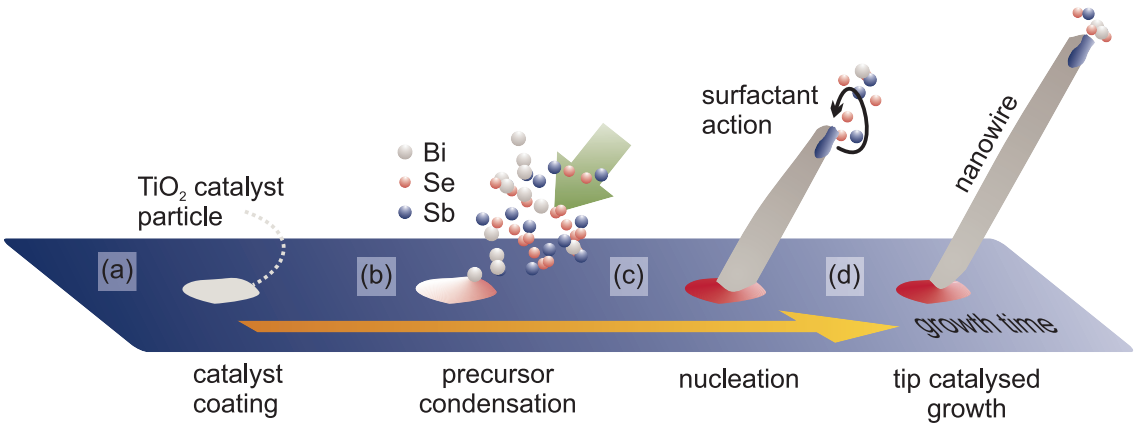

Fig. 4.4.2: Nanowire growth mechanism for TiO_2 catalyst nanoparticles. (a) TiO_2 particles (white) are deposited on the substrate. (b) The Bi-Sb-Se precursor vapour condenses onto the TiO_2 surface, whereby the TiO_2 particles only initiate the growth. (c) Incoming precursor material is mainly absorbed at the tip, but also at the sidewalls mediated by Sb surfactant action. (d) The nanowire grows into a long crystal.

4.4.2 Cd_3As_2 nanowires

The most characteristic growth feature of Cd_3As_2 nanowires is the exclusive growth from Cd_3As_2 clusters. Whereas Bi_2Se_3 nanowires only sometimes grow from plates, Cd_3As_2 nanowires grow star-like from a relatively large polyhedral, Cd-rich cluster.

Most of the research on Cd_3As_2 so far has been carried out in the context of II-V compound semiconductors. Omari *et al.* reported the non-catalytic vapour-solid growth of Cd_3As_2 nanowires from a Cd_3As_2 film, ruling out any effect of Cd on the growth [163]. For other II-V compounds such as Zn_3As_2, on the other hand, it is known that Zn particles act as self-catalysts in the VLS growth of nanowires [164].

III-V compound nanowires are usually grown in a self-catalysed process with or without a group-III element acting catalytically and being located at the tip of the nanowire. It was shown for InAs that the presence of the catalytic tip depends on the group-V flux during cool-down [165]. In the presence of the group-V element the catalytic tip is consumed whereas a reduction of the flux preserves the group-III element droplet. Intuitively, one would assume that this scenario can be applied to II-V growth too, but experiments on the group II-V Cd_3As_2 nanowires did not show a group-II element-rich stoichiometry towards the tip. In the following, the growth of Cd_3As_2 nanowires will be characterised and a model of the growth will be presented.

Optimisation of the growth conditions

Samples are grown using the parameters listed in Table 4.4.1. Crystalline growth occurs only in a very small temperature window. The Si substrates then appears black to the naked eye. Dense Cd_3As_2 nanowire ensembles ('wool') and micron-sized crystal rods grow from the inner walls of the quartz tube and on the quartz boats. The most important growth parameter for Cd_3As_2 is the flow rate of the carrier gas at a given furnace temperature. For a flow rate of 300 sccm, a thick layer composed of Cd_3As_2

Table 4.4.1: Experimental parameters for the growth of Cd_3As_2 nanowires.

Parameter		**Value**
growth method		vapour transport
substrate	type	Si(100)
	catalyst coating	Au, TiO_2, none
precursor		Cd_3As_2
N_2 flow rate		25 sccm
growth temperature		750°C
ramp time		20 min
growth time		60 min
substrate temperature		200°C
analysis methods		SEM and TEM

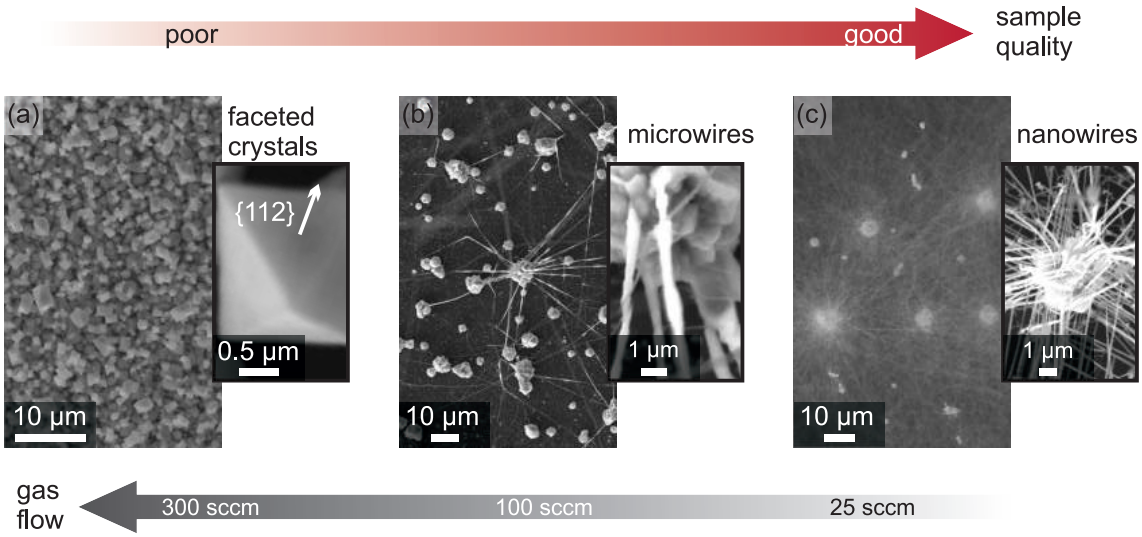

Fig. 4.4.3: SEM micrographs of as-grown Cd_3As_2 samples as a function of carrier gas flow. (a) 300 sccm: A thin film of Cd_3As_2 microcrystals is grown. In the inset an arrow indicates a {112} lattice plane of one of the microcrystals. (b) 100 sccm: Micro- and nanowires extrude from clusters. The inset shows the roots of the wires with respect to the cluster surface. (c) 25 sccm: Nanowires extrude from the clusters forming dense networks. The nanowires grow along preferential directions, i.e., <112>, as can be seen in the inset. Instrument: Jeol JSM-6610LV; acceleration voltage: 20 keV.

microcrystals grows on the Si substrates, as shown in Fig. 4.4.3(a). The crystals have a pyramidal shape enclosed by {112} facets as in Fig. 4.4.3(a), inset. The typical size of a single crystallite is ~2 µm. At 100 sccm, large clusters with a diameter of ~10 µm initiate the growth of most nanowires, as shown in Fig. 4.4.3(b). The wire diameter can be irregular and rather large (up to 0.5 µm), as shown in Fig. 4.4.3(b), inset. The lowest available flow rate was 25 sccm, however, growth also occurs at zero flow rate of the carrier gas, purely driven by diffusion. The size of the clusters from which the nanowires protrude, as can be seen Fig. 4.4.3(c), is by 50% smaller than at a flow rate of 100 sccm. More and thinner nanowires with diameters as small as 10 nm are achieved. The growth directions of the nanowires are intimately connected with the orientation of the facets from which they originate, and thus the underlying crystal symmetry, as displayed in Fig. 4.4.3(c), inset.

The catalytic tip in high magnification

The nanowires are tapered with a root diameter on the order of several 100 nm. Close to the tip the nanowires are usually kinked. The tapered growth is confirmed up to the very top of the nanowire. In Fig. 4.4.4(a) the nanowire has an initial diameter of 80 nm and tapers off to below 50 nm at the tip. A darker shading compared to the rest

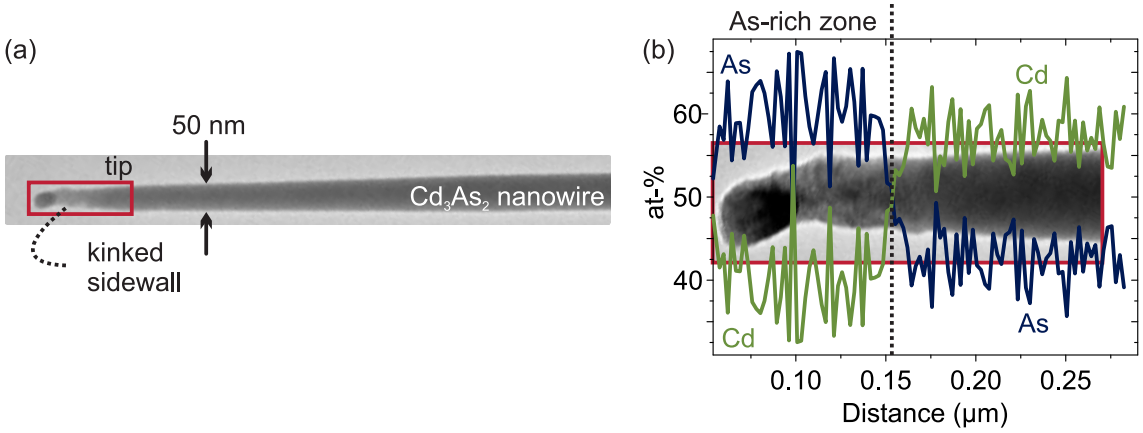

Fig. 4.4.4: TEM micrograph of a Cd_3As_2 nanowire tip. (a) The nanowire is tapered with a tip diameter below 50 nm. (b) EDS linescan of the tip of the nanowire. The scanned section is indicated by a red rectangle in (a). The As and Cd concentrations (in atomic-%) along the nanowire are shown in blue and green, respectively. Instrument: Jeol 2100.

of the wire indicates a greater thickness for the same materials composition. The tip is As-rich and this 'inverted' composition persists up to 150 nm below the tip, where the correct Cd_3As_2 stoichiometry is abruptly restored, as can be seen in Fig. 4.4.4(b). This transition is also reflected in the shape of the sidewalls which are kinked and coarse up to 150 nm below the tip, and become abruptly smooth and straight beyond that interface (all the way down to the root). This represents in a way an inversion of the common scenario for II-V nanowires in which the group II material has a higher concentration at the tip and catalyses the growth. It is also in contrast to III-V materials where the group III element acts as catalytic element and the group V element is absorbed into the liquid droplet during VLS growth.

Growth mechanism

Cd has a higher vapour pressure than As at the investigated growth temperatures. Both elements also have a higher vapour pressure than Zn, In, and Ga making it hard to draw conclusions from comparisons with these arsenides, since for Cd_3As_2 we cannot assume As-rich conditions.

At an early growth stage the growth is catalysed by Cd droplets that can be seen in Fig. 4.4.5(a). At a substrate temperature of 200°C, which is below the melting point of bulk Cd (321°C), the temperature gap can be overcome by melting-point depression, which can amount to more than 100°C for nanometer-sized metals [166].

The Cd droplets are formed at random sites on the substrate surface. Impinging As atoms desorb from the surface unless they interact with the liquid Cd droplets. A liquid solution is formed that will readily crystallize given the fact that the solubility limit of As in Cd is only 5% at 465°C [167]. Further As addition leads to the crystallization of Cd_3As_2 forming small crystallites and clusters. Their sizes depend on the growth time and temperature, and the flow rate. It can be assumed that no further accumulation of liquid Cd occurs since Cd-rich areas can only be found in gaps between the crystalline

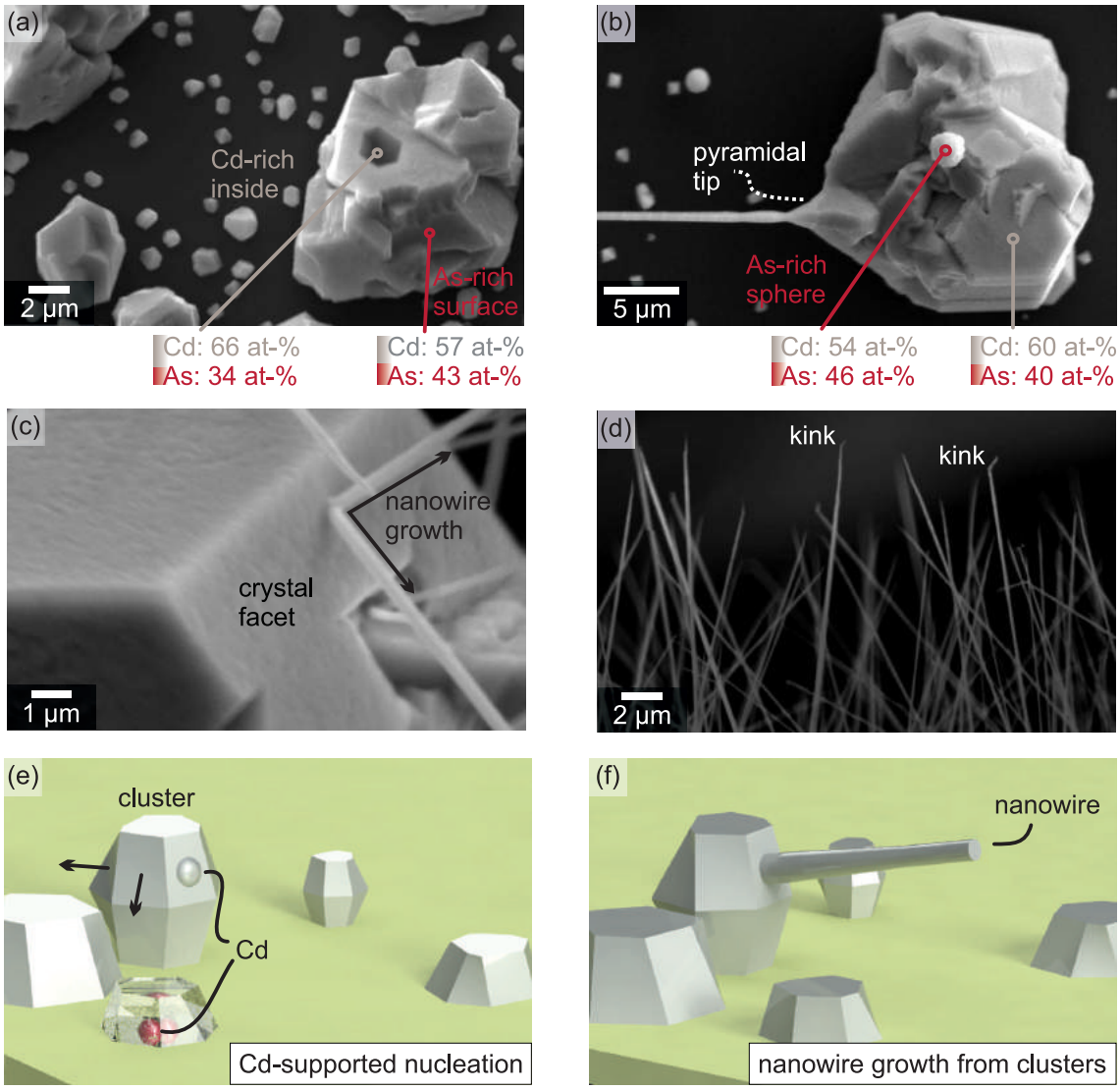

Fig. 4.4.5: (a) SEM image of Cd_3As_2 clusters. Two EDS measurement spots are highlighted. The hole in the top facet of the cluster is Cd-rich whereas the side facet is As-rich. (b) SEM image of a Cd_3As_2 cluster that has nucleated the growth of a nanowire via the formation of a pyramidal tip. EDS at the indicated spots reveal that the white sphere is As-rich, whereas the smooth top facet has perfect Cd_3As_2 stoichiometry. (c) SEM high resolution image of a crystal facet. Two nanowires emerge from a spherical structure on the facet. (d) Side-view SEM image of densely grown nanowires. A kink or elbow-like structure appears at the tip of all nanowires. (e) Sketch of the first phase of the growth. Crystalline clusters of different sizes grow on the Si surface. A Cd-rich phase (red sphere) is located in the center of the cluster. Cd also accumulates on the facets (enlarged surface feature). Arrows indicate nanowire growth occurring from all facets. (f) Nanowires grow from Cd-rich spots on the {112} facets via vapour-solid growth. Instrument: Jeol JSM-6610LV; acceleration voltage: 20 keV (a-d).

clusters shown in Fig. 4.4.5(a). The growth of nanowires always starts from such clusters. The root of the nanowires can be the tip of a pyramid, as shown in Fig. 4.4.5(b); an edge, as shown in Fig. 4.4.3(b), inset; or a crystal facet, as shown in Fig. 4.4.5(c). Presumably the Cd-rich atmosphere leads to nucleation centers as indicated on cluster facets shown in Fig. 4.4.5(e). The nanowires grow in a tip-based vapour-solid growth mode, that is illustrated in Fig. 4.4.5(f). However, judging from the tapering of the nanowires which are narrow at the top and wider at the root, growth also proceeds by crystallization on the side walls. The vapour-solid growth mode of Cd_3As_2 can be understood as the inverse of the vaporisation of Cd_3As_2 [168]. When Cd_3As_2 is thermally vaporised, Cd evaporates first and leaves an As-rich surface behind. The Cd vacancies can be replenished by Cd diffusion from the bulk if the surface-to-volume ratio is small. Inversely, if a given crystal is exposed to Cd and As vapour, it will grow an As-rich layer that gradually incorporates incoming Cd atoms. Therefore, the tip of nanowires and the surface layer of clusters are As-rich.

The occurrence of a kink close to the very tip of the nanowires, as can be seen in Fig. 4.4.5(d), coincides with the transition from the As-rich tip to the Cd-rich, single-crystalline Cd_3As_2 main part of the nanowire. This transition region stays at a constant distance from the tip and moves with the growing nanowire upwards. The chemical composition of the tip is close to the Cd:As ratio of $CdAs_2$. Both Cd_3As_2 and $CdAs_2$ have a tetragonal space group, however, their lattice constants are rather different. Therefore, assuming that at least some of the tip crystallizes out as $CdAs_2$, the lattice mismatch will give rise to strain which could be responsible for the kink formation as it is known from III-V heterostructure nanowires.

Conclusion

Cd_3As_2 nanowires were grown in a self-catalysed process on Si substrates. Nanowires grow from the surfaces of Cd_3As_2 clusters. We propose a predominantly tip-

induced vapour-solid growth mechanism. The growth of the nanowires can be controlled through the flow of the carrier gas. Nanowires can be grown at a low flow rate, while a high gas flow leads to microwires which eventually form a thin film. We will come back to Cd_3As_2 in Chapter 7 for crystallographic and electronic characterisation.

4.4.3 SnO_2 nanotrees

To conclude the section on growth mechanisms of non-layered materials, we present a comparison between Au, TiO_2, and self-catalysed growth of SnO_2 nanostructures by vapour transport [169]. TiO_2 enables growth of a nanonetwork of SnO_2, whereas self-catalysed growth results in nanoclusters. Using Au catalyst, single-crystalline SnO_2 nanowire trees can be grown in a one-step process. Two types of trees are identified that differ in size, presence of a catalytic tip, and degree of branching. The growth mechanism of these nanotrees is based on branch-splitting and self-seeding by the catalytic tip, facilitating at least three levels of branching, namely trunk, branch, and leaf.

Background

Metal-oxide semiconductors have served as functional materials for gas sensors for decades [170]. The sensitivity, response speed, and power efficiency scale with the size of the sensing element. Nanostructures of SnO_2, which is also known for applications in solar cells, are ideal building blocks for realising improved sensors for, e.g., inflammable gases such as CO [171–174]. Branched nanowires are particularly suited to provide high sensitivity at low cost without the need of spatial resolution, i.e., it is of minor importance *where* a single gas molecule is detected on the sensor as long as it *can* be detected. The most economical method to fabricate such structures is vapour transport [175]. This method employs a catalysed growth process in which nanowires

are seeded by Au nanoparticles [176]. Branches are typically added by multi-step catalyst seeding [177].

Optimisation of the growth conditions and catalyst selection

The parameter space of SnO_2 nanowire growth was studied systematically using a fast-load lock vapour transport system and the parameters summarised in Table 4.4.2.

Table 4.4.2: Experimental parameters used to grow SnO_2 nanowires. The vapour transport setup is extended via a load-lock to allow fast sample exchange to run systematic studies without the need to cool down the furnace.

Parameter		**Value**
growth method		vapour transport with load-lock
substrate	type	Si(100)
	catalyst coating	TiO_2 P-25, Au, none
precursor		Sn
N_2 flow rate		300–900 sccm
growth temperature		800–1000°C
ramp time		1 h
growth time		1 h
substrate temperature		~480°C
analysis methods		SEM, TEM, EDS

Figure 4.4.6 shows the results of three sets of growth experiments varying the catalyst, furnace temperature, and flow rate (Fig. 4.4.6(a-c)). Three samples were prepared for the catalyst comparison shown in Fig. 4.4.6(a): without catalyst, with (20±6)-nm-diameter TiO_2 nanoparticles (rutile and anatase mixture P-25), and with (7±1)-nm-diameter Au nanoparticles.

Only plates grow from the substrate without catalyst, while both TiO_2 and Au enable nanowire growth. TiO_2-grown nanowires form an intertwined, free-standing network. Au leads to a homogeneous coverage with straight nanowires (diameter ~50 nm) and nanostars, as shown in Fig. 4.4.6(a). Therefore, we used Au nanoparticles in all subsequent SnO_2 growth experiments.

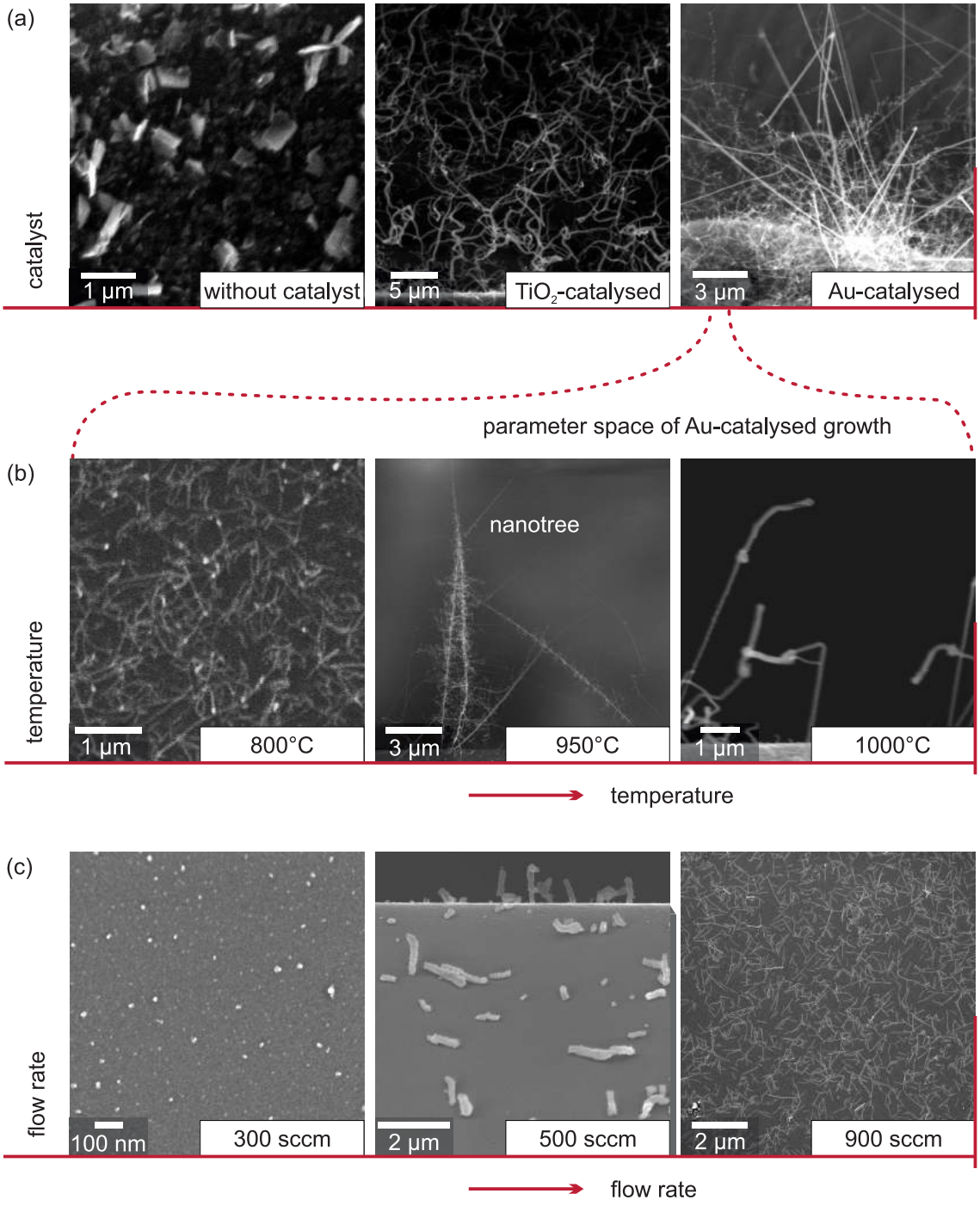

Fig. 4.4.6: SEM images of SnO_2 nanowire growth that characterise the impact of changing the growth parameters: catalyst, furnace temperature, and flow rate. Three examples are displayed in each category. (a) Substrate preparation using no catalyst, TiO_2 nanoparticles, and Au nanoparticles (left to right). Instrument: Jeol JSM-6610LV; acceleration voltage: 20 keV. (b) Furnace temperature (Au-catalysed growth) increased from 800, 950, to 1000°C. Instrument: Jeol JSM-6610LV; acceleration voltage: 20 keV. (c) Carrier gas flow rate dependence of SnO_2 nanowire growth (300, 500 (grey sideline indicates substrate edge), and 900 sccm). Instrument: FEI Quanta 600 FEG; acceleration voltage: 30 keV.

The temperature window for nanowire growth between 800°C and 1000°C is depicted in Fig. 4.4.6(b). In principle, Sn vapour transport is possible at lower temperatures since we found occasional 20-μm-sized clusters down to 600°C. The highest yield of nanowires was achieved at temperatures around 800°C. At 1000°C the nanowires have a poor morphology as determined by SEM. At around 950°C, the formation of branches from very long nanowires dominates the growth (c.f. Fig. 4.4.6(b), centre). These nanotrees lie flat on the substrate or grow free-standing from the sides of the substrate.

A flow of 700 sccm was used for the temperature series. The high flow is crucial for SnO_2 nanowire growth, as can be seen in Fig. 4.4.6(c). The catalyst particles only accumulate material and grow into spheres at too low flow but nucleation is not initiated due to limited precursor supply. There is a threshold between 300 and 500 sccm at 800°C furnace temperature where nucleation starts to occur. The large diameter of the nanowires grown at 500 sccm means that the axial growth rate is very slow and that radial growth dominates. It is the supersaturation of the catalytic tip that drives the growth at high enough flow (900 sccm). The resulting nanowires are thin and long. Many catalyst sites can be activated such that the substrate coverage, i.e., the yield, is very high.

The catalytic tips at high magnification

All nanowires that were grown using the Au catalyst have a catalytic tip larger than the 5-nm-diameter of the initial Au nanoparticle. This is an evidence of the fact that the catalyst forms an alloy with incoming precursor vapour and grows in size until supersaturation is reached, consistent with the VLS model.

TiO_2, however, is not liquid during the growth because of its higher melting point, so the VLS mechanism can be ruled out. It either forms a solid solution with SnO_2 or facilitates the formation of Sn droplets that allow for self-catalysed growth. TiO_2

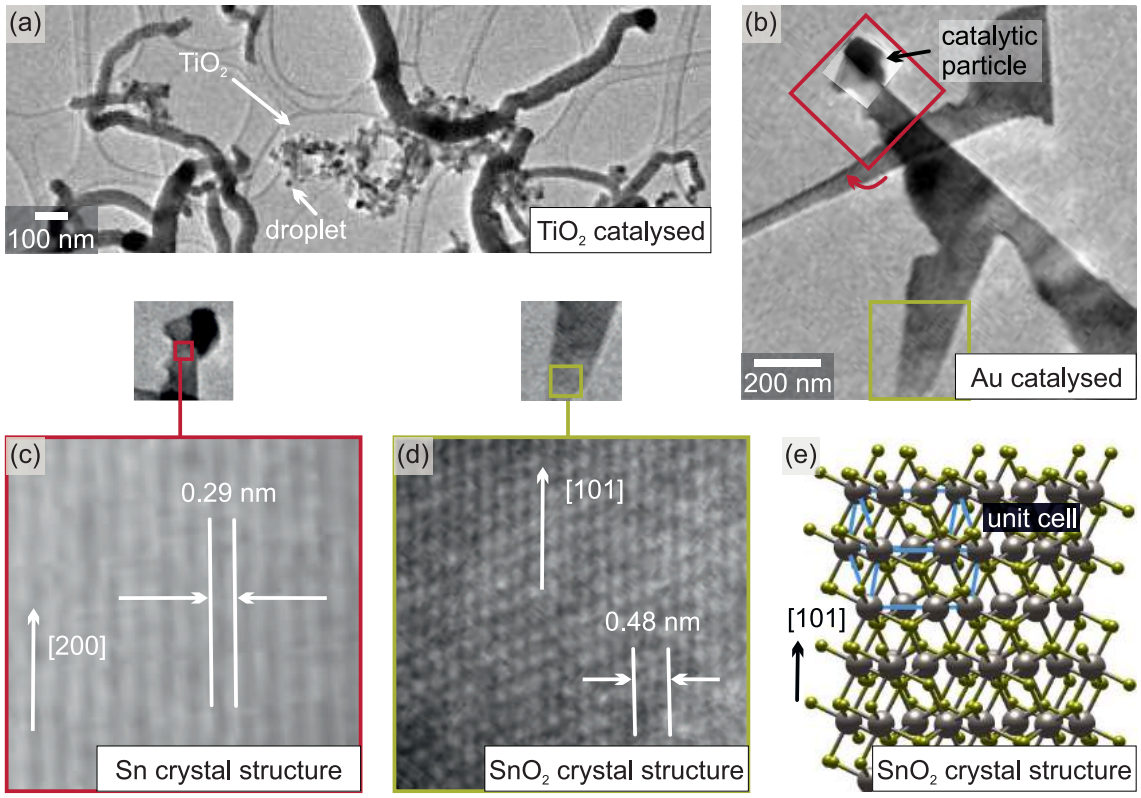

Fig. 4.4.7: TEM images of SnO_2 nanowires. (a) TiO_2-catalysed growth: The catalyst particles remain at the root of the nanowires. TiO_2 patches facilitate the formation of droplets that appear as dark spots. (b) Au nanoparticle catalyst: A catalytic particle is formed at the tip of the nanowires. Two types of crystal structures are observed: (c) β-Sn with a lattice spacing of 0.29 nm consistent with the [200] growth direction (rotated by 46° with respect to (b), red rectangle). (d) High-resolution TEM micrograph of the area highlighted by a green rectangle in (b) shows tetragonal SnO_2 with a lattice spacing of 0.48 nm. (e) A sketch of the lattice illustrates the unit cell (blue) and the [101] growth direction. Instrument: Jeol 2100 (a-d).

catalyst particles should be found at the tip if a solid solution was formed to lead to tip-catalysed growth. TEM-EDS does not detect any TiO_2 in the tip of the nanowire. Therefore, it can be concluded that the TiO_2 nanoparticles are located at the base of the wire. Growth is initiated by the formation of Sn droplets on their surface. Figure 4.4.7(a) shows such droplets as dark spots on TiO_2 patches. The nanowires are amorphous.

Au-catalysed nanowires grow longer and straight compared to TiO_2-catalysed nanowires, as shown in Fig. 4.4.7(b), and branch occasionally, as also reported by Jin *et al.* for catalyst-free growth [175]. In the centre of the catalytic tip is a dark spot which is roughly the size of a single Au nanoparticle or a cluster of several nanoparticles, indicative of VLS growth. Whereas most of the nanostructures are composed of SnO_2, a small fraction of pure Sn is also found (see high resolution image of the tip area in Fig. 4.4.7(c)). The growth direction of this short wire is the [200]-direction, consistent with Sn nanowire growth [178]. The SnO_2 nanowires have a tetragonal crystal structure and grow along the [101]-direction, as shown in Fig. 4.4.7(d,e).

The two types of SnO_2 trees

Growth at 950°C and a flow rate of 700 sccm lead to trees with and without catalytic tips. A nanowire tree without catalytic tip is tapered as shown in Fig. 4.4.8(a) and (b). It consists of three components: trunk, branches, and leaves. The components grow perpendicular to each other and become gradually smaller. Branches at the bottom are longer than branches at the top. The nanotree in Fig. 4.4.8(c) is larger and consists of a trunk with 50 nm diameter and fine branches with 30 nm diameter. The branches are curled up and have grown denser than the tree in Fig. 4.4.8(a).

The four sections of the trunk are described in the following. The tip is formed by a droplet as usually observed for VLS-grown nanowires. The next section is marked by the appearance of short branches. The number and length of branches increases

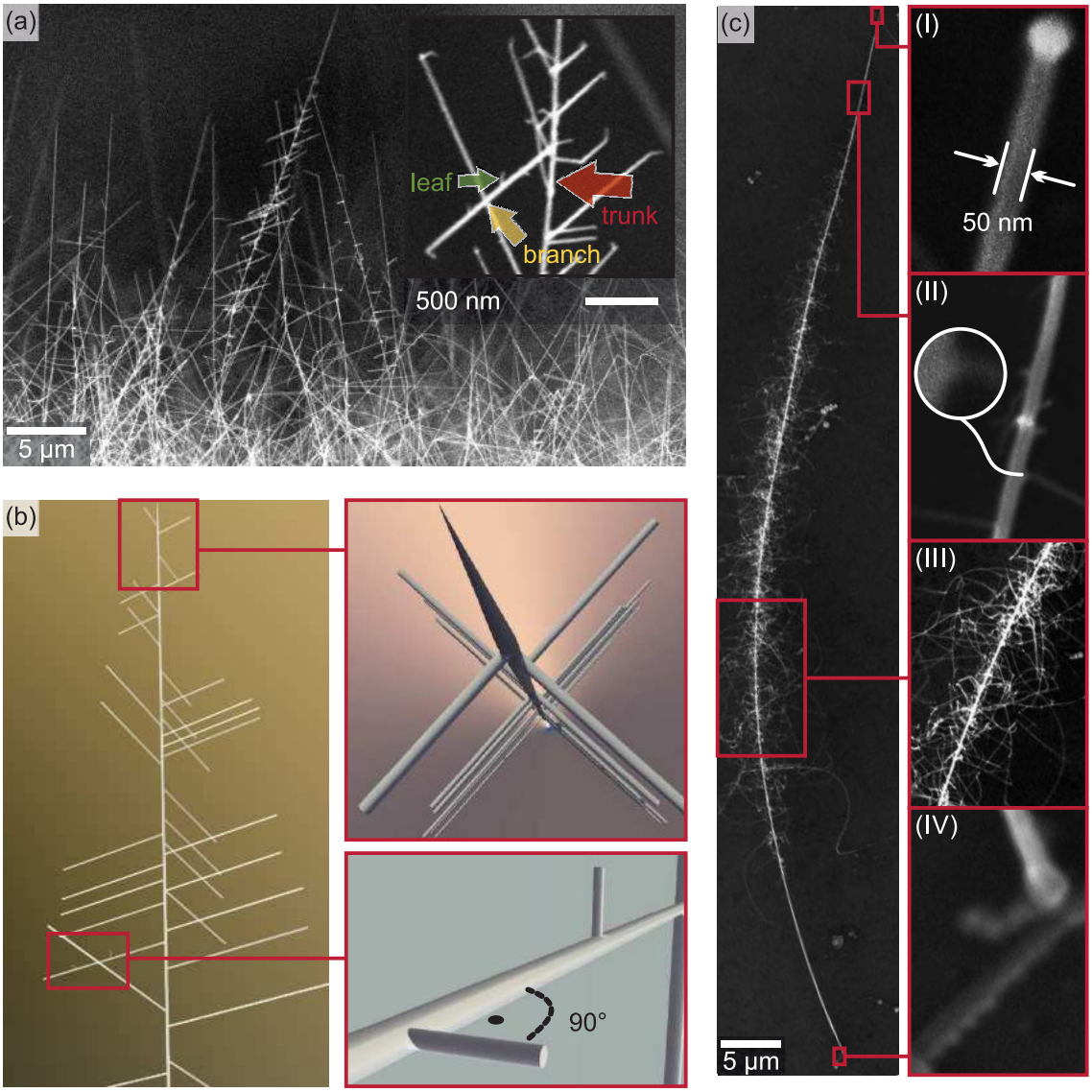

Fig. 4.4.8: SEM images of SnO_2 nanotrees. (a) Vertical trees at the substrate edge. The inset shows a trunk with branches and leaves. (b) Sketch of a nanowire tree. The tip is tapered with no catalyst particle visible at the top (upper inset). Trunk and branches as well as branches and leaves are perpendicular to each other (lower inset). (c) Horizontally oriented nanotree on the surface. There are four sections (I-IV) with distinctive features: tip (I), little branch growth with extrusion in the inset (II), middle of the trunk (III), and root (IV). Instrument: Jeol JSM-6610LV; acceleration voltage: 20 keV (a,c).

towards the main section. Branches are connected to the tree by extruding bases (Fig. 4.4.8(c) (II), inset). The fourth section near the base is completely free of branches. An amorphous structure on the root indicates the first tens of nanometers where the growth started.

Branching supported by gold nanoparticles

What is the mechanism for the formation of branches? A low magnification TEM image in Fig. 4.4.9(a) gives an overview over the density and length of the branches. The density is especially increased by splitting of branches, as can be seen in Fig. 4.4.9(b), where a nanobranch splits in the centre and separates into two branches. This can be induced by a crystal defect or, more likely, a split catalyst particle resulting in an additional growth direction. High magnification images reveal 5-nm-sized particles on the walls of the trunk, as shown in Fig. 4.4.9(c). The size is identical to the particle size of the commercial Au nanoparticles. There are three scenarios that can explain this feature. (1) Au nanoparticles migrate over the SnO_2 surface and deposit onto the trunk. The 5-nm-particle shown in Fig. 4.4.9(c) could be such a nanoparticle. However, this would require an exceptional mobility of Au on SnO_2 at this temperature. (2) Sn precursor atoms spontaneously form droplets on the SnO_2 trunk and branches grow self-catalysed following the VLS mechanism. This also explains the observa-

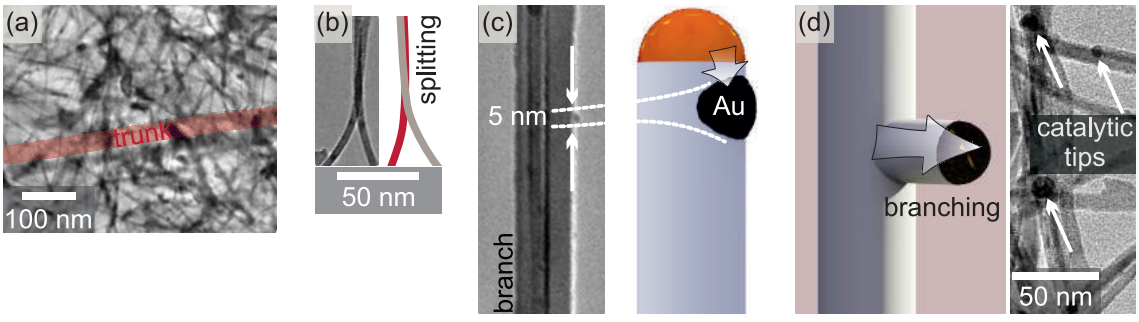

Fig. 4.4.9: Formation mechanism of SnO_2 nanotree branches. (a) TEM image of a nanotree structure. The trunk is indicated by a red line. (b) Splitting of a branch. (c) 5-nm-sized particle on the side-wall of a branch. (d) Sketch of the initial stages of the branch growth and observation of catalyst tips on branches (arrows). Instrument: Jeol 2100.

tion in Fig. 4.4.9(c) and the formation of leaves grown from smaller droplets on the branches. (3) The main catalyst particle at the tip gives off smaller particles if the size exceeds a certain threshold [179], as depicted in Fig. 4.4.9(c). These particles can even migrate several micrometers along the trunk [180]. During the first few micrometers of growth the size does not exceed the threshold yet. Hence, less branches grow near the root. Branch length is a function of height, measured from the trunk, with the longest branches towards the root and short branches, or even seeds, at the top. Leaves grow also mediated by catalyst migration on branches. Some of the nanotrees do not have a catalyst particle attached to the tip, yet still grow branches since the tip has been depleted of the catalytic particle.

Conclusion

The use of a fast-load lock in vapour transport growth has enabled systematic studies of the parameter space using Sn as a precursor. The drawback is unwanted introduction of oxygen which results in the growth of SnO_2 nanowires. Au and TiO_2 nanoparticles are efficient catalysts for SnO_2 nanowire growth. Networks of polycrystalline and bent; or single-crystalline, straight, and branched nanowires can be grown by tuning the growth parameters. TiO_2 catalyst particles facilitate the self-catalysed growth by enabling Sn droplet formation on the catalyst surface. At 950°C catalyst particles diffuse over the substrate and the grown structures. This leads to a preferential growth on nanowires forming trunks, branches, and leaves. However, the Au supported branching might come at the cost of unintentional doping or contamination by Au although we did not find any evidence of that. The nanotrees are building blocks for highly-sensitive gas detectors and other nanoelectronic devices.

5 A quasi one-dimensional topological insulator

Introduction

Bi_2Se_3 usually has a rhombohedral crystal structure (space group $R\bar{3}m$), however, an orthorhombic form occurs naturally as well and is known as Guanajuatite [181]. It has been reported in the past that the orthorhombic phase can be induced by pressure or S and Sb doping [182–184]. This is interesting in terms of TIs because of the reduced bulk conductivity by 10^{-4} Ω/cm^{-2} compared to the rhombohedral phase [185].

In contrast to the layered compounds of the $Bi_2(Se,S,Te)_3$ solid solution series, orthorhombic Bi_2Se_3 is characterised by a 1D nanoribbon structure. The polymer-like $[Bi_4Se_6]_n$ chain is linked to four neighbours per unit via weak Bi-Se and Se-Se bonds [186]. Density functional theory simulations have shown an electronic quasi 1D behaviour as van Hove singularities are found in the density of states [187]. For orthorhombic Sb_2Se_3 it is reported that the surface of the (internal) nanoribbons, which are 0.2 nm thick and 1 nm wide, is virtually perfect due to the absence of dangling bonds [188].

Bi_2Se_3 nanowires were introduced in Section 4.2.1 in the context of the growth using different catalysts. We found that the TiO_2 mixture catalyst P-25 is most suitable for the growth of high yield nanowires. Its growth mechanism is a solid-phase seeded type of growth and it includes Sb surfactant action at the tip, as described in Section 4.4.1. This chapter presents a systematic study of the growth, an analysis of the crystal structure by TEM, XRD, and Raman microscopy, and a micro-ARPES measurement on an individual nanowire.

5.1 $(Bi_{0.62}Sb_{0.38})_2Se_3$ nanowires

Vapour transport is used to grow high-density $(Bi,Sb)_2Se_3$ nanowires in a TiO_2 nanoparticle catalysed process using the parameters shown in Table 5.1.1. We use XRD and

Table 5.1.1: Experimental parameters for the growth and characterisation of $(Bi_{0.62}Sb_{0.38})_2Se_3$ nanowires.

Parameter		**Value**
growth method		vapour transport
substrate	type	Si(100)
	catalyst coating	Au, TiO_2 (P-25, anatase, rutile), Au/TiO_2
precursor		Sb-doped Bi_2Se_3
N_2 flow rate		150 sccm
growth temperature		585 °C
ramp time		1 h
growth time		1 h
substrate temperature		450 °C
analysis methods		SEM, EDS, TEM

TEM to identify the crystal structure and ARPES to confirm the existence of a topological surface state (TSS) in this material.

Figure 5.1.1 shows SEM images of the growth results as a function of substrate temperature. High purity and density $(Bi_{0.62}Sb_{0.38})_2Se_3$ nanowires, which are the main focus of this investigation, grow at a substrate temperature of 450°C, as shown in Fig. 5.1.1(c). The furnace temperature was 600°C for all growth experiments. Above a substrate temperature of 450°C, sparsely distributed larger wires with a lower Sb concentration are found, as shown in Fig. 5.1.1(a,b). For lower temperatures, less Bi is incorporated leading to the growth of Sb_2Se_3 nanowires and the appearance of Sb crystals, as shown in Fig. 5.1.1(d). The Sb concentration is measured by TEM-EDS with an error of ~1 at%. A typical EDS spectrum is shown in Fig. 5.1.2. The nanowire growth depends on the catalyst particle size, as can be seen in Fig. 5.1.1(b), where large TiO_2 flakes have not catalysed any material deposition. Below a study of the nanowires grown at 450°C is presented to determine the crystal structure and the electronic properties.

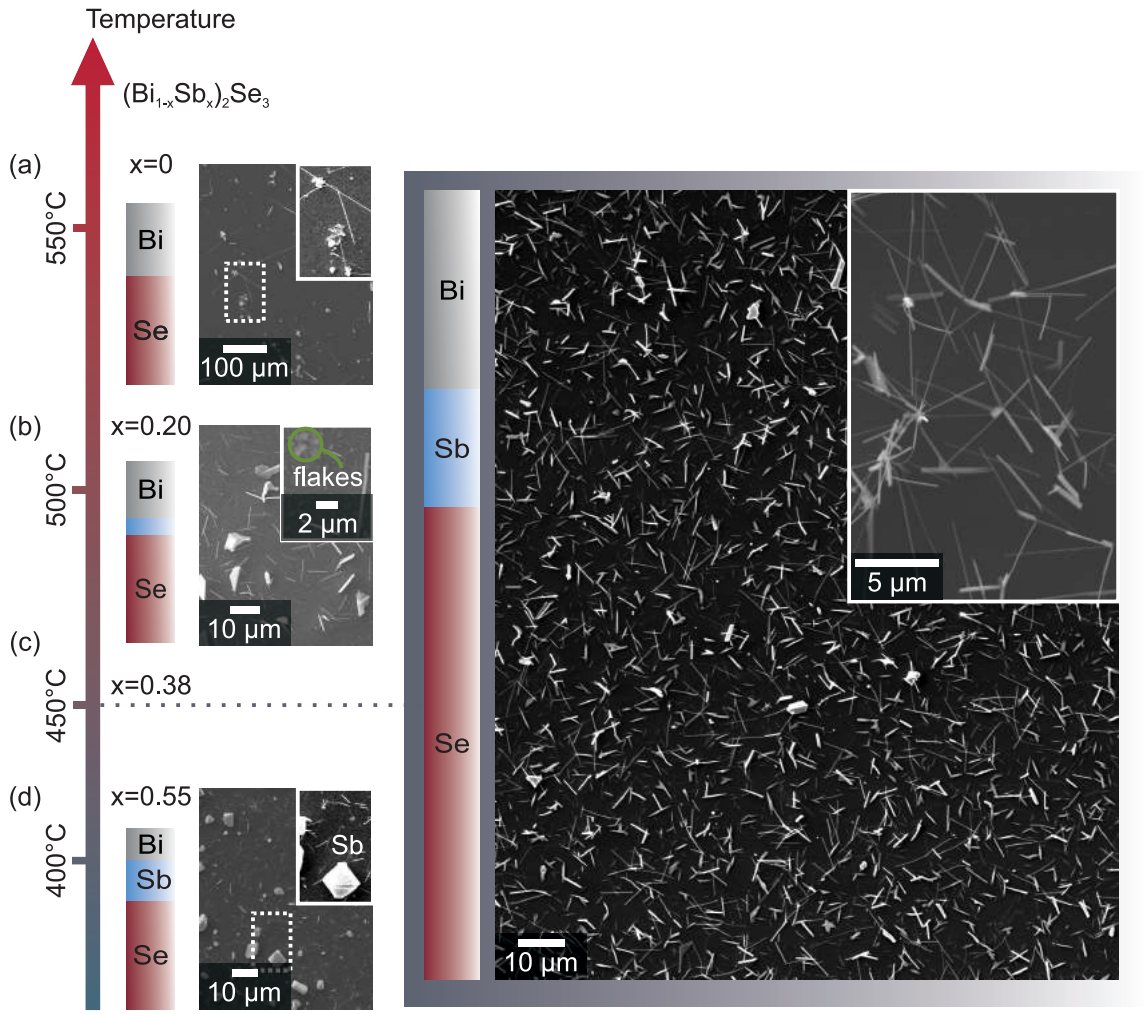

Fig. 5.1.1: Temperature-dependence of the $(Bi_{1-x}Sb_x)_2Se_3$ nanowire growth. (a) At 550°C, thick Sb-free Bi_2Se_3 wires with diameters in the range of micrometers are grown alongside other Bi_2Se_3 structures. (b) At 500°C the density of the wires is higher and Sb is incorporated. The diameter of the $(Bi_{0.80}Sb_{0.20})_2Se_3$ structures is on the order of hundreds of nm and the lengths around several μm. However, the structures are still a mixture of wires and plates. The flakes in the inset are an example of agglomerated catalyst material. (c) At 450°C, $(Bi_{0.62}Sb_{0.38})_2Se_3$ ribbons are found with a high density. Their diameter is 50-100 nm and their length a few μm. (d) At 400°C Sb dominates over Bi and the stoichiometry of the nanowires is $(Bi_{0.45}Sb_{0.55})_2Se_3$. Elemental Sb also begins to crystallise out. Instrument: Jeol JSM-6610LV; acceleration voltage: 20 keV.

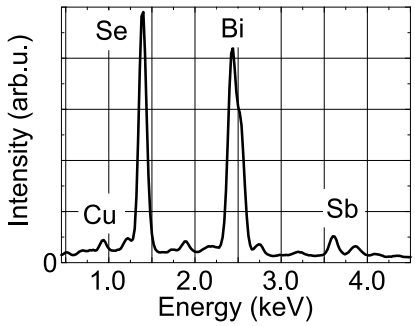

Fig. 5.1.2: EDS spectrum of the sample grown at 450°C which is in the focus of this study. The composition is $(Bi_{0.62}Sb_{0.38})_2Se_3$. The Cu peak in the spectrum is due to the Cu-grid used to support the sample. Instrument: Jeol JSM-6610LV; acceleration voltage: 20 keV.

5.2 Crystal structure

Lattice-resolved TEM images in Fig. 5.2.1(a) show that an orthorhombic phase forms upon Sb incorporation in Bi_2Se_3 nanowires. The interplanar spacings are d_{110} = 0.8 nm and d_{001} = 0.4 nm for $(Bi_{0.62}Sb_{0.38})_2Se_3$, compared to 0.828 nm and 0.398 nm, respectively, for pure Sb_2Se_3 nanowires [189].

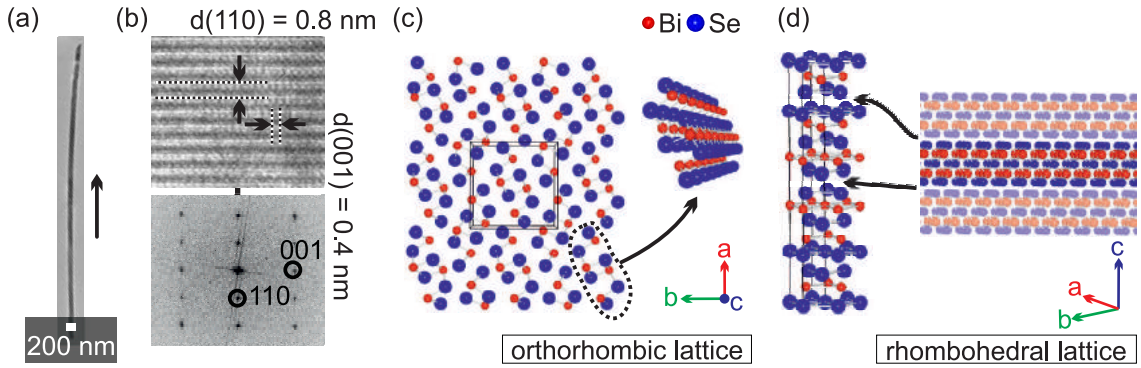

Fig. 5.2.1: (a) Low-magnification TEM image of a $(Bi_{0.62}Sb_{0.38})_2Se_3$ nanowire. The [001] growth direction is indicated by an arrow. (b) Upper/lower panel: high-resolution TEM image and corresponding Fourier transformation, respectively, show that the crystal structure is orthorhombic. Instrument: Jeol 2100. (c) Unit cell (black lines) of orthorhombic Bi_2Se_3. The characteristic 1D nanoribbon structure is shown in the inset. It is ~0.3 nm thick and 1.1 nm wide. (d) Undoped Bi_2Se_3 has a rhombohedral crystal structure and is shown for comparison with the unit cell indicated by black lines. The characteristic 2D, weakly bonding planes (van der Waals gap) are indicated by arrows. Instrument: Jeol 2100.

An ensemble of nanowires was investigated by x-ray powder diffraction at beamline I15 at Diamond Light Source (Didcot). The nanowires were transferred onto the culet of a single crystal diamond in order to minimise the substrate contribution. Similar diamonds are used in diamond anvil cell experiments since the x-ray absorption of diamond is very low and the diamond background scattering and Bragg diffraction spots are easily identified. Powder diffraction patterns were recorded using a Perkin Elmer detector and integrated using Fit2D. Topas was used to solve the crystal structure and refine the powder diffraction pattern. Measurement parameters and structural information are summarised in Tab. 5.2.1. Results of the refinement are listed in Tab. 5.2.2.

Table 5.2.1: Details on the nanowire powder diffraction experiment.

Formula sum:	$(Bi_{0.62}Sb_{0.38})_2Se_3$
Crystal system:	orthorhombic
Space group:	*Pnma*
Lattice parameters:	a = (11.78±0.01) Å, b = (4.08±0.01) Å, c = (11.56±0.01) Å
Cell volume:	(555±3) Å^3

Table 5.2.2: Fractional coordinates for all atoms in the $(Bi_{0.62}Sb_{0.38})_2Se_3$ unit cell.

Site	Wyckoff-position	x/a	y/b	z/c	occupancy
Bi1	4c	0.0193(11)	0.2500	0.33790(86)	0.6200
Sb1	4c	0.0202(31)	0.2500	0.3286(24)	0.3800
Bi2	4c	0.1594(14)	0.7500	0.04358(79)	0.6200
Sb2	4c	0.1114(36)	0.7500	0.0490(20)	0.3800
Se1	4c	0.0659(17)	0.2500	0.8757(17)	1.0000
Se2	4c	0.1387(21)	0.7500	0.4492(17)	1.0000
Se3	4c	0.2206(14)	0.2500	0.2010(18)	1.0000

The dominating phase for $(Bi_{0.62}Sb_{0.38})_2Se_3$ is the orthorhombic phase which was identified in the diffraction pattern using the Rietveld method. Small amounts of the rhombohedral phase and Si are also present in the ensemble since the nanowires were obtained by scratching from a Si substrate. The fit to the data is presented in Fig. 5.2.2. Since the Sb concentration is not high enough to form pure Sb_2Se_3 structures to such a high percentage, it can be concluded that $(Bi_{0.62}Sb_{0.38})_2Se_3$ forms an orthorhombic lattice. Bi atoms occupy Sb sites in the orthorhombic Sb_2Se_3-type lattice as will become apparent from the Raman spectrum.

The Raman spectrum of a single $(Bi_{0.62}Sb_{0.38})_2Se_3$ nanowire in Fig. 5.2.3 resembles qualitatively the spectrum of Sb_2Se_3 [190]. All vibrational modes that involve Sb atomic sites are shifted to lower frequencies ν, since the atomic mass m of Bi (Z = 83) is higher than that of Sb (Z = 51) and $\nu \sim m^{-1}$. Therefore, the spectrum can be explained by substitution of Bi by Sb atoms in the orthorhombic lattice. For comparison, the Bi-Se peak of pure Bi_2Se_3 is located at 131 cm^{-1} and the Sb-Se peak of Sb_2Se_3 at ~190 cm^{-1} according to Ivanova *et al.* [190]. No peak was observed above 180 cm^{-1}, thereby ruling out the existence of Sb_2Se_3 in the sample.

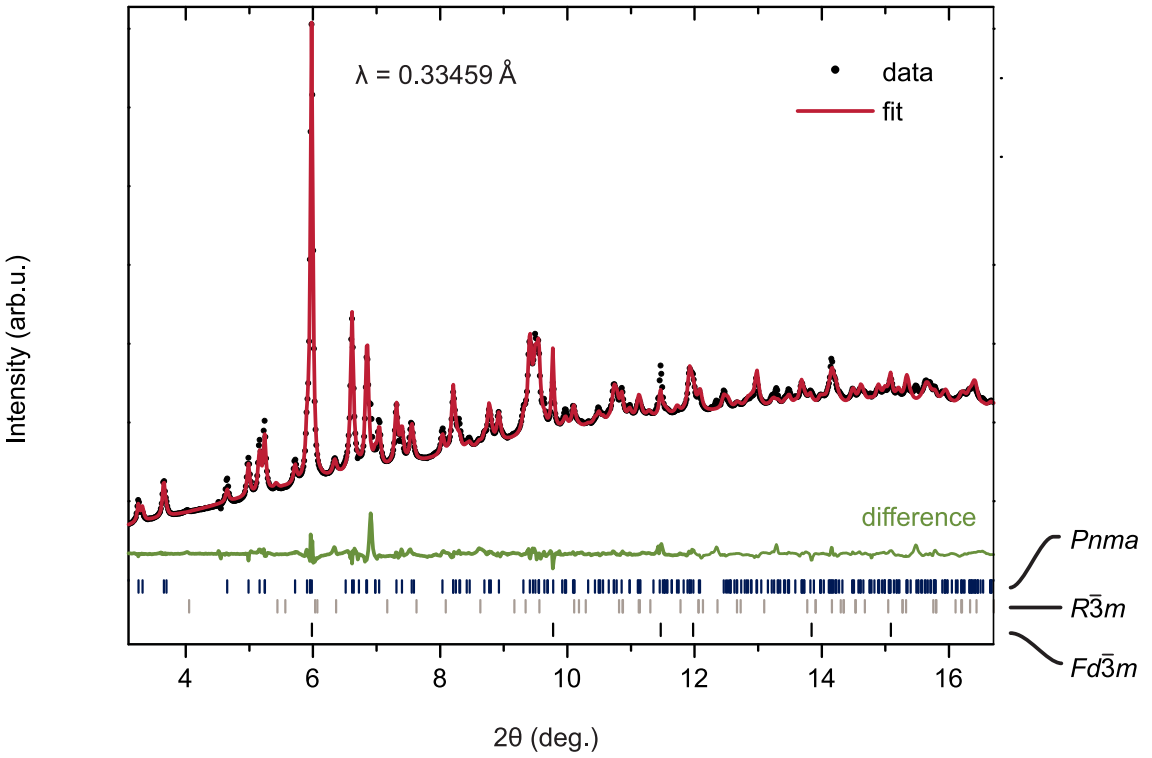

Fig. 5.2.2: X-ray diffraction pattern of an ensemble of $(Bi_{0.62}Sb_{0.38})_2Se_3$ nanowires taken at beamline I15, Diamond Light Source, Didcot, UK. The x-ray diffraction data (black dots) is the integrated x-ray intensity of the powder diffraction pattern. It is fitted by the dotted line using the Rietveld method with the software package Topas. The best fit (red line) is obtained for the orthorhombic phase and a small amount of rhombohedral material and Si (from the substrate). The green line shows the difference between the data and the fit. Expected peaks for the space group of the orthorhombic unit cell (*Pnma*, blue) and the rhombohedral unit cell ($R\bar{3}m$, grey) for Bi_2Se_3 are indicated at the bottom. Peaks for Si ($Fd\bar{3}m$, black) are also indicated.

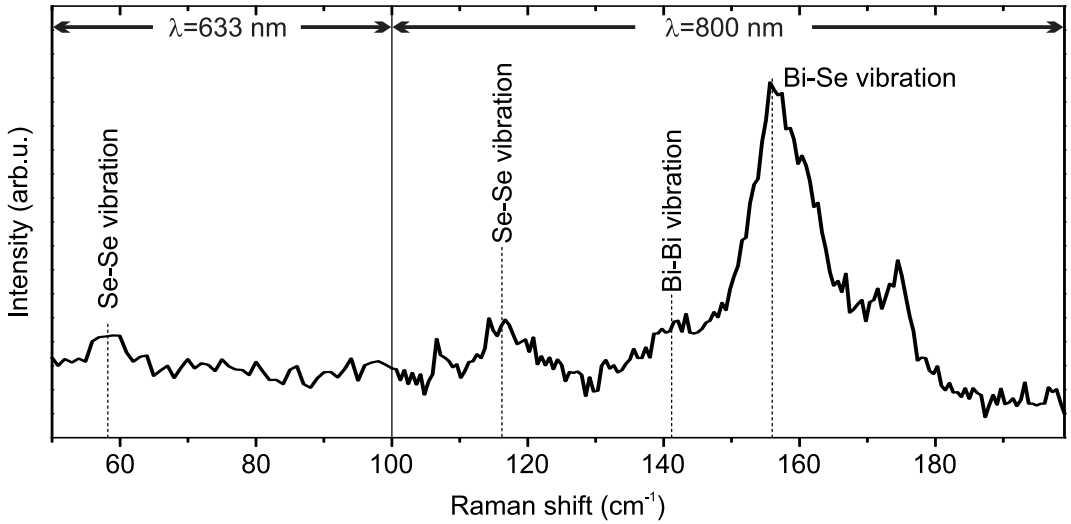

Fig. 5.2.3: The Raman spectrum of a single $(Bi_{0.62}Sb_{0.38})_2Se_3$ nanowire was recorded with a laser wavelength of λ = 633 nm at 2.5 mW/μm^2 on the low frequency side and λ = 800 nm at 15.3 mW/μm^2 on the high frequency side using the Horiba T64000 Raman spectrometer system. The main peak at 156 cm^{-1} comes from a Bi-Se bond vibration. For pure Sb_2Se_3 the Sb-Se vibration is located at 190 cm^{-1}. Thus, Sb doping broadens the peak towards higher frequencies. At 174 cm^{-1} the A^2_{1g} mode of Bi_2Se_3 appears. It is broadened towards lower frequencies by the Sb dopant. Other Bi_2Se_3 modes are silent. The Bi-Bi bond vibration appears as a smaller peak at 141 cm^{-1}. The two peaks at 58 and 116 cm^{-1} are Se-Se vibrational modes.

Our structural analysis shows that Sb-doped Bi_2Se_3 has an orthorhombic crystal structure in which Sb substitutes on Bi sites. It is characterised by quasi 1D bands, both structurally and electronically, much different from the layered structure known from pure Bi_2Se_3. The fundamental question is whether or not it is a topological insulator, keeping in mind that orthorhombic Sb_2Se_3 is not a TI.

The ARPES measurement of the band dispersions along the K-Γ-K direction is shown in Fig. 5.2.4, which looks similar to those of Bi_2Se_3 [191]. The V-shaped dispersion is from the surface state band, and its apex indicates the Dirac point. The bandgap of the sample from the experiment is ≥200 meV, and the Fermi level E_F of the sample resides at the very bottom of the bulk conduction band, indicating a very low doping level. A dip in the bulk valence band indicates the band inversion. This confirms that orthorhombic $(Bi,Sb)_2Se_3$ is a TI.

The measurement was conducted at the spectromicroscopy beamline at Elettra Synchrotron Radiation lab in Italy. The surface of the sample was cleaned by several cy-

cles of Ar-sputtering and annealing under vacuum. Measurements were taken using a beam energy of 100 eV with energy resolution of 70 meV and angle resolution 0.5°. The beam was focused into a sub-micron spot size and individual nanowires were identified by scanning the beam over the surface.

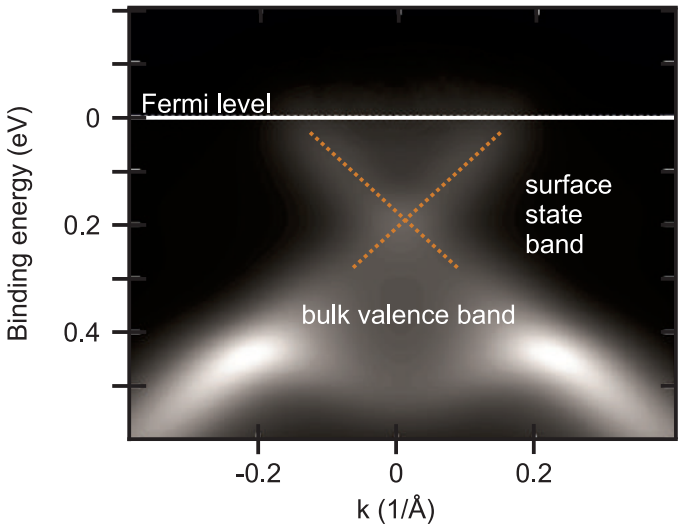

Fig. 5.2.4: Electronic bandstructure of a $(Bi_{0.62}Sb_{0.38})_2Se_3$ nanowire. The micro-ARPES spectrum along the K-Γ-K direction was taken on an individual nanowire at the spectromicroscopy beamline at Elettra Synchrotron Radiation lab in Italy using a low photon energy beam. The energy is measured with respect to the Fermi level. The broad bulk valence band is indicated and a bulk bandgap of ≥200 meV is visible. The surface state band (SSB) has a distinct V-shape and the crossover point is the Dirac point.

Conclusion

The incorporation of Sb into Bi_2Se_3 leads to an orthorhombic crystal structure (space group *Pnma*). Sb enters the crystalline matrix by replacing Bi, as concluded from the shift of the vibrational modes in the Raman spectrum. The amount of Sb doping can be controlled via the substrate temperature during growth. Instead of Au, we employed TiO_2 nanoparticles as a catalyst. We explored the entire temperature range in which doping was possible, starting from Sb-free, binary Bi_2Se_3 at 550°C down to the lowest temperature (400°C) at which Sb starts to crystallise out. The Sb doping concentration (in % of the Bi sites) ranges from 0 to 55. The study focused on the 38% Sb-doped sample. The nanowires are pure, dense, and uniform, which allowed to

study ensembles by x-ray powder diffraction which confirms the orthorhombic crystal structure of the nanowires. Previous work found a maximum doping concentration of 10% and the formation of a Sb_2Se_3 guest lattice [49, 50], which was absent in this study in both the TEM and XRD data. In micro-ARPES measurements on an individual nanowire we found a TSS. The bulk bandgap is ≥200 meV. The Fermi level resides above the Dirac point and no further surface doping was required to make the TSS visible.

The interesting question is why Sb-doped Bi_2Se_3 with its peculiar quasi 1D sheet structure is a TI, while the end member of the doping series, orthorhombic Sb_2Se_3, is not. A possible reason could be the strain resulting from Sb doping. Starting from the topologically trivial, orthorhombic Sb_2Se_3 structure, the insertion of Bi^{3+} (ionic radius 117 pm, as compared to 90 pm for Sb^{3+}) will lead to an expansion of the lattice, similar to the application of external pressure [192, 193]. Density functional theory calculations would add to an understanding of the occurrence of the TSS in 1D structures, which are very much different from the layered structure of the vast majority of all experimentally confirmed TIs [62].

6 Bi_2Te_3: growth optimisation and hybrid structures

Introduction

This chapters will explore the nanowire growth of the TI Bi_2Te_3 with the ultimate goal to achieve heterostructure growth. First, a recipe for the growth of small Bi_2Te_3 nanowires with Se as additional precursor is developed and a method introduced that can be used to quickly determine the stoichiometry by Raman spectroscopy. Then, Bi_2Te_3 nanostructures are grown as large as possible using vapour transport and the existence of a TSS is demonstrated by electronic transport measurements. The third part shows a potential route to realise Majorana fermions in superconductor/TI hybrid nanomaterials of Sn and Bi_2Te_3. Sn is also known to reduce the intrinsic doping in Bi_2Te_3.

6.1 Ternary compounds

Bi_2Te_2Se (BTS) and Bi_2Se_2Te (BST) are combinations of the binary TIs Bi_2Se_3 and Bi_2Te_3 with a tetradymite structure. The advantage of these ternary materials is that defect-induced bulk carriers are suppressed by reduction of the intrinsic defects such as vacancies and anti-site defects compared to their binary counterparts [54, 194]. Hence their bulk resistivity is higher which is desirable for TSS measurements [55, 195]. A detailed study of Bi_2Te_2Se nanowire growth as a function of substrate temperature is presented using the parameters summarised in Table 6.1.1.

6.1.1 Growth

The morphology and composition of the synthesised nanostructures strongly depend on the substrate temperature. SEM micrographs of samples grown at substrate temperatures of 480°C, 506°C, and 545°C are shown in Fig. 6.1.1. At the highest temperature (see Fig. 6.1.1(c)) mostly small objects were found; in part sheets growing out of

Table 6.1.1: Experimental parameters for the growth of Bi_2Te_2Se nanowires with a high yield.

Parameter		**Value**
growth method		vapour transport
substrate	type	Si(100)
	catalyst coating	Au
precursor		Bi_2Te_2Se
N_2 flow rate		150 sccm
growth temperature		585°C
ramp time		1 h
growth time		1 h
substrate temperature		150-550°C
analysis methods		SEM, TEM, AFM
		XRD (I15), Raman (Horiba)

the surface, along with sparsely distributed larger wires. The composition is Bi_2Se_3 as determined by EDS, indicating that the temperature is too high for the incorporation of Te. At 506°C the planar growth increases and only a few, smaller nanowires are found as shown in Fig. 6.1.1(b). The x-ray powder diffraction pattern in Fig. 6.1.2 was obtained from the as-grown material by scraping. It shows that the material is Bi_2Te_2Se with space group $R\bar{3}m$ and the lattice parameters are $a = 4.25$ Å and $c = 29.95$ Å [196]. The peak associated with [110]-oriented crystals is enhanced, suggesting a pre-

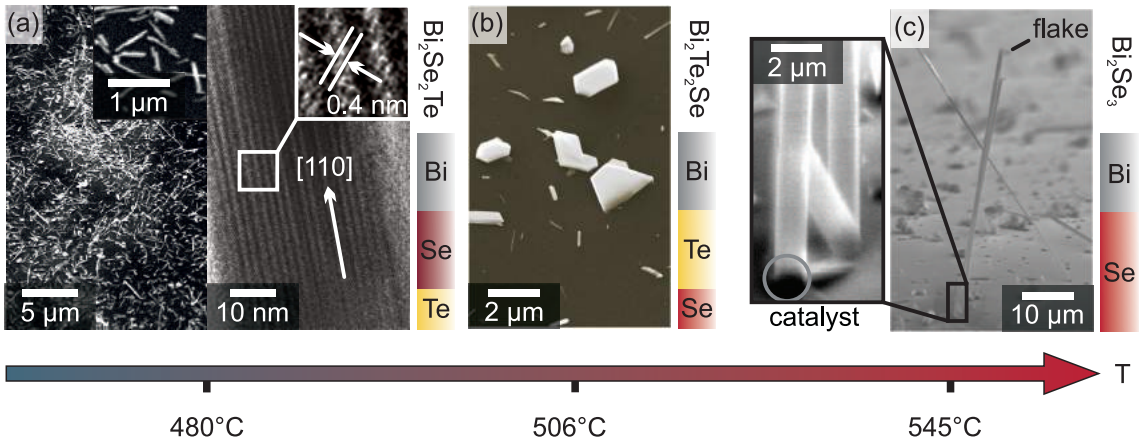

Fig. 6.1.1: Electron micrographs of samples grown between 480°C and 545°C: (a) 480°C (left: 45° tilt-view SEM, right: TEM, Jeol 2100), (b) 506°C (top-view SEM), and (c) 545°C (side-view SEM). In the lattice-resolved TEM micrograph in (a), the indicated growth direction is along [110]. The inset reveals an interplanar distance of 0.4 nm. In (b) mostly Bi_2Te_2Se platelets are observed, whereas at higher temperatures (c) the sample is composed of flakes as well as large Bi_2Se_3 wires. Instrument: Jeol JSM-6610LV; acceleration voltage: 20 keV.

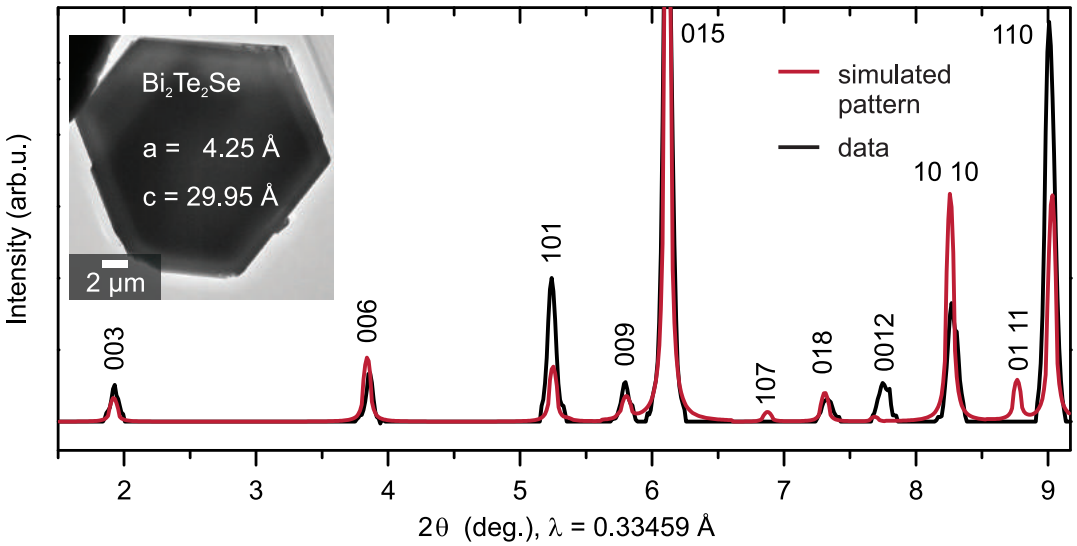

Fig. 6.1.2: X-ray powder diffraction pattern of the nanostructure sample grown at 506°C (black line). The pattern is assigned to Bi_2Te_2Se. The red trace is the simulated pattern [196]. The inset shows a TEM micrograph of a hexagonal platelet recorded using the Jeol 2100, which is typical for the studied powder sample. Data was taken at Beamline I15, Diamond Light Source, Didcot, UK.

ferred orientation within the sample. For two peaks, (107) and (01 11), the intensity is too low to be resolved.

At a substrate temperature of 480°C the surface is uniformly covered with nanowires, indicating that the axial growth dominates over the planar and radial growth modes as can be seen in Fig. 6.1.1(a). Lattice-resolved TEM imaging shows a spacing of 0.4 nm between adjacent lattice planes, consistent with a growth direction along [110]. This confirms the observation of a preferred growth orientation in the x-ray data. TEM-based EDS analysis identifies the composition as Bi_2Se_2Te.

At even lower temperatures, i.e., below the optimum Bi_2Se_2Te growth temperature (results not shown), axial and radial nanowire growth still dominates. However, no Bi is detectable in these nanowires since its vapour pressure is orders of magnitude lower than that of Se and Te at these temperatures.

6.1.2 Composition analysis using Raman spectroscopy

The composition of the nanostructures is further analysed using micro Raman spectroscopy, which allows for a study of individual nanowires. The spectrum of a nanowire grown at 480°C is shown in Fig. 6.1.3(a) and exhibits four peaks that were assigned to the three modes of Bi_2Se_2Te – note that the E_g^2 mode is split for certain stoichiometries. The fit was obtained using the software tool *peak-o-mat* [197]. It is based on the assumption of the existence of four Lorentzian line shape peaks and a linear background. The software takes user generated starting parameters of the slope of the background and the position and width of the peaks via a graphical user interface. Exact values are then determined via a least squares refinement in fifty steps.

The Raman spectrum of $Bi_2(Te_{1-x}Se_x)_3$ strongly depends on the compositional value x, as determined by Richter *et al.* (data reproduced in Fig. 6.1.3(b)) [198]. The spectrum is dominated by the A_{1g}^2 and E_g^2 modes over a broad range of intermediate x values due to the decoupling of the Bi-Te and Bi-Se vibrations at high frequencies. The A_{1g}^2 mode especially is subject to change for high Se concentrations. This fact makes this mode a sensitive indicator of variations in the concentration x. The high frequency E_g^2 mode is broadened as in the original data of Richter *et al.* (see their Fig. 5(a)). The position of the A_{1g}^2 and higher E_g^2 mode were weighted stronger than the position of the relatively constant A_{1g}^1 mode and the lower E_g^2 mode. The value of x was determined to 0.7, once more confirming the stoichiometry to be Bi_2Se_2Te.

6.2 Millimetre-long Bi_2Te_3 nanowires

There is a profound interest in long Bi_2Te_3 nanowires for three reasons: (i) They enable the observation of pronounced Shubnikov-de Haas oscillations as seen in long Bi_2Se_3 nanowires [199]; (ii) they offer the possibility to combine multiple devices on a single

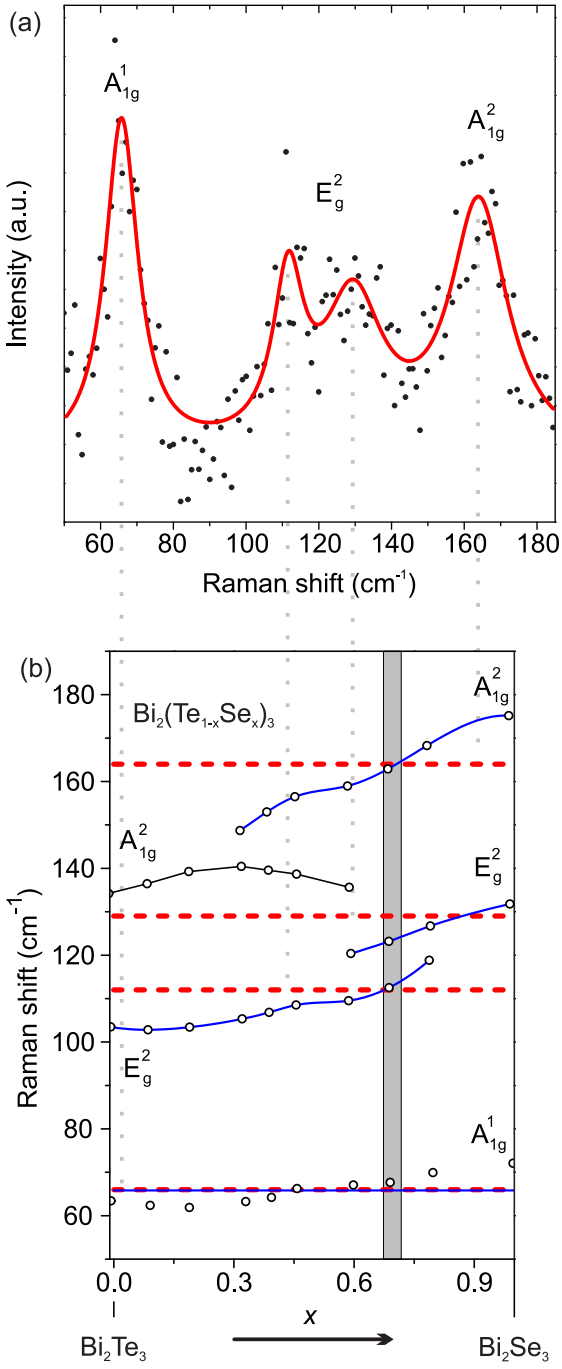

Fig. 6.1.3: (a) Raman spectrum of a nanowire grown at 480°C recorded using the Horiba T64000 Raman spectrometer system at 3 mW incident laser power and a laser wavelength of 633 nm. Four peaks at (65.7±0.4), (111.6±0.8), (130±2), and (164.0±0.7) cm^{-1} are obtained from fitting Lorentzians to the data. The peaks can be assigned to the Raman modes of Bi_2Se_2Te. (b) Representation of the Raman data for $Bi_2(Te_{1-x}Se_x)_3$ for $0 < x < 1$ taken from Ref. [198]. Data points of the higher A^2_{1g} and the E^2_g mode were fitted with a spline interpolation. Red dashed lines indicate the peak positions of the nanowire and the shaded grey area the composition range of $x \approx 0.69 \pm 0.02$.

nanowire [200]; (iii) long nanowires are an interesting building block for sensors that require few high-aspect electrodes over a wide area without the need of high spatial resolution [201, 202].

Previous electrical measurements on VLS-grown Bi_2Te_3 nanowires were limited to quasi-four-point-probe measurements due to the short length of the nanowires [111]. The influence of contact resistance could not be fully excluded. Andzane *et al.* demonstrated four-point-probe measurements on Bi_2Te_3 nanobelts that were synthesised in a two-step process [203]. We have grown free-standing millimetre-long Bi_2Te_3 submicron belts by vapour transport in a one-step process. The new TiO_2 catalyst increases the growth yield compared to catalyst-free growth. Four separated contacts are prepared by standard laser lithography to extract the temperature-dependent conductivity. The vapour transport growth was carried out using the parameters summarised in Table 6.2.1.

Table 6.2.1: Experimental parameters for the growth of long belts of Bi_2Te_3.

Parameter		**Value**
growth method		vapour transport
substrate	type	Si(100)
	catalyst coating	TiO_2 and none
precursor		Bi_2Te_3
N_2 flow rate		300 sccm
growth temperature		585 °C
ramp time		1 h
growth time		1 h
substrate temperature		450 °C
analysis methods		SEM, SEM EDS, AFM, electronic transport

6.2.1 Catalytic activity

Exact reproducibility of vapour transport growth experiments is a great challenge. One reason is the memory effect, i.e., that growth experiments are affected by de-

posits on the walls of the quartz tube from previous runs, and small variations in the growth parameters, such as temperature, resulting from slightly varied substrate arrangements. The catalyst-loaded and pristine substrates were overgrown simultaneously and in close proximity to one another to minimise these problems. Eight substrates were prepared for each growth run, out of which four were coated with TiO_2 nanoparticles. The substrates were placed in the quartz boats before transfer into the furnace, as shown in Fig. 6.2.1(a). The Roman numerals from (I) to (IV) indicate pairs of substrates, whereby (I) corresponds to the hotter zone (close to the centre of the furnace) and (IV) to the colder downstream end. A ceramic insert supports the substrates as depicted in Fig. 6.2.1(b) so that their position is right in the vertical centre of the quartz tube in order to optimize the exposure to the vapour. Substrates next to each other are subject to the exactly same growth conditions, i.e., substrate temperature and precursor flux.

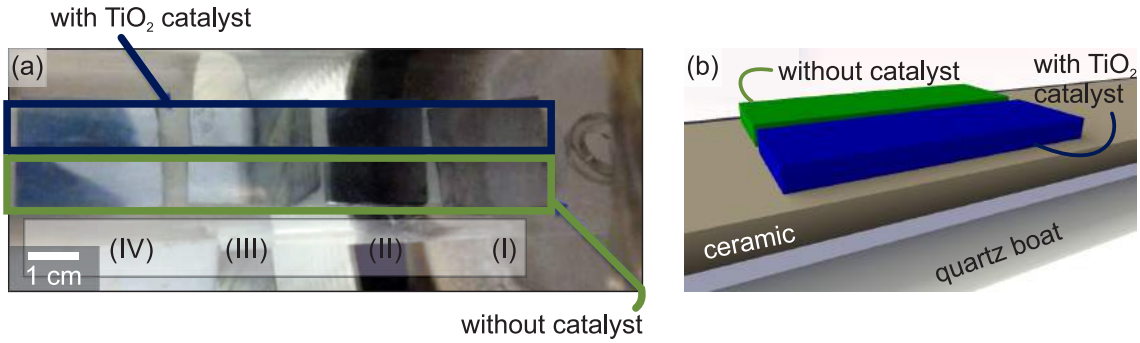

Fig. 6.2.1: (a) Image of eight Si(100) substrates placed onto the ceramic insert in the quartz boat. The metal housing and the white isolation material of the furnace can be seen on the right-hand side. The blue frame indicates the four substrates coated with TiO_2 catalyst nanoparticles, and the green frame indicates four pristine substrates without catalyst. (b) Sketch of the substrate arrangement. Two substrates with (blue) and without catalyst (green) are placed next to each other. The ceramic insert assures the position of the substrates remains unchanged.

After growth all eight substrates are coated with a grey or silver-coloured layer judging from the optical inspection; samples with and without catalyst look the same. EDS analysis confirms the stoichiometry to be Bi_2Te_3 (see below for more details). SEM images, however, reveal the impact of TiO_2 on the growth. Samples grown next to each other are compared in Fig. 6.2.2 using the numbering scheme introduced in

Fig. 6.2.1(a). The grey coating layer observed for samples in zone (I) is a result of the growth of platelets which can be seen for both samples grown at the same temperature in Fig. 6.2.2(a) and (b), for TiO_2 and without catalyst, respectively. The catalyst facilitates the growth of a higher density of platelets and smaller platelet dimensions. Platelets grown without catalyst are larger with dimensions typically between 10 and 20 µm. Sub-micron belts are only rarely observed, but a few were spotted as shown in the inset in Fig. 6.2.2(b). TiO_2 increases the areal density of belts drastically, as can be already seen in the overview in Fig. 6.2.2(a). An ensemble of several belts is shown in the inset in Fig. 6.2.2(a).

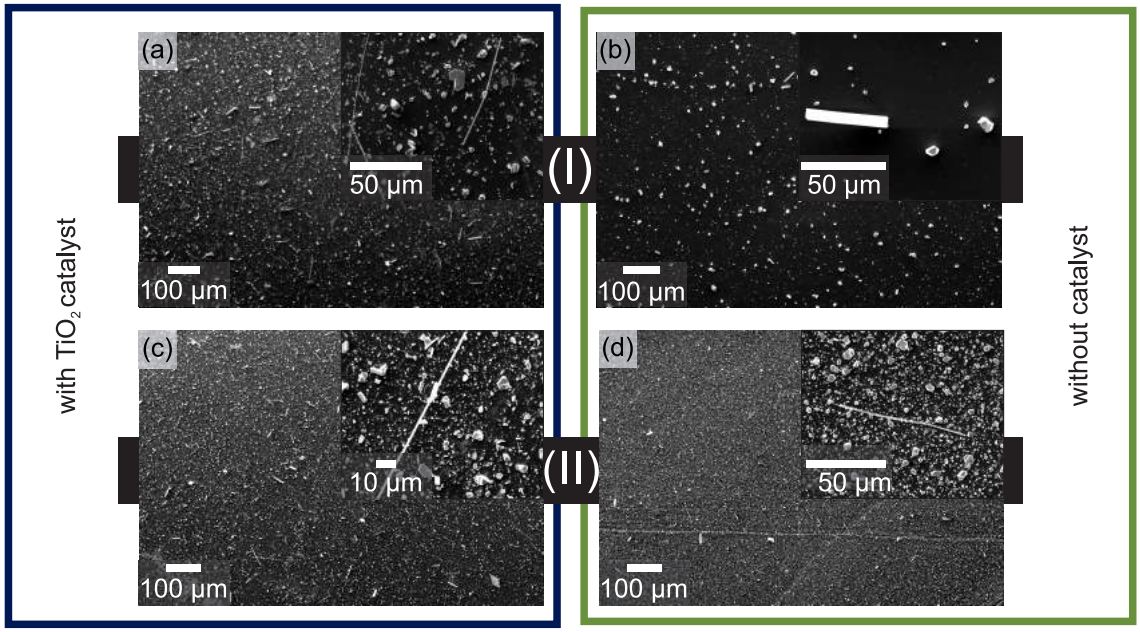

Fig. 6.2.2: SEM images of Bi_2Te_3 nanostructures from sample pairs from zones (I) and (II) with TiO_2 catalyst nanoparticles (blue frame) and without catalyst (green frame). (a) Zone (I), TiO_2: Platelets and belts grow with relatively high yield. Most platelets grow at an angle to the substrate normal. (b) Zone (I), catalyst-free: Only very few belts and almost no small platelets are grown. The most abundant structures are 10 µm-diameter platelets. (c) Zone (II), TiO_2: Dense growth with significantly increased density of belts. (d) Zone (II), catalyst-free: The density of platelets increases compared to (c). Some thin nanowires are observed. Instrument: Jeol JSM-6610LV; acceleration voltage: 10 keV.

For lower substrate temperatures, downstream in zone (II), the stoichiometry is Bi_2Te_3 as well. The platelet density increases for both samples although the size of the platelets decreases (see Fig. 6.2.2(c) and (d)). A larger number of belts is found, effectively catalysed by the TiO_2 nanoparticles (Fig. 6.2.2(c)). The inset shows that the hexagonal

platelets are not only lying flat on the surface but also extend from the surface under an angle. Few electron-transparent, i.e., very thin, belts are observed on the corresponding catalyst-free substrate (Fig. 6.2.2(d)). The platelets grow horizontally, as in case of the thin film growth (see Fig. 6.2.2(d), inset). Their shapes reflect the inherent hexagonal crystal structure. This indicates that the growth at an angle to the substrate is characteristic of the catalysed process. The samples grown at a lower temperature in zone (III) (not shown) are very similar to the ones grown in zones (I) and (II) in that a mixed growth of platelets and belts is observed. In contrast, the two substrates grown in zone (IV) are covered with a layer of Te and no Bi_2Te_3 is found. To summarise, the substrate temperature window for the growth of Bi_2Te_3 sub-micron belts, using a furnace temperature of 600°C, is between 450–510°C, with close to optimum conditions for 480°C.

6.2.2 Growth time

In the next step, the dependence of belt dimensions on the growth time was studied, employing nanoparticle TiO_2 catalyst. A growth time of 1 h was used for the catalyst comparison discussed above. The analysis of Fig. 6.2.2(c) yields an average length of belts of (53±19) µm. The distribution of dimensions across the ensemble is very heterogeneous, indicative of a random start time of the belt growth within the 1 h of growth. In Fig. 6.2.3(a) an overview and a high magnification image of a similar sample grown for 4 h are shown. The average length is (107±28) µm, which is twice the average length for the 1-h-sample. Larger and fewer platelets are found in Fig. 6.2.3(a).

For the 8-h-sample, however, the number of small platelets increases (see Fig. 6.2.3(b), high magnification image) consistent with both previous samples grown at shorter growth times. The average length was estimated to (111±50) µm using the overview in Fig. 6.2.3(b). This number is identical to the 4 h growth, however, the standard devia-

tion has doubled. The reason for the increase in standard deviation instead of average length is twofold. Some belts have grown for the entire duration to become extremely long, while short ones have just started to grow when the growth period finished. Furthermore, the average width (neglecting rotation with respect to the viewing direction) has increased from (2.0±0.9) µm to (3.4±1.2) µm indicating horizontal growth where the material is deposited onto the sidewalls. So far, it is not clear what determines whether the vertical (on top of the layers) or horizontal growth dominates.

Typically, over a substrate area of 1×1 cm^2, one to two very long structures can be found, as shown in Fig. 6.2.4(a). The free-standing structure has a length of at least 0.8 mm, a width of 4 µm, and a thickness of 430 nm. It stands without bending at a

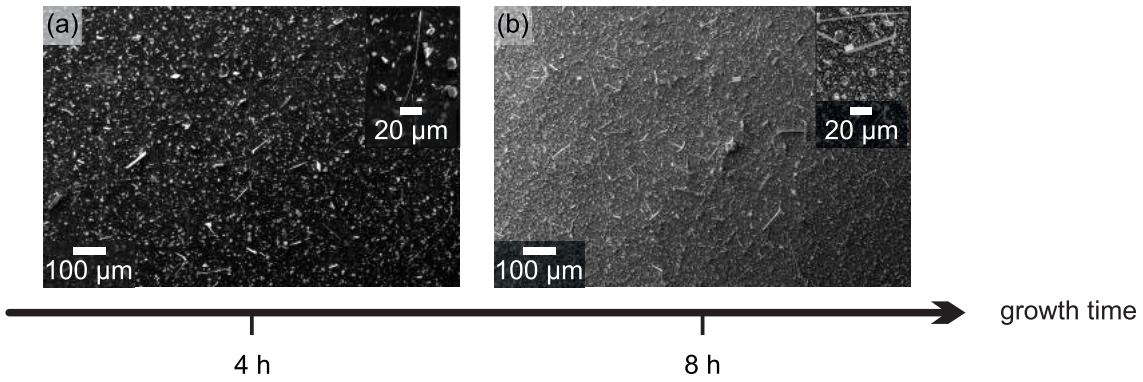

Fig. 6.2.3: SEM images of two samples grown for (a) 4 h and (b) 8 h. The number of small platelets and the width of Bi_2Te_3 belts increases with growth time, however, the average length does not change significantly. Instrument: Jeol JSM-6610LV; acceleration voltage: 20 keV.

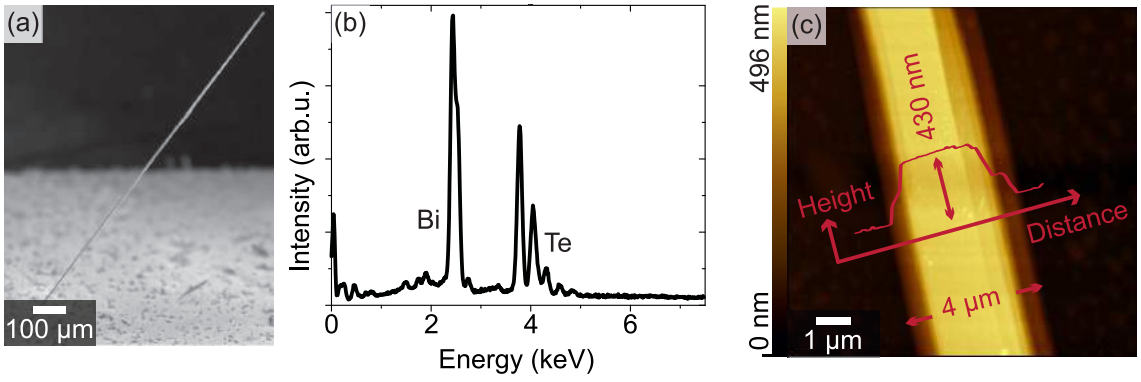

Fig. 6.2.4: (a) SEM image of a free-standing Bi_2Te_3 belt. Instrument: Jeol JSM-6610LV; acceleration voltage: 20 keV. (b) EDS analysis shows the composition to be stoichiometric Bi_2Te_3. (c) AFM image of the long Bi_2Te_3 belt, with the height profile in red, showing a thickness of 430 nm and a width of 4 µm, i.e., an aspect ratio of thickness to width of ~1:10.

height-to-width ratio of only ~1:10 and a height-to-length ratio of ~1:2,000. Assuming a constant growth scenario over the 8 h of growth, the growth rate was larger than 28 nm/min. The composition was determined to be stoichiometric Bi_2Te_3 using EDS, as shown in Fig. 6.2.4(b). Subsequent to the growth, the belt was transferred by hand using a micro-needle, and deposited onto a Si wafer to study its height profile using AFM (see Fig. 6.2.4(c)). The observation of step edges is an indicator of a growth direction parallel to the quintuple layers.

6.2.3 Electronic transport

Two belts, labelled B1 and B2, were picked from the same substrate for four-point-probe measurements. A typical device is shown in the inset of Fig. 6.2.5. The distance l between the voltage probes is $l_{B1} = 31.4\,\mu m$ and $l_{B2} = 52.5\,\mu m$ for B1 and B2, respectively. The resistance R was studied as a function of temperature T. The electrical conductivity $\sigma(T)$ of each belt was calculated using

$$\sigma(T) = \frac{1}{R(T)} \frac{l_B}{A_B}, \tag{6.2.1}$$

with A the belt's rectangular cross-section given by $A_B = h_B \times w_B$ (see Fig. 6.2.4(c) for qualitative comparison). The room temperature values for σ and the dimensions of B1 and B2 are given in Tab. 6.2.2. B1 has a conductivity of $\sim 0.5 \times 10^5\,S\,m^{-1}$, comparable to the low value reported for n-type bulk Bi_2Te_3 [204]. The electrical conductivity of the two belts differs by nearly one order of magnitude.

Stoichiometry variations beyond +1% Te in Bi_2Te_3, as determined by EDS on several belts, can be excluded as the cause of this difference.

Further, deviations in electrical conductivity can originate from defects or Te-depletion near the surface that leads to a surface layer of high electrical conductivity [205]. In our case, the surface-to-volume-ratio of B2 is about 20 % higher than that of B1 so that

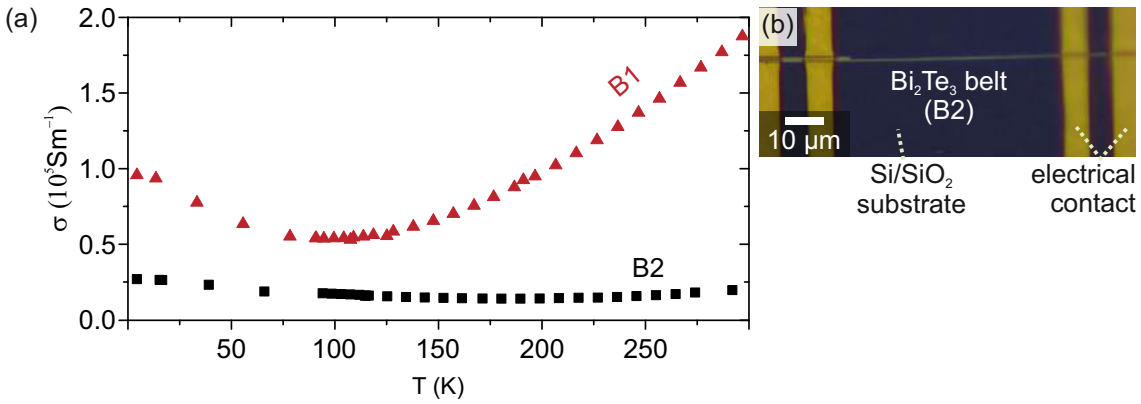

Fig. 6.2.5: Temperature-dependent electrical conductivity $\sigma(T)$ of two Bi_2Te_3 belts from the same batch as function of temperature T. The inset shows a microscope image of the contacted B2 allowing for measurements in four-point configuration.

surface effects may be, at least in parts, the origin of the higher electrical conductivity of B2 [206].

A plot of the temperature-dependent electrical conductivity is shown in Fig. 6.2.5. Both belts show a minimum in the conductivity at an intermediate temperature of 185 K for B1 and 95 K for B2, respectively. A characteristic minimum in the conductivity has also been observed in Bi_2Te_3 bulk samples and nanostructures grown by different methods [207–211]. The feature appears at a temperature when the contribution of the surface conduction to the total conductivity becomes significant compared to the bulk contribution at a carrier density below 1×10^{17} cm^{-1}. The conductivity is as low as for pure bulk Bi_2Te_3 which is an advantage for the observation of the TSS and a sign of excellent crystal quality.

Table 6.2.2: Summary of the electrical conductivity σ at room temperature, the belt width w_B, height h_B, and length of the central part l_B, and the surface-to-volume-ratio S/V.

Sample	σ 10^5 Sm^{-1}	w_B nm	h_B nm	l_B μm	S/V 10^7 m^{-1}
B1	0.2	246	261	31.4	1.58
B2	1.88	514	131	52.5	1.92

6.3 Sn and Bi_2Te_3

This section presents a study of the vapour transport growth of Sn and Bi_2Te_3. Three types of Sn-Bi_2Te_3 interactions, leading to different structures, can be distinguished: (i) Sn nanoparticle-Bi_2Te_3 heterostructures, (ii) Sn puddles on Bi_2Te_3 plates, and (iii) Sn-doped Bi_2Te_3. In particular the Sn-Bi_2Te_3 heterostructures may be suitable hosts for Majorana fermions [212]. The direct fabrication of heterostructures has the inherent advantage of fewer processing steps and well-defined interfaces, which makes them ideal testbeds for fundamental studies and future applications alike.

Growth time and flow rate were studied systematically and Sn-doped Bi_2Te_3 samples were achieved with a long growth time and relatively low flow rate (8 h at 150 sccm). The density of heterostructures tends to increase when a relatively large quantity of Sn is used, while also supplying the transport gas at a high flow rate (10 granules of 0.6 g each and 700 sccm). The other experimental parameters are listed in Table 6.3.1. The discussion is organised following the three types of interaction.

Table 6.3.1: Experimental parameters for the growth of Sn and Bi_2Te_3.

Parameter		**Value**
growth method		vapour transport
substrate	type	Si(100)
	catalyst coating	TiO_2 P-25
precursor		Bi_2Te_3 and Sn
N_2 flow rate		150–700 sccm
growth temperature		585°C
ramp time		0
growth time		1–8 h
substrate temperature		~480°C
analysis methods		SEM, AFM, Raman, TEM, STEM, EDS

6.3.1 Sn nanoparticle-Bi_2Te_3 heterostructures

Type (i) Sn nanoparticle-Bi_2Te_3 heterostructures are characterised by Sn flakes that homogeneously cover all structures, as can be seen from a comparison of a Sn-free growth in Fig. 6.3.1(a) and a Sn-assisted growth in Fig. 6.3.1(b). TiO_2 catalyst clusters on the substrate can enhance the growth of Sn flakes.

Bi_2Te_3 plates and the tips of belts promote the growth of larger Sn flakes that form cloud-like objects (Fig. 6.3.1(b), upper inset). The density of flakes at the tip of the belt decreases to zero within a few microns away from the tip, and the base of the belt is free of Sn flakes. Plates, on the other hand, are fully covered by large Sn flakes, as can be seen in Fig. 6.3.1(b), lower inset. Sn is contained in clusters, and neither Bi nor Te react with the Sn flakes on top of Bi_2Te_3 plates, as shown in Fig. 6.3.1(c). The SEM image shows white spots that cover the surface of a plate. Corresponding EDS elemental maps show homogeneous concentrations of Bi and Te, but distinguished features of Sn that correspond to the flakes. The flakes are composed of ~20-nm-diameter Sn nanoparticles, as shown in Fig. 6.3.1(d). If the coverage is lower the nanoparticles do not form flakes but stay rather separated, as shown in Fig. 6.3.1(e).

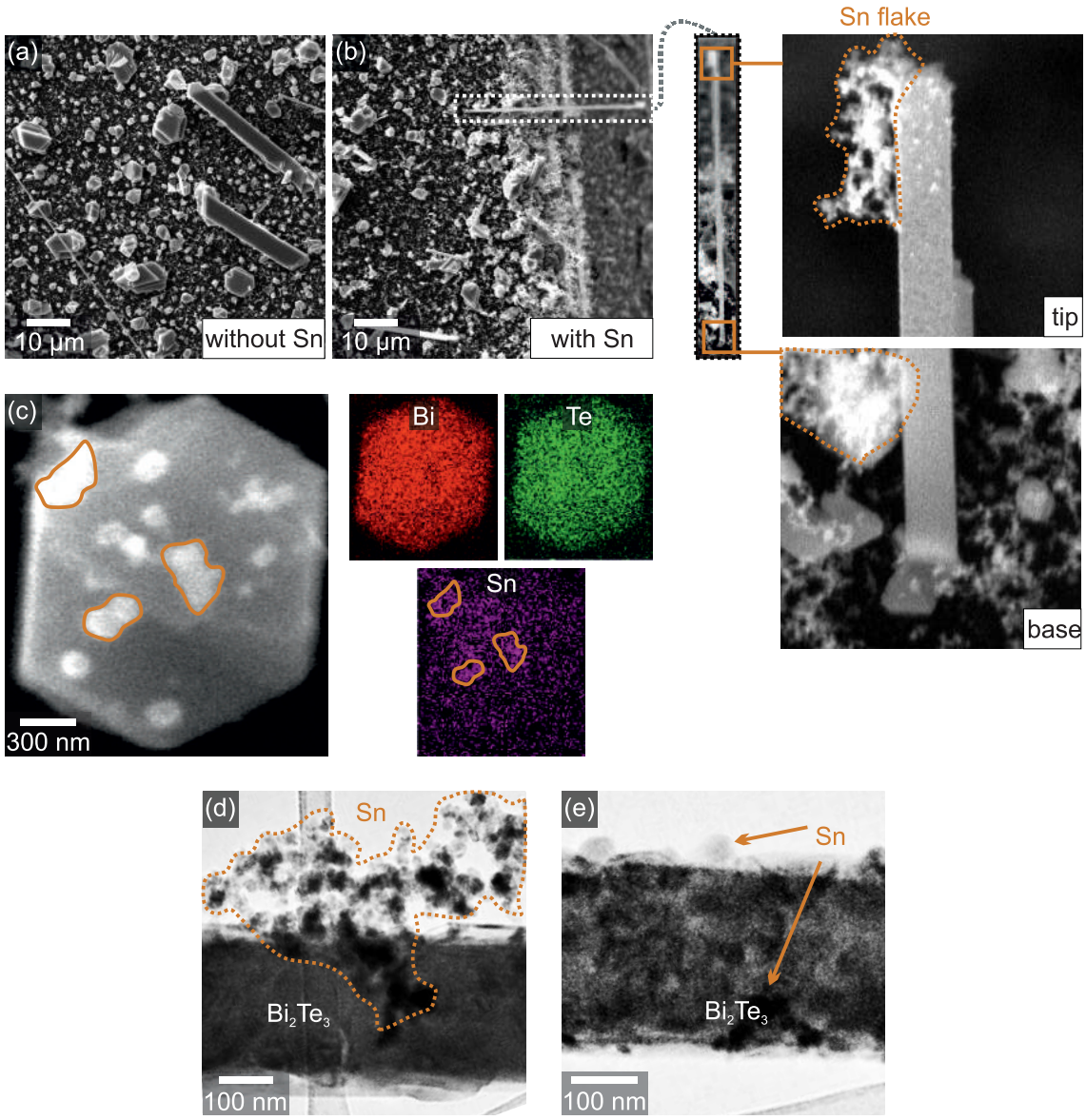

Fig. 6.3.1: Sn flakes on Bi_2Te_3 structures (type (i)). SEM comparison of the growth (a) without and (b) with Sn precursor. Flakes preferentially grow on Bi_2Te_3 structures such as plates and the tip of belts (upper inset). Their coverage decreases towards the base of the ribbons (lower inset). (c) SEM image of a hexagonal plate covered with flakes (left), and EDS maps showing the elemental composition for Bi, Te, and Sn (right). Bi and Te are homogeneously distributed, while Sn in concentrated in the flakes (areas of high concentration are indicated by yellow outlines). (d) TEM micrograph of a Sn flake attached to a belt. The flake consists of Sn nanoparticles. (e) TEM image of Sn nanoparticles attached to a Bi_2Te_3 belt. Instrument (a-c): Jeol JSM-6610LV; acceleration voltage: 20 keV. Instrument (d,e): Jeol 2100.

6.3.2 Sn puddles on Bi_2Te_3 plates

Type (ii) Sn puddles on Bi_2Te_3 plates appear as white spots on a metallic surface under an optical microscope (see Fig. 6.3.2(a)). The part near the base of the plate is nearly free of puddles, whereas the coverage at the top is very high, similar to the coverage of belts by Sn flakes. Most of the puddles have triangular shapes that are aligned with respect to each other (Fig. 6.3.2(b)). This is most likely a consequence of the underlying hexagonal crystal structure of Bi_2Te_3. Two lines of puddles in Fig. 6.3.2(c) form a parallelogram with the outline of the plate. This could be due to a growth mechanism that is related to the formation of Sn droplets at step edges of Bi_2Te_3. Indeed, we find a 20 nm hillock at the bottom of a puddle by AFM (Fig. 6.3.2(d)). This could be an initial droplet of Sn at a step edge around which further Bi_2Te_3 layers have grown. The puddle has a width of 1 µm and a depth of 50 nm.

An example of a puddle without a hillock is shown in Fig. 6.3.2(e) in cross-section prepared by FIB. Sn appears as a flat thin layer on top of the relatively thicker Bi_2Te_3 plate. The layer consists of ~15×20 nm sized Sn granules and is recessed beneath the top surface of the Bi_2Te_3 plate by 40 nm. The edges of the layer above connect smoothly into the recession. Smaller granules fill up the space between the large Sn granules, as shown in Fig. 6.3.2(f) in a STEM micrograph. There is a residual concentration of Bi and Te found in this layer, as measured by STEM-EDS and illustrated in Fig. 6.3.2(g).

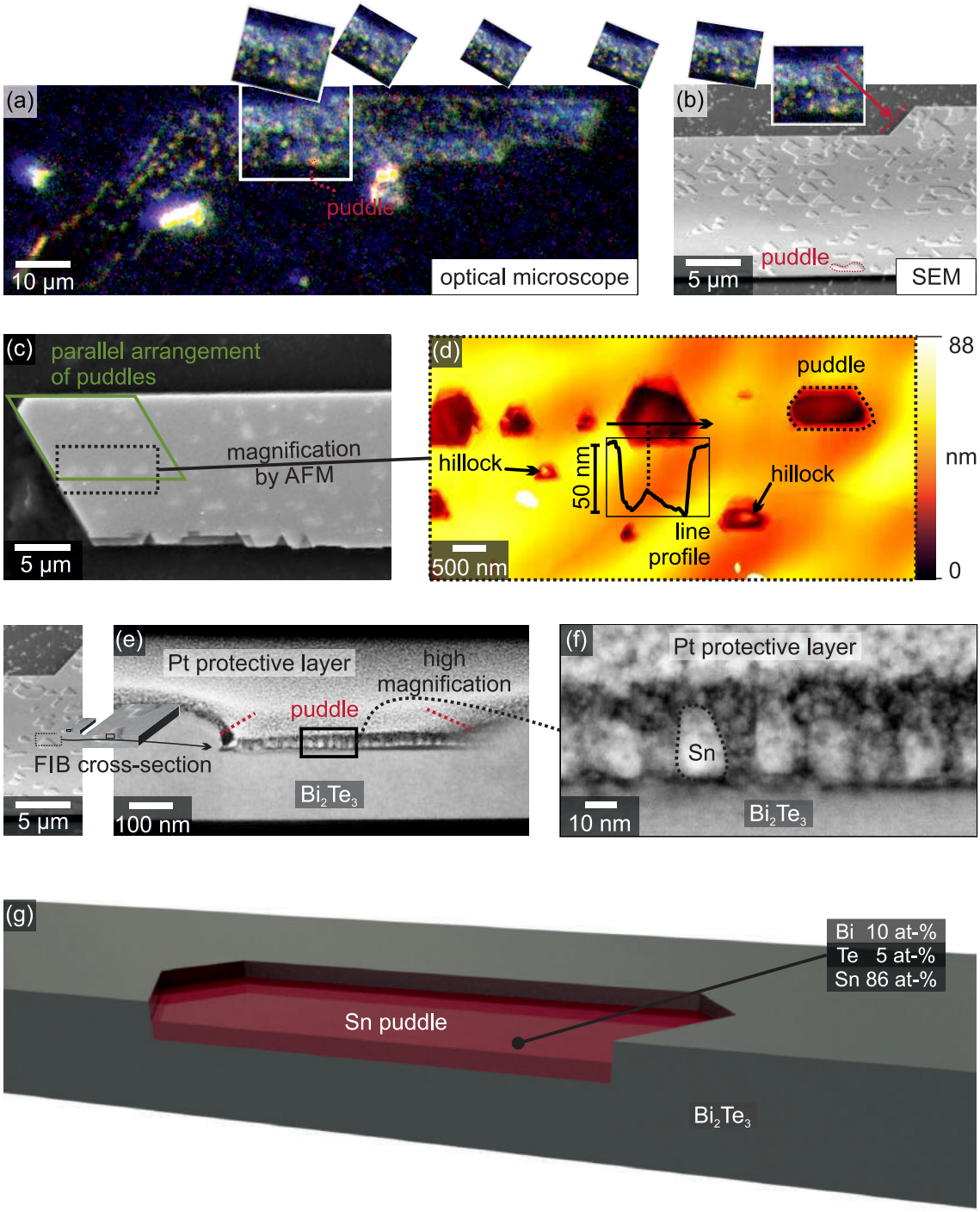

Fig. 6.3.2: Sn puddles on Bi_2Te_3 plates [type (ii)]. (a) Optical microscope image of a pistol-shaped Bi_2Te_3 plate. Sn puddles appear as shiny spots. A white rectangle highlights the area in which the SEM micrograph in (b) was taken. (b) SEM image of triangular Sn puddles on Bi_2Te_3. (c) Tip of another Bi_2Te_3 ribbon. Puddles (green outline) are aligned with the growth front (left) and the edge of the ribbon (top). (d) AFM image of the area marked by a dashed rectangle in (c). The line profile shows that a hillock is located on the bottom of the puddle. Other puddles show similar hillocks. (e) Cross-sectional STEM image of the plate shown in (b). The sample is covered by a protective Pt layer. (f) The high magnification image taken from the Sn-rich layer (indicated by a rectangle) shows that the layer is composed of Sn grains (bright). (g) Illustration of a Sn puddle (red) on a Bi_2Te_3 plate (grey). The atomic composition of the Sn layer is indicated as measured by STEM-EDS. Instrument (b,c): Jeol JSM-6610LV; acceleration voltage: 20 keV. Instrument (e,f): Jeol ARM200F.

6.3.3 Sn-doped Bi_2Te_3 structures

Type (iii) Sn-doped Bi_2Te_3 structures typically have a Sn concentration of ~5 at-% as detected by EDS (Fig. 6.3.3(a)). As compared to undoped Bi_2Te_3 (40 at-% Bi and 60 at-% Te), the doped structures have 36 at-% Bi and 59 at-% Te, which indicates that the Sn concentration comes at the expense of Bi if no additional phases such as SnTe are formed. We estimate the instrumental error for the SEM-EDS experiments to be ±1% of the stated concentrations. In order to exclude the possibility of secondary phase formation, we transferred an ensemble of nanostructures from the as-grown substrate to a micro-loop suitable for x-ray transmission experiments. The diffraction pattern resembles pure Bi_2Te_3, as can be seen in Fig. 6.3.3(b). Bi_2Te_3 peaks are indexed based on diffraction data for Bi_2Te_3 [213]. In particular, there are no additional phases and Sn does not cause a measurable lattice distortion as the peak positions can be matched with ±0.1° accuracy. These observations are consistent with mainly substitutional doping of Sn atoms on Bi lattice sites. Interstitial doping at random places of the crystal lattice cannot be completely excluded because it would not affect the diffraction pattern.

In Fig. 6.3.3(c) the Raman spectrum of pure Bi_2Te_3 which has modes at 61.7, 100.8,

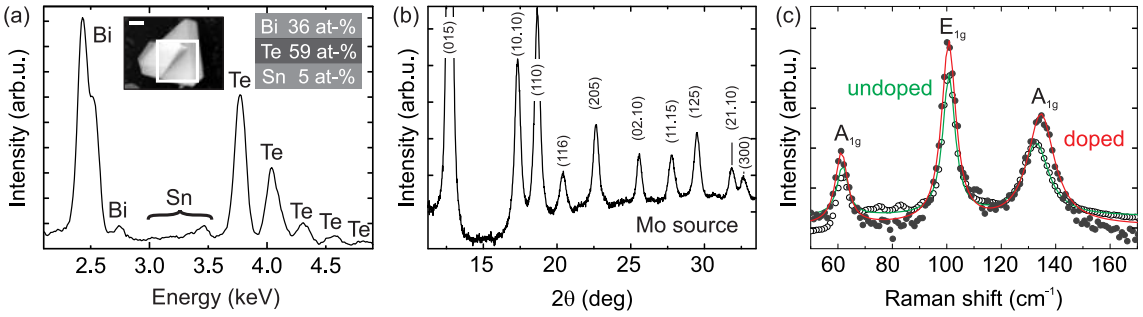

Fig. 6.3.3: Sn-doped Bi_2Te_3 nanostructures [type (iii)]. (a) EDS spectrum of a plate. The inset shows an SEM image with the scan area marked by a white rectangle. The white scale bar corresponds to 1 µm. The Sn doping concentration is 5 at-%. Instrument: Jeol JSM-6610LV; acceleration voltage: 20 keV. (b) Integrated powder XRD pattern taken by using a Mo x-ray source on the Agilent Supernova. The Bi_2Te_3 diffraction peaks are indexed. (c) Raman spectra of Sn-doped (dark filled dots, red fit) and undoped (empty dots, green fit) Bi_2Te_3. The data points are fitted using Lorentzian line shapes. The A_{1g} mode is shifted by 2 cm^{-1} between the doped and the undoped sample. Instrument: Renishaw; wavelength: 830 nm.

and 132.8 cm^{-1} is compared with a Sn-doped sample [110]. The A_{1g} mode is slightly shifted. This is similar to Raman measurements on ternary $(Bi_{1-x}Sb_x)_2Te_3$ compounds where the A_{1g} mode is most sensitive to changes in the concentration of Sb for small x [198]. It moves by 1.3% towards higher frequencies (from 132.8 to 134.6 cm^{-1}), since Sn is lighter than Bi. The two lower modes are shifted by less than 1% to lower frequencies which is within the instrumental error of the Raman system. Sn and Sb are next to each other in the periodic table with a relative mass difference of 2.5%, so the energy of the lattice vibrations is nearly the same. Therefore, we used the literature data for $(Bi_{1-x}Sb_x)_2Te_3$ to estimate the concentration of Sn causing the shift of the Raman line. A Sn concentration of 2% is obtained which is lower than the value from EDS measurements. In summary, Sn substitutes Bi in Bi_2Te_3 and reduces the n-type bulk carrier concentration of the material since it has one valence electron less than Bi [214].

6.3.4 Electronic transport

Electronic transport measurements were carried out on type (i) Sn-Bi_2Te_3 heterostructures. A long heterostructure was selected and four silver paint contacts were applied, as shown in the inset to Fig. 6.3.4. The temperature-dependent resistance of the sample below 5 K is shown in Fig. 6.3.4. During cool-down, the resistance of the structure initially decreased as expected from the undecorated structures [142]. At the superconducting critical temperature of Sn, however, a sudden increase in resistance of $\approx$1 Ω is observed. Note that the density of Sn nanoparticles is below the percolation threshold, so the transport can be assumed to be through the ribbon. Further studies are needed to understand this phenomenon in the framework of TI-superconductor proximity coupling.

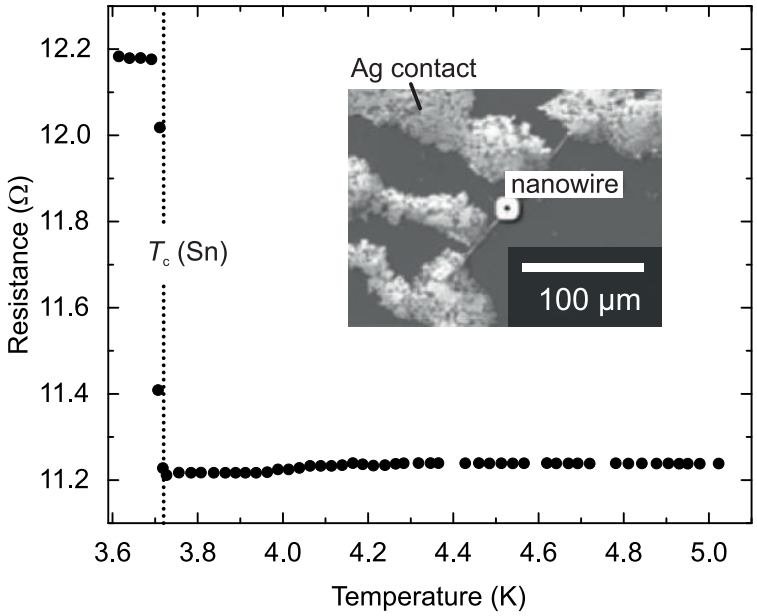

Fig. 6.3.4: Resistance of a type (i) structure as a function of temperature. The 4-point contact measurement on a Sn-Bi_2Te_3 heterostructure (inset, SEM, Jeol JSM-6610LV at 20 keV) shows a jump in resistance at the superconducting transition temperature (T_c) of Sn of ≈3.72 K.

Conclusion

We have performed a systematic growth study of the Sn-assisted synthesis of Bi_2Te_3 nano- and microstructures using physical vapour transport. Three different growth scenarios were observed depending on the growth conditions: cloud-like Sn-decorated Bi_2Te_3, the local formation of Sn-rich areas on Bi_2Te_3 plates (puddles), and Sn-doped Bi_2Te_3. While the cloud-like Sn growth is related to tips and catalyst sites, the formation of Sn puddles is based on the spontaneous resublimation of Sn droplets on the surface of Bi_2Te_3. The different growth regimes are controlled by the Sn precursor quantity, carrier gas flow rate, and growth time. Each type has its specific application potentials. The high aspect ratio of nanoparticles – in combination with the controllable structure of a belt-like backbone as in the Sn-decorated structures – is desirable,e.g., for sensors [174,215,216]. Superconductor-TI layered heterostructures in the form of Sn puddles on Bi_2Te_3 are promising candidates for the observation and study of Majorana fermions, and ultimately topological quantum computation [217]. First transport measurements show an interesting jump in resistance at the supercon-

ducting transition temperature of Sn. Finally, Sn doping holds the promise to align the chemical potential within the band gap of Bi_2Te_3 which could contribute to making use of the TSS in spintronic devices. Therefore, the combination of Sn and Bi_2Te_3 is very promising for future applications.

7 Cd_3As_2 nanowires: basic properties

Introduction

After introducing nanostructure growth in Chapter 4 and focusing on two classes of TI nanowires in Chapter 5 and Chapter 6, I now turn to the more recently discovered *quantum material* Cd_3As_2, a 3D Dirac semimetal [34, 218]. In transport measurements a protection mechanism was found that suppresses backscattering in Cd_3As_2 and leads to a low temperature (5 K) mobility of 9×10^6 cm^2 V^{-1} s^{-1}, which is close to the highest reported mobility of 3.6×10^7 cm^2 V^{-1} s^{-1} in 2D electron gases in AlGaAs/GaAs, and much higher than in graphene [219, 220]. Moreover, a small effective mass leads to a large exciton radius making such materials interesting objects for the study of quantum confinement in nanostructures. This chapter presents a structural study of Cd_3As_2 nanowires in the first part and a study of the electrical properties via THz measurements in the second part. THz measurements and data analysis including fitting was carried out by Dr Jessica Boland (University of Oxford).

7.1 Crystal structure

The crystal structure of Cd_3As_2 can be visualised as a face-centered cubic lattice for As, and a smaller, inner cube containing Cd atoms at its corners, as shown in Fig. 7.1.1. In the low temperature, non-centrosymmetric $I4_1cd$ form, which displays the characteristics of a 3D topological semimetal, two regular Cd vacancies appear on adjacent faces of the Cd cube at opposite corners [34].

X-ray powder diffraction was carried out to determine the crystal structure and its variation across an ensemble of nanowires retrieved from a Si substrate. The integrated powder diffraction pattern of a nanowire ensemble was fitted using Topas. Figure 7.1.2(a) shows that the nanowires indeed have the desired crystal structure of α-Cd_3As_2 (space group $I4_1cd$). The calculated value of the [112]-direction inter-

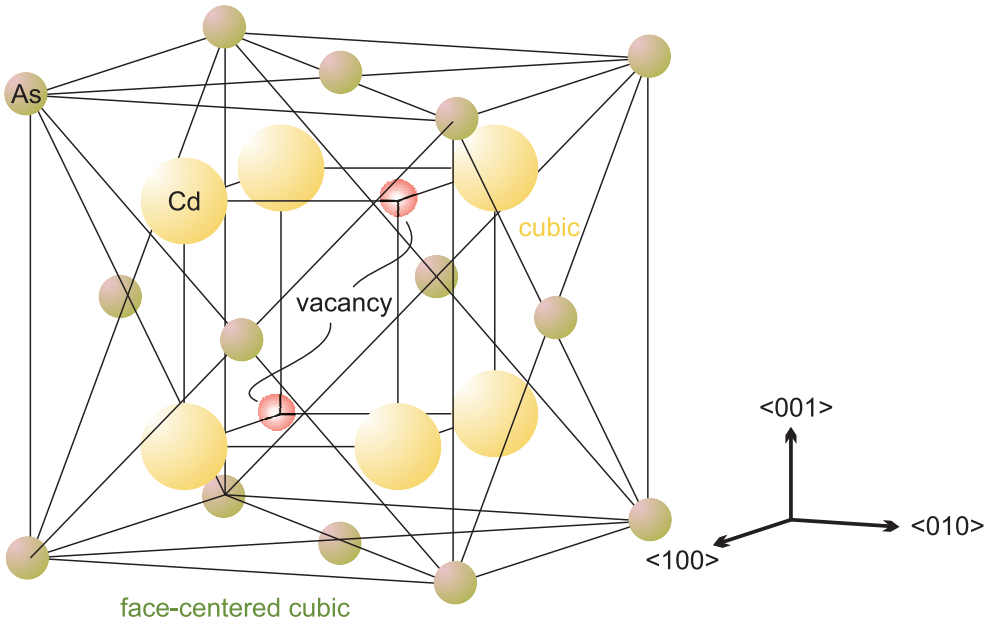

Fig. 7.1.1: The crystal structure of Cd_3As_2 consists of a face-centered cubic lattice of As atoms and an intercalated cubic lattice of Cd atoms. Two vacancies on the Cd-lattice are indicated by red spheres.

planar spacing is 0.732 nm, consistent with results from the TEM analysis shown in Fig. 7.1.2(b). The high-resolution lattice-resolved imaging shows growth along the [112]-direction with an interplanar distance of (0.73±0.05) nm.

Raman spectroscopy was carried out on a single nanowire using a laser wavelength of 830 nm on the Horiba system by Dr Patryk Kusch (Freie Universiät Berlin). The low wavenumber part of the spectrum is not accessible due to experimental limitations of the setup. The lowest mode at 93 cm^{-1} is overshadowed by a sharp increase in intensity near the cut-off region [222]. Jandl *et al.* [222] also report a single peak at 194 cm^{-1} using a 647 nm laser wavelength. We find an additional peak at 178 cm^{-1}, and two more modes at around 300 cm^{-1} which coincide with a mode at 300 cm^{-1} reported by Weszka *et al.* [223]. The authors did not comment on the satellite peak at 309 cm^{-1} which has half of the intensity of the main peak [223].

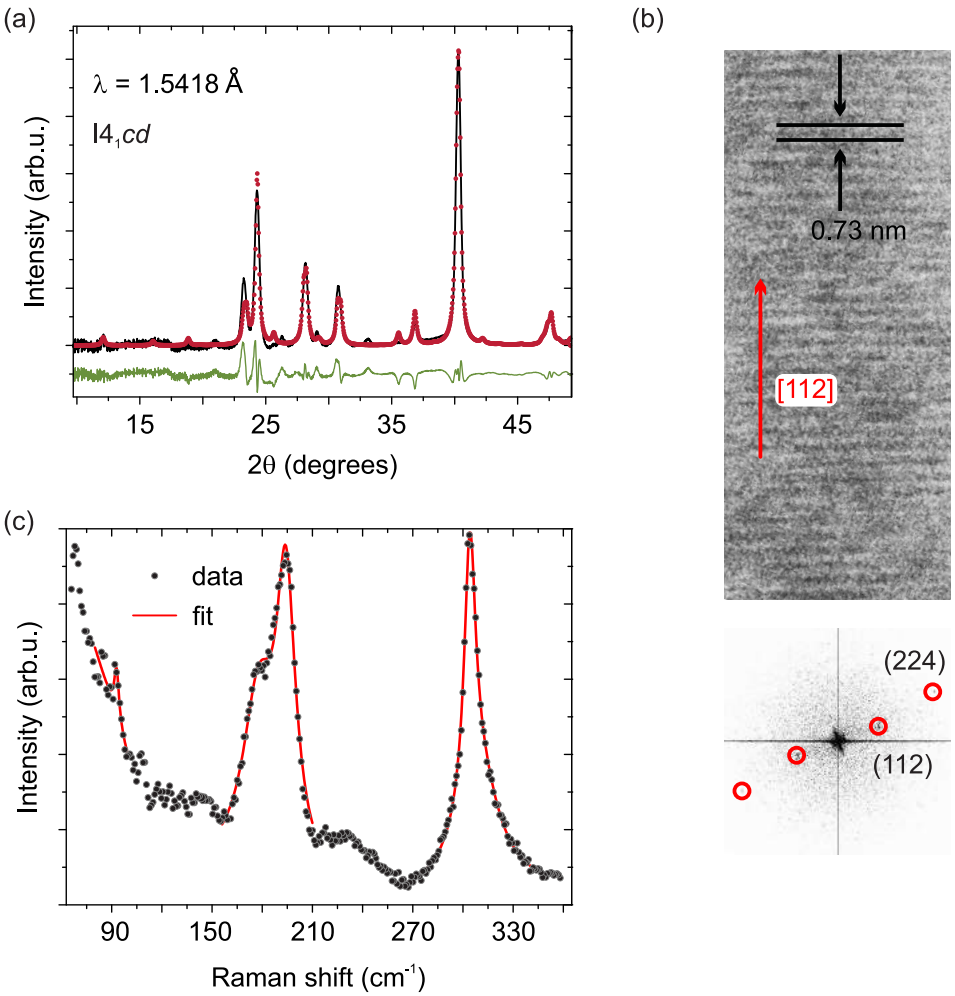

Fig. 7.1.2: (a) Integrated x-ray diffraction pattern from Cd_3As_2 nanowires (black curve) and simulated pattern (red curve) [221]. The difference between the diffraction pattern and the simulated pattern is shown as the green curve. Data was taken on the Agilent Supernova. (b) Lattice-resolved TEM micrograph showing a lattice spacing of 0.73 nm, indicating growth along the [112]-direction (red arrow). The inset is a Fourier transform of the lattice image. Red circles indicate the reciprocal lattice points of the (112) and (224) planes in the α-Cd_3As_2 structure. Instrument: Jeol 2100. (c) Raman spectrum of a Cd_3As_2 nanowire recorded on the Horiba T64000 Raman spectrometer system. The data (dots) is fitted using Lorentzian line shapes (red curves). Vibrational modes are identified at 93, 178, 194, 304, and 309 cm^{-1}.

7.2 Electrical conductivity

Optical pump-THz probe spectroscopy is used to extract the electronic mobility of an entire sample without the need for making electrical contacts as described in Chapter 3. Nanowires are deposited on a transparent quartz substrate, similar to Fig. 7.2.1(a), and their diameter is determined as an average of 123 wires by counting (SEM image). The histogram in Fig. 7.2.1(b) shows that the average is 126 nm with a standard deviation of 35 nm which is a result of the tapered growth and of smaller wires growing on the sidewalls of larger wires, as can be seen in Fig. 7.2.1(c). This secondary growth is consistent with the fact that the first order nanowires grow from Cd_3As_2 clusters.

The fluence of the laser that creates the photoexcitation can be tuned to set the initial photoinjected electron density. Thus, a higher fluence leads to a higher photoinduced conductivity, as can be seen in Fig. 7.2.2(a).

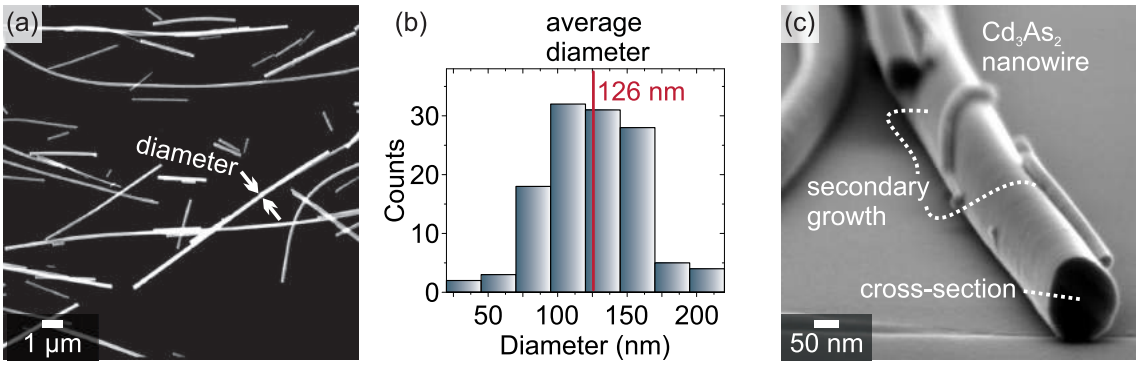

Fig. 7.2.1: Measurement of the diameter of Cd_3As_2 nanowires. (a) SEM micrograph of nanowires transferred onto another substrate. (b) Diameter distribution of 123 nanowires. The average diameter is (126±35) nm. (c) Cross-section of a nanowire in SEM obtained by breaking a Si wafer with nanowires deposited on it. The cross-section is circular and smaller wires grow on the sidewalls of larger ones. Instrument: FEI Quanta 600 FEG; acceleration voltage: 30 keV.

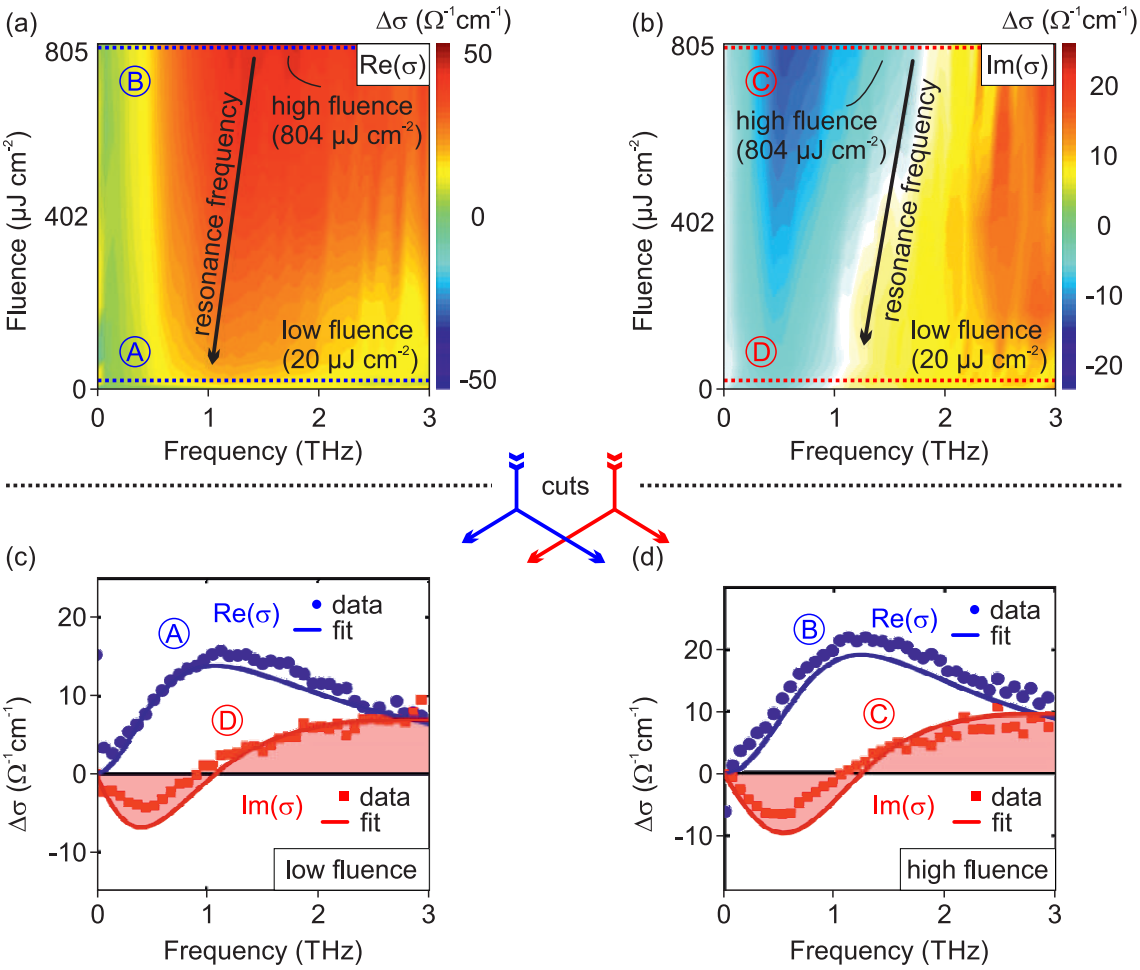

Fig. 7.2.2: Color maps of the (a) real and (b) imaginary parts of the time-resolved conductivity of photoexcited electrons as a function of frequency and fluence at 5 ps after photoexcitation of the Cd_3As_2 nanowires. The black arrow indicates the position of the resonance frequency. (c–d) Cuts through the colour maps at (c) low and (d) high fluence.

The resonance frequency (indicated by an arrow) marks the position of the plasmon response for the photoconductivity of the nanowire. The imaginary part of the photoconductivity is zero at this position, as shown in Fig. 7.2.2(b). The mobility calculation requires the momentum scattering rate γ that can be obtained by fitting cuts through the spectral colour maps with a Lorentzian conductivity response, as shown in Fig. 7.2.2(c) for a low fluence and Fig. 7.2.2(d) for a high fluence. The mobility is then

$$\mu = \frac{e}{m_e^* \gamma} = (6040 \pm 620) \frac{\mathrm{cm}^2}{\mathrm{V \cdot s}}, \tag{7.2.1}$$

where an effective electronic mass of $m_e^* = 0.023 m_0$ and the electronic charge e were

used [224]. This value agrees with the mobility reported on individual nanowires mentioned above. The next step would be to add THz measurements in the low temperature range to complete the picture.

Conclusion

XRD measurements, TEM, and Raman spectroscopy confirm that the nanowires are indeed α-Cd_3As_2. Cd_3As_2 single crystals have an electron mobility of up to $9 \times 10^6 \frac{cm^2}{V \cdot s}$ [219]. The highest mobility measured in nanowires measured by Zhang *et al.* is two orders of magnitude smaller with $3.2 \times 10^4 \frac{cm^2}{V \cdot s}$ at low temperature [225]. The sample used here has a mobility of $(6040 \pm 620) \frac{cm^2}{V \cdot s}$ measured on an ensemble of nanowires at room temperature. This is in agreement with the single nanowire room temperature mobility of Zhang *et al.* at $\sim 8.1 \times 10^3 \frac{cm^2}{V \cdot s}$ (extrapolated from their data at 200 K).

8 Conclusions and outlook

Introduction

Understanding how crystals grow is as important as the study of their physical properties. Sixty years have passed since Ellis and Wagner presented the first growth model for Si whiskers [69]. Since then the number of materials that have been synthesised as nanowires has been increasing significantly. This thesis presented studies of five selected materials: Bi_2Se_2Te, Bi_2Se_3, Bi_2Te_3, SnO_2, and Cd_3As_2. In the following, I summarise these findings and results from the characterisation and put them into context. Finally, I will point out further research and potential applications.

8.1 Growth

Starting from the first step of nanowire growth, i.e., cluster formation on a substrate, I studied Au catalyst particles on Si that had been used in an interrupted growth experiment. The precursor material from Bi_2Se_2Te vapour accumulated around the catalyst particle. Nucleation was driven from the root rather than from the tip in contrast to similar experiments in the literature. This was explained with reference to the particle size: Large catalyst particles lead to tip-catalysed growth, whereas smaller particles catalysed the growth from the root.

In Sb-doped Bi_2Se_3, however, Au was found to contaminate the entire nanowire sidewall. TiO_2 was introduced as a novel catalyst and that did not show any negative side-effects, whilst, simultaneously, the nanowire yield could even be improved. Whereas Au is liquid during the growth and absorbs Se from the precursor, TiO_2 stays well separated at the root of the grown structures. However, a preferential deposition of Se/Te was observed here as well.

The efficiency of TiO_2 was confirmed in the growth of Bi_2Te_3 nanowires. Catalyst-free growth of this material is also possible, but the nanowire yield is much higher

if a catalyst is used, as could be demonstrated under identical growth conditions in vapour transport growth. In MBE, Bi_2Te_3 nanowires grow catalyst-free and the size can be tuned by the substrate temperature. Due to the lower precursor flux rate and ultra-high vacuum environment, these structures have a better crystalline quality and are smaller than samples that were grown using vapour transport. The use of MBE, in addition to synthesising high quality nanostructures, provides the unique opportunity to grow nanowire heterostructures to combine other functionalities with TIs and create novel device structures. Nanowires with a tunable size are ideal candidates to study the transition from a 3D TI to an ordinary insulator as the diameter passes a certain threshold to a 1D system. This experiment would require a combined MBE/ARPES chamber to avoid sample contamination due to air exposure.

The next step for MBE growth is to reproduce and control the step-flow growth mode observed in Bi_2Te_3 sub-micron belts in vapour transport growth. Thin films suffer from surface roughening due to the spiral-like growth mode of Bi_2Te_3 thin films. This makes it challenging to grow atomically sharp interfaces and promotes delamination, e.g., in TEM sample preparation. Layered nanowire heterostructures (sandwiches) would be easier to handle and enable studies with high interface quality. Such devices are milestones on the road from pure material research to p-n-junctions and spin-transistors.

There is a lot of potential to be explored with metal-oxide catalysts, heterogeneous catalysts, and catalyst size dependent experiments. Further research could focus on deliberately contaminating nanowires with certain catalyst materials to explore interface effects and promote electronic contacting. This requires custom-made catalyst solutions since commercially available solutions only offer a limited range of options. However, custom-made solutions come with the disadvantage of a broader size distribution and reduced stability.

The growth mechanisms of nanowires of the non-layered materials Sb-doped Bi_2Se_3, Cd_3As_2, and SnO_2 each have unique features: Bi_2Se_3 nanowires incorporate Sb in a way that resembles surfactant mediated growth in thin films. It would be interesting to generalise this study, e.g., for other surfactant/nanowire material combinations that are known from thin film growth. Interestingly, Cd_3As_2 nanowires grow in a tip-catalysed process from an As-rich tip, most likely because Cd has the higher vapour pressure. In other II-V and III-V compounds the opposite is the case: The catalytic tip is formed of the group II or III element and As is absorbed by the liquid II/III droplet. SnO_2 also grows following the VLS scheme but in some wires, the catalyst particle at the tip is consumed by the growth and the tip is tapered. Catalyst-splitting mediated branching enables the growth of nanotrees–SnO_2 structures resembling trees on the nanoscale. The one-step growth of such structures has the potential to save costs for the production of gas sensors.

8.2 Characterisation

One of the highlights of this work is the discovery of a quasi 1D TI in Sb-doped Bi_2Se_3 nanowires. This system is an exception in the family of layered Bi/Sb based TIs because its crystal structure is made of atomic chains. ARPES was able to confirm the existence of linear dispersing TSS but it would be important to analyse the symmetry of the reciprocal space further, e.g., by constant binding energy maps. Electronic transport measurement, perhaps on larger wires, would serve as a cross-check to confirm the topological nature of the material.

The challenge for electronic transport measurements is the deposition of the nanowires on a suitable substrate and unwanted melting of contacted structures if the current is too high. Bi_2Te_3 nanowires could be driven into almost macroscopic scales by long growth times. These structures are very stable under manipulation by micro-

instruments and take relatively high currents so that they could be used in electronic transport measurements. Resistance versus temperature curves confirm the semiconducting behaviour of the bulk and the metallic surface states.

The interaction of Bi_2Te_3 with Sn in the growth of nanostructures showed three types of interactions: formation of nanoparticle clusters on the sidewalls, Sn puddles, and Sn doping. The first two are superconductor/TI hybrid structures that are expected to show exotic physics at the interface. These effects might show up in electronic transport measurements as indicated by the initial results. Sn-doping reduces intrinsic doping as known from studies on bulk crystals. The fact that nanowires can be doped as well is an important finding for device applications.

Characterisation of Cd_3As_2 nanowires by THz spectroscopy with respect to electronic mobility and carrier scattering rate showed that the nanowires perform at a similar level as the bulk materials which is known for its record-high mobility. Since very little is known about these nanowires, further studies should exploit similarities to the well-known III-V systems and explore differences that emerge from the topological nature of Cd_3As_2.

In summary, this thesis fills important gaps in the phenomenological understanding of the growth mechanism of *quantum materials* nanowires and provides essential characterisation of their electronic properties. It forms the basic foundation to explore the full potential of such nanostructures further within collaborations with spectroscopy, microscopy, electronic transport, and life science groups.

9 Appendix

A On-film growth of Ge nanowires

Ge is the much neglected semiconductor that has launched the information age with the first transistor in 1947 [226]. It was later replaced by the cheaper alternative Si [227]. Now, Ge is used in infrared photodetectors [228] and high frequency transistors [229] due to its high electronic mobility of $> 1000 \frac{cm^2}{V \cdot s}$ [230]. Ge nanowires can be grown via VLS growth using CVD in an Au-catalysed process [231]. A post-growth HCl etching step is required for cleaning due to Au contamination of the sidewalls [232]. This makes Ge an interesting platform to introduce TiO_2 as an alternative catalyst for nanowire growth.

Ge nanowires were grown by MBE using the parameters summarised in Table A .1.

Table A .1: Experimental parameters for the MBE growth of Ge nanowires.

Parameter		**Value**
growth method		MBE
base pressure		~5×10^{-10} Torr
substrate	type	Si(100)
	preparation	Au, TiO_2 P-25
Temperature	Ge cell	1120°C
	substrate	600°C
growth time		30 min
analysis methods		SEM, AFM

The goal is to reproduce MBE growth from Au nanoparticles from previous work [233, 234] and introduce TiO_2 as an alternative catalyst. Five samples were prepared using (7±1)-nm-diameter Au catalyst particles. Ge was grown for 15 min at substrate temperatures 550, 650, and 700°C. A 600°C sample was grown for 70 min. All samples are covered by a Ge thin film. The sample grown for 70 min has a rougher surface than the other three so that it has sufficient contrast in SEM, as shown in Fig. A .1(a). Nanowires were not observed on any of these samples.

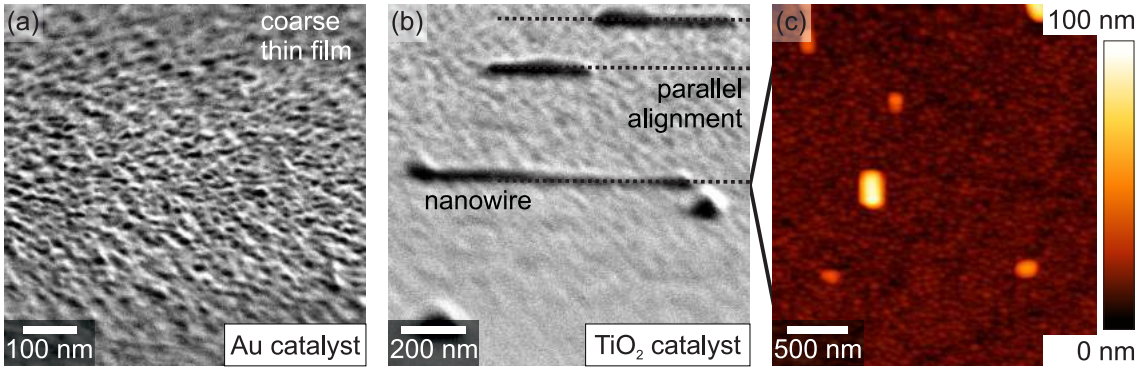

Fig. A .1: (a) SEM side-view of an as-grown Ge thin film grown on Si substrate coating using Au nanoparticles. (b) Ge nanowires on the rough surface of a Ge thin film on a substrate prepared using TiO_2 nanoparticles in SEM side-view. (c) AFM image of the sample in (b). The maximum height of the structures is 100 nm. Instrument (a,b): Jeol JSM-6610LV; acceleration voltage: 20 keV.

Another sample was prepared using (20±6)-nm-diameter TiO_2 P-25 nanoparticles. This sample was grown at 600°C for 30 min (see Fig. A .1(b)). It shows nanowires and nanodots that are growing flat up to 1 µm length on the surface of the thin film. The height of the nanowires is on the order of several tens of nanometres whereas dots can be up to 100 nm high, as can be seen in the AFM image in Fig. A .1(c). The nanowires are grown parallel to each other indicating an epitaxial relationship to the thin film underneath.

This proof of concept shows that TiO_2 is a potential alternative catalyst beyond TI materials and should be considered for well-established nanowire systems as well.

B Bibliography

[1] Hoddeson, L. *Out of the Crystal Maze: Chapters from the History of Solid State Physics*. Oxford University Press, New York and Oxford, (1992).

[2] Born, M. *Dynamik der Kristallgitter*. B.G. Teubner Verlag, Leipzig and Berlin, (1915).

[3] Wilson, A. H. *Proc. Roy. Soc. A* **133**, 458 (1931).

[4] *Editorial. Nat. Phys.* **12**, 105 (2016). 'The rise of quantum materials'.

[5] Vincent, J. *www.independent.co.uk* (2013). '"Digital downtime" means we spend more than five days each year waiting for computers to load' [Online; accessed Nov 25, 2016].

[6] Prati, E., Michielis, M. D., Belli, M., Cocco, S., Fanciulli, M., Kotekar-Patil, D., Ruoff, M., Kern, D. P., Wharam, D. A., Verduijn, J., Tettamanzi, G. C., Rogge, S., Roche, B., Wacquez, R., Jehl, X., Vinet, M., and Sanquer, M. *Nanotechnology* **23**, 215204 (2012).

[7] Wolf, S. A., Chtchelkanova, A. Y., and Treger, D. M. *IBM J. Res. Dev.* **50**, 101 (2006).

[8] Ohno, H. *Science* **281**, 951 (1998).

[9] Schmehl, A., Vaithyanathan, V., Herrnberger, A., Thiel, S., Richter, C., Liberati, M., Heeg, T., Röckerath, M., Kourkoutis, L. F., Mühlbauer, S., Böni, P., Muller, D. A., Barash, Y., Schubert, J., Idzerda, Y., Mannhart, J., and Schlom, D. G. *Nat. Mater.* **6**, 882 (2007).

[10] Zhu, H. J., Ramsteiner, M., Kostial, H., Wassermeier, M., Schönherr, H.-P., and Ploog, K. H. *Phys. Rev. Lett.* **87**, 016601 (2001).

[11] Moore, J. E. *Nature* **464**, 194 (2010).

[12] Stern, A. *Nature* **464**, 187 (2010).

[13] Mourik, V., Zuo, K., Frolov, S. M., Plissard, S. R., Bakkers, E. P. a. M., and Kouwenhoven, L. P. *Science* **336**, 1003 (2012).

[14] Das, A., Ronen, Y., Most, Y., Oreg, Y., Heiblum, M., and Shtrikman, H. *Nat. Phys.* **8**, 887 (2012).

[15] Franz, M. *Nat. Nanotechnology* **8**, 149 (2013).

[16] Xu, J.-P., Wang, M.-X., Liu, Z. L., Ge, J.-F., Yang, X., Liu, C., Xu, Z. A., Guan, D., Gao, C. L., Qian, D., Liu, Y., Wang, Q.-H., Zhang, F.-C., Xue, Q.-K., and Jia, J.-F. *Phys. Rev. Lett.* **114**, 017001 (2015).

[17] Twaha, S., Zhu, J., Yan, Y., and Li, B. *Renew. Sustainable Energy Rev.* **65**, 698 (2016).

[18] Tritt, T. M. *Science* **283**, 804 (1999).

[19] Tang, X., Xie, W., Li, H., Zhao, W., Zhang, Q., and Niino, M. *Appl. Phys. Lett.* **90**, 12102 (2007).

[20] Qi, X.-L. and Zhang, S.-C. *Phys. Today* **63**, 33 (2010).

[21] Yamashita, O., Ochi, T., and Odahara, H. *Mater. Res. Bull.* **44**, 1352 (2009).

[22] World Health Organization. *www.who.int* (2012). 'Facts on cancer' [Online; accessed Nov 25, 2016].

[23] Dreifuss, T., Betzer, O., Shilo, M., Popovtzer, A., Motiei, M., and Popovtzer, R. *Nanoscale* **7**, 15175 (2015).

[24] Li, J., Jiang, F., Yang, B., Song, X.-R., Liu, Y., Yang, H.-H., Cao, D.-R., Shi, W.-R., and Chen, G.-N. *Sci. Rep.* **3**, 1998 (2013).

[25] Li, Z., Hu, Y., Howard, K. A., Jiang, T., Fan, X., Miao, Z., Sun, Y., Besenbacher, F., and Yu, M. *ACS Nano* **10**, 984 (2016).

[26] Zhang, X.-D., Chen, J., Min, Y., Park, G. B., Shen, X., Song, S.-S., Sun, Y.-M., Wang, H., Long, W., Xie, J., Gao, K., Zhang, L., Fan, S., Fan, F., and Jeong, U. *Adv. Funct. Mater.* **24**, 1718 (2014).

[27] Patolsky, F. and Lieber, C. M. *Mater. Today* **8**, 20 (2005).

[28] Hasan, M. Z. and Kane, C. L. *Rev. Mod. Phys.* **82**, 3045 (2010).

[29] Hornyak, G. L., Dutta, J., Tibbals, H. F., and Rao, A. *Introduction to Nanoscience*. CRC Press, Boca Raton (Florida), 1st edition, (2008).

[30] Rao, R. and Govindaraj, A. *Nanotubes and Nanowires*. RSC Nanoscience & Nanotechnology. RSC, Cambridge, (2005).

[31] Lu, W. and Xiang, J. *Semiconductor Nanowires: From Next-Generation Electronics to Sustainable Energy*. Smart Materials Series. RSC, Cambridge, 1st edition, (2014).

[32] Nobel Media AB. *www.nobelprize.org* (2014). 'The Nobel Prize in Physics 2016' [Online; accessed Nov 25, 2016].

[33] Wang, Z., Weng, H., Wu, Q., Dai, X., and Fang, Z. *Phys. Rev. B* **88**, 125427 (2013).

[34] Liu, Y., Li, Y. Y., Rajput, S., Gilks, D., Lari, L., Galindo, P. L., Weinert, M., Lazarov, V. K., and Li, L. *Nat. Phys.* **10**, 294 (2014).

[35] Hsieh, D., Xia, Y., Qian, D., Wray, L., Dil, J. H., Meier, F., Osterwalder, J., Patthey, L., Checkelsky, J. G., Ong, N. P., Fedorov, A. V., Lin, H., Bansil, A., Grauer, D., Hor, Y. S., Cava, R. J., and Hasan, M. Z. *Nature* **460**, 1101 (2009).

[36] Schnyder, A. P., Ryu, S., Furusaki, A., and Ludwig, A. W. W. *AIP Conf. Proc.* **1134**, 10 (2009).

[37] König, M., Wiedmann, S., Brüne, C., Roth, A., Buhmann, H., Molenkamp, L. W., Qi, X.-L., and Zhang, S.-C. *Science* **318**, 766 (2007).

[38] Hsieh, D., Qian, D., Wray, L., Xia, Y., Hor, Y. S., Cava, R. J., and Hasan, M. Z. *Nature* **452**, 970 (2008).

[39] Chen, Y. L., Analytis, J. G., Chu, J.-H., Liu, Z. K., Mo, S.-K., Qi, X. L., Zhang, H. J., Lu, D. H., Dai, X., Fang, Z., Zhang, S. C., Fisher, I. R., Hussain, Z., and Shen, Z.-X. *Science* **325**, 178 (2009).

[40] Xia, Y., Qian, D., Hsieh, D., Wray, L., Pal, A., Lin, H., Bansil, A., Grauer, D., Hor, Y. S., Cava, R. J., and Hasan, M. Z. *Nat. Phys.* **5**, 398 (2009).

[41] Kaddouri, H., Bénet, S., Charar, S., Makowaska-Janusik, M., Tedenac, J. C., and Kityk, I. V. *Phys. Rev. B* **62**, 17108 (2000).

[42] Charar, S., Tedenac, J., Potin, V., Viennois, R., Laire, O., Fau, C., and Liautard, B. *Phys. Stat. Sol. (a)* **182**, 669 (2000).

[43] Bianchi, M., Hatch, R. C., Guan, D., Planke, T., Mi, J., Iversen, B. B., and Philip Hofmann. *Semicond. Sci. Technol.* **27**, 124001 (2012).

[44] Zhang, H., Liu, C.-X., Qi, X.-L., Dai, X., Fang, Z., and Zhang, S.-C. *Nat. Phys.* **5**, 438 (2009).

[45] Peng, H., Lai, K., Kong, D., Meister, S., Chen, Y., Qi, X.-L., Zhang, S.-C., Shen, Z.-X., and Cui, Y. *Nat. Mater.* **9**, 225 (2010).

[46] Yan, Y., Liao, Z.-M., Zhou, Y.-B., Wu, H.-C., Bie, Y.-Q., Chen, J.-J., Meng, J., Wu, X.-S., and Yu, D.-P. *Sci. Rep.* **3**, 1264 (2013).

[47] Zhang, Y., Chang, C.-Z., He, K., Wang, L.-L., Chen, X., Jia, J.-F., Ma, X.-C., and Xue, Q.-K. *Appl. Phys. Lett.* **97**, 194102 (2010).

[48] Analytis, J. G., McDonald, R. D., Riggs, S. C., Chu, J.-H., Boebinger, G. S., and Fisher, I. R. *Nat. Phys.* **6**, 960 (2010).

[49] Hong, S. S., Cha, J. J., Kong, D., and Cui, Y. *Nat. Commun.* **3**, 757 (2012).

[50] Lee, C. H., He, R., Wang, Z. H., Qiu, R. L. J., Kumar, A., Delaney, C., Beck, B., Kidd, T. E., Chancey, C. C., Sankaran, R. M., and Gao, X. P. A. *Nanoscale* **5**, 4337 (2013).

[51] Cha, J. J., Kong, D., Hong, S.-S., Analytis, J. G., Lai, K., and Cui, Y. *Nano Lett.* **12**, 1107 (2012).

[52] Nakajima, S. *J. Phys. Chem. Solids* **24**, 479 (1963).

[53] Wang, G., Zhu, X.-G., Sun, Y.-Y., Li, Y.-Y., Zhang, T., Wen, J., Chen, X., He, K., Wang, L.-L., Ma, X.-C., Jia, J.-F., Zhang, S. B., and Xue, Q.-K. *Adv. Mat.* **23**, 2929 (2011).

[54] Ren, Z., Taskin, A. A., Sasaki, S., Segawa, K., and Ando, Y. *Phys. Rev. B* **82**, 241306 (2010).

[55] Bao, L., He, L., Meyer, N., Kou, X., Zhang, P., Chen, Z.-G., Fedorov, A. V., Zou, J., Riedemann, T. M., Lograsso, T. A., Wang, K. L., Tuttle, G., and Xiu, F. *Sci. Rep.* **2**, 726 (2012).

[56] Sulaev, A., Ren, P., Xia, B., Lin, Q. H., Yu, T., Qiu, C., Zhang, S.-Y., Han, M.-Y., Li, Z. P., Zhu, W. G., Wu, Q., Feng, Y. P., Shen, L., Shen, S.-Q., and Wang, L. *AIP Adv.* **3**, 032123 (2013).

[57] Barfuss, A., Dudy, L., Scholz, M. R., Roth, H., Höpfner, P., Blumenstein, C., Landolt, G., Dil, J. H., Plumb, N. C., Radovic, M., Bostwick, A., Rotenberg, E., Fleszar, A., Bihlmayer, G., Wortmann, D., Li, G., Hanke, W., Claessen, R., and Schäfer, J. *Phys. Rev. Lett.* **111**, 157205 (2013).

[58] Brüne, C., Liu, C. X., Novik, E. G., Hankiewicz, E. M., Buhmann, H., Chen, Y. L., Qi, X. L., Shen, Z. X., Zhang, S. C., and Molenkamp, L. W. *Phys. Rev. Lett.* **106**, 126803 (2011).

[59] Cava, R. J. *Nat. Mater.* **12**, 379 (2013).

[60] Rasche, B., Isaeva, A., Ruck, M., Borisenko, S., Zabolotnyy, V., Büchner, B., Koepernik, K., Ortix, C., Richter, M., and van den Brink, J. *Nat. Mater.* **12**, 422 (2013).

[61] Schönherr, P., Zhang, S., Liu, Y., Kusch, P., Reich, S., Giles, T., Daisenberger, D., Prabhakaran, D., Chen, Y., and Hesjedal, T. *Phys. Stat. Sol. - RRL* **9**, 130 (2015).

[62] Autès, G., Isaeva, A., Moreschini, L., Johannsen, J. C., Pisoni, A., Mori, R., Zhang, W., Filatova, T. G., Kuznetsov, A. N., Forró, L., Van den Broek, W., Kim, Y., Kim, K. S., Lanzara, A., Denlinger, J. D., Rotenberg, E., Bostwick, A., Grioni, M., and Yazyev, O. V. *Nat. Mater.* **15**, 154 (2016).

[63] Tanaka, Y., Ren, Z., Sato, T., Nakayama, K., Souma, S., Takahashi, T., Segawa, K., and Ando, Y. *Nat. Phys.* **8**, 800 (2012).

[64] Young, S. M., Zaheer, S., Teo, J. C. Y., Kane, C. L., Mele, E. J., and Rappe, A. M. *Phys. Rev. Lett.* **108**, 140405 (2012).

[65] Hosur, P. and Qi, X. *C. R. Phys.* **14**, 857 (2013).

[66] Lv, B., Weng, H., Fu, B., Wang, X., Miao, H., Ma, J., Richard, P., Huang, X., Zhao, L., Chen, G., Fang, Z., Dai, X., Qian, T., and Ding, H. *Phys. Rev. X* **5**, 031013 (2015).

[67] Schönherr, P., Baker, A. A., Kusch, P., Reich, S., and Hesjedal, T. *Eur. Phys. J. Appl. Phys.* **66**, 10401 (2014).

[68] IBM. *www.research.ibm.com* (2013). 'A Boy And His Atom: The World's Smallest Movie' [Online; accessed Nov 25, 2016].

[69] Wagner, R. S. and Ellis, W. C. *Appl. Phys. Lett.* **4**, 89 (1964).

[70] Wu, Y. and Yang, P. *J. Am. Chem. Soc.* **123**, 3165 (2001).

[71] Kolasinski, K. W. *Curr. Opin. Solid State Mater. Sci.* **10**, 182 (2006).

[72] Kong, D., Randel, J. C., Peng, H., Cha, J. J., Meister, S., Lai, K., Chen, Y., Shen, Z.-X., Manoharan, H. C., and Cui, Y. *Nano Lett.* **10**, 329 (2010).

[73] Alegria, L. D., Schroer, M. D., Chatterjee, A., Poirier, G. R., Pretko, M., Patel, S. K., and Petta, J. R. *Nano Lett.* **12**, 4711 (2012).

[74] Messing, M. E., Hillerich, K., Johansson, J., Deppert, K., and Dick, K. A. *Gold Bull.* **42**, 172 (2009).

[75] Liu, B., Boercker, J. E., and Aydil, E. S. *Nanotechnology* **19**, 505604 (2008).

[76] Pachmann, K. and Leibold, W. *J. Immunol. Methods* **12**, 81 (1976).

[77] Lee, J. S., Brittman, S., Yu, D., and Park, H. *J. Am. Chem. Soc.* **130**, 6252 (2008).

[78] Schmidt, V., Wittemann, J. V., Senz, S., and Gösele, U. *Adv. Mater.* **21**, 2681 (2009).

[79] Gu, G., Burghard, M., Kim, G. T., Düsberg, G. S., Chiu, P. W., Krstic, V., Roth, S., and Han, W. Q. *J. Appl. Phys.* **90**, 5747 (2001).

[80] Jackson, J. B., Kapoor, D., Jun, S.-G., and Miller, M. S. *J. Appl. Phys.* **102**, 054310 (2007).

[81] Putnam, M. C., Filler, M. A., Kayes, B. M., Kelzenberg, M. D., Guan, Y., Lewis, N. S., Eiler, J. M., and Atwater, H. A. *Nano Lett.* **8**, 3109 (2008).

[82] Hannon, J. B., Kodambaka, S., Ross, F. M., and Tromp, R. M. *Nature* **440**, 69 (2006).

[83] Paladugu, M., Zou, J., Guo, Y.-N., Zhang, X., Joyce, H. J., Gao, Q., Tan, H. H., Jagadish, C., and Kim, Y. *J. Appl. Phys.* **105**, 073503 (2009).

[84] Nguyen, P., Ng, H. T., and Meyyappan, M. *Adv. Mater.* **17**, 1773 (2005).

[85] Tuan, H.-Y., Lee, D. C., and Korgel, B. A. *Angew. Chem. Int. Ed.* **45**, 5184 (2006).

[86] Nakata, K. and Fujishima, A. *J. Photochem. Photobiol. C* **13**, 169 (2012).

[87] Ohsaka, T., Izumi, F., and Fujiki, Y. *J. Raman Spetrosc.* **7**, 321 (1978).

[88] Cha, J. J., Koski, K. J., and Cui, Y. *Phys. Stat. Sol. - RRL* **7**, 15 (2013).

[89] Brumfiel, G. *Nat. News* **466**, 310 (2010).

[90] Markov, I. L. *Nature* **512**, 147 (2014).

[91] Müchler, L., Casper, F., Yan, B., Chadov, S., and Felser, C. *Phys. Stat. Sol. - RRL* **7**, 91 (2013).

[92] Huang, B., Lawrence, C., Gross, A., Hwang, G.-S., Ghafouri, N., Lee, S.-W., Kim, H., Li, C.-P., Uher, C., Najafi, K., and Kaviany, M. *J. Appl. Phys.* **104**, 113710 (2008).

[93] Hiralal, P., Unalan, H. E., and Amaratunga, G. A. J. *Nanotechnology* **23**, 194002 (2012).

[94] Carter, C. B. and Norton, M. G. *Ceramic Materials: Science and Engineering*. Springer Science & Business Media, (2007).

[95] Akasaki, I., Amano, H., Sota, S., Sakai, H., Tanaka, T., and Koike, M. *Jpn. J. Appl. Phys.* **34**, L1517 (1995).

[96] Joyce, H. J., Gao, Q., Hoe Tan, H., Jagadish, C., Kim, Y., Zou, J., Smith, L. M., Jackson, H. E., Yarrison-Rice, J. M., Parkinson, P., and Johnston, M. B. *Prog. Quant. Electron.* **35**, 23 (2011).

[97] Goldstein, J., Newbury, D., Joy, D., Lyman, C., Echlin, P., Lifshin, E., Sawyer, L., and Michael, J. *Scanning Electron Microscopy and X-Ray Microanalysis*. Springer, (2003).

[98] Williams, D. and Carter, C. B. *Transmission Electron Microscopy*. Plenum, (1996).

[99] Daisenberger, D. *Transformations among Metastable Amorphous and Crystalline Forms of Silicon* (2009). University College London.

[100] Hammersley, A. P. *Fit2D V12* (2004). 2D data reduction and analysis program.

[101] Bruker AXS. *Topas V4.2* (2009). Rietveld structure refinement software.

[102] Rigaku Corporation. *CrysAlisPro V38* (2016). Data collection and data processing software for small molecule and protein crystallography.

[103] Nobel Media AB. *www.nobelprize.org* (2014). 'The Nobel Prize in Physics 1921' [Online; accessed Nov 25, 2016].

[104] Suga, S. and Sekiyama, A. *Photoelectron Spectroscopy*, volume 176 of *Springer Series in Optical Sciences*. Springer, Berlin, (2014).

[105] Chen, Y. *Front. Phys.* **7**, 175 (2012).

[106] Yaji, K., Harasawa, A., Kuroda, K., Toyohisa, S., Nakayama, M., Ishida, Y., Fukushima, A., Watanabe, S., Chen, C., Komori, F., and Shin, S. *Rev. Sci. Instrum.* **87**, 053111 (2016).

[107] Flöhr, K., Liebmann, M., Sladek, K., Günel, H. Y., Frielinghaus, R., Haas, F., Meyer, C., Hardtdegen, H., Schäpers, T., Grützmacher, D., and Morgenstern, M. *Rev. Sci. Instrum.* **82**, 113705 (2011).

[108] Joyce, H. J., Boland, J. L., Davies, C. L., Baig, S. A., and Johnston, M. B. *Semicond. Sci. Technol.* **31**, 103003 (2016).

[109] Boland, J. L., Casadei, A., Tütüncüoglu, G., Matteini, F., Davies, C. L., Jabeen, F., Joyce, H. J., Herz, L. M., Fontcuberta i Morral, A., and Johnston, M. B. *ACS Nano* **10**, 4219 (2016).

[110] Schönherr, P., Collins-McIntyre, L. J., Zhang, S., Kusch, P., Reich, S., Giles, T., Daisenberger, D., Prabhakaran, D., and Hesjedal, T. *Nanoscale Res. Lett.* **9**, 127 (2014).

[111] Hamdou, B., Kimling, J., Dorn, A., Pippel, E., Rostek, R., Woias, P., and Nielsch, K. *Adv. Mater.* **25**, 239 (2013).

[112] Fan, H. J., Lee, W., Hauschild, R., Alexe, M., Le Rhun, G., Scholz, R., Dadgar, A., Nielsch, K., Kalt, H., Krost, A., Zacharias, M., and Gösele, U. *Small* **2**, 561 (2006).

[113] Sun, X., Yu, B., Ng, G., Nguyen, T. D., and Meyyappan, M. *Appl. Phys. Lett.* **89**, 233121 (2006).

[114] Li, H., Peng, H., Dang, W., Yu, L., and Liu, Z. *Front. Phys. China* **7**, 208 (2012).

[115] Bowker, M., Crouch, J. J., Carley, A. F., Davies, P. R., Morgan, D. J., Lalev, G., Dimov, S., and Pham, D.-T. *J. Phys. Chem. C Nanomater. Interfaces* **117**, 21577 (2013).

[116] Mlack, J. T., Rahman, A., Johns, G. L., Livi, K. J. T., and Markovi, N. *Appl. Phys. Lett.* **102**, 193108 (2013).

[117] Dick, K. A. *Prog. Crys. Growth Charact. Mater.* **54**, 138 (2008).

[118] Breuer, S., Pfüller, C., Flissikowski, T., Brandt, O., Grahn, H. T., Geelhaar, L., and Riechert, H. *Nano Lett.* **11**, 1276 (2011).

[119] Morales, A. M. and Lieber, C. M. *Science* **279**, 208 (1998).

[120] Gather, B. and Blachnik, R. *J. Less-Common Met.* **48**, 205 (1976).

[121] Rabenau, A., Rau, H., and Rosenstein, G. *J. Less-Common Met.* **24**, 291 (1971).

[122] Tuan, H.-Y., Lee, D. C., Hanrath, T., and Korgel, B. A. *Chem. Mater.* **17**, 5705 (2005).

[123] Li, G. H. and Gray, K. A. *Chem. Phys.* **339**, 173 (2007).

[124] Hoffmann, M. R., Martin, S. T., Choi, W. Y., and Bahnemann, D. W. *Chem. Rev.* **95**, 69 (1995).

[125] Ohno, T., Sarukawa, K., Tokieda, K., and Matsumura, M. *J. Catal.* **203**, 82 (2001).

[126] Ohtani, B., Prieto-Mahaney, O. O., Li, D., and Abe, R. *J. Photochem. Photobiol. A: Chem.* **216**, 179 (2010).

[127] Chen, M. S. and Goodman, D. W. *Chem. Soc. Rev.* **37**, 1860 (2008).

[128] Pan, Z. W., Dai, Z. R., and Wang, Z. L. *Science* **291**, 1947 (2001).

[129] Bae, S. Y., Seo, H. W., Park, J., Yang, H., Park, J. C., and Lee, S. Y. *Appl. Phys. Lett.* **81**, 126 (2002).

[130] Zhu, Y.-C., Bando, Y., and Xue, D.-F. *Appl. Phys. Lett.* **82**, 1769 (2003).

[131] Xie, T., Lin, Y., Wu, G., Yuan, X., Jiang, Z., Ye, C., Meng, G., and Zhang, L. *Inorg. Chem. Commun.* **7**, 545 (2004).

[132] Liu, H., Cui, H., Han, F., Li, X., Wang, J., and Boughton, R. I. *Crys. Growth Des.* **5**, 1711 (2005).

[133] Shi, W., Yu, J., Wang, H., and Zhang, H. *J. Am. Chem. Soc.* **128**, 16490 (2006).

[134] Peng, H., Dang, W., Cao, J., Chen, Y., Wu, D., Zheng, W., Li, H., Shen, Z.-X., and Liu, Z. *Nat. Chem.* **4**, 281 (2012).

[135] Guo, Y., Lin, L., Zhao, S., Deng, B., Chen, H., Ma, B., Wu, J., Yin, J., Liu, Z., and Peng, H. *Adv. Mater.* **27**, 4315 (2015).

[136] Zheng, W., Xie, T., Zhou, Y., Chen, Y. L., Jiang, W., Zhao, S., Wu, J., Jing, Y., Wu, Y., Chen, G., Guo, Y., Yin, J., Huang, S., Xu, H. Q., Liu, Z., and Peng, H. *Nat. Commun.* **6**, 6972 (2015).

[137] Zou, Y., Chen, Z. G., Huang, Y., Drennan, J., and Zou, J. In *2014 Conf. Optoelectr. Microelectr. Mat.Dev.*, 11, (2014).

[138] Harrison, S. E., Li, S., Huo, Y., Zhou, B., Chen, Y. L., and Harris, J. S. *Appl. Phys. Lett.* **102**, 171906 (2013).

[139] Kampmeier, J., Borisova, S., Plucinski, L., Luysberg, M., Mussler, G., and Grützmacher, D. *Cryst. Growth Des.* **15**, 390 (2015).

[140] Jauregui, L. A., Pettes, M. T., Rokhinson, L. P., Shi, L., and Chen, Y. P. *Sci. Rep.* **5**, 8452 (2015).

[141] Park, Y.-S. and Lee, J. S. *J. Nanopart. Res.* **16**, 2226 (2014).

[142] Schönherr, P., Zhang, F., Kojda, D., Mitdank, R., Fischer, S., and Hesjedal, T. *Nanoscale Res. Lett.* **11**, 308 (2016).

[143] Cha, J. J., Williams, J. R., Kong, D., Meister, S., Peng, H., Bestwick, A. J., Gallagher, P., Goldhaber-Gordon, D., and Cui, Y. *Nano Lett.* **10**, 1076 (2010).

[144] Schönherr, P., Prabhakaran, D., Jones, W., Dimitratos, N., Bowker, M., and Hesjedal, T. *Appl. Phys. Lett.* **104**, 253103 (2014).

[145] Predel, B. Landolt-Börnstein - Group IV Physical Chemistry, 1. (1992).

[146] Ferhat, M., Tedenac, J. C., and Nagao, J. *J. Cryst. Growth* **218**, 250 (2000).

[147] Lagally, M. G. and Zhang, Z. *Nature* **417**, 907 (2002).

[148] Lv, H. Y., Liu, H. J., Shi, J., Tang, X. F., and Uher, C. *J. Mater. Chem. A* **1**, 6831 (2013).

[149] Zhang, J., Yang, Y., Jiang, F., Xu, B., Li, J., Wang, X., and Wang, S. *Nanotechnology* **16**, 2887 (2005).

[150] He, R., Law, M., Fan, R., Kim, F., and Yang, P. *Nano Lett.* **2**, 1109 (2002).

[151] Woodruff, D. P. *Phil. Trans. R. Soc. A* **373**, 20140230 (2015).

[152] Hsin, C.-L., Wingert, M., Huang, C.-W., Guo, H., Shih, T.-J., Suh, J., Wang, K., Wu, J., Wu, W.-W., and Chen, R. *Nanoscale* **5**, 4669 (2013).

[153] Bales, G. S. and Zangwill, A. *Phys. Rev. B* **41**, 5500 (1990).

[154] Harrison, S. E., Schönherr, P., Huo, Y., Harris, J. S., and Hesjedal, T. *Appl. Phys. Lett.* **105**, 153114 (2014).

[155] Knebl, G. M., Gessler, J. R., Kamp, M., and Höfling, S. *Appl. Phys. Lett.* **105**, 133109 (2014).

[156] Karma, A. and Plapp, M. *Phys. Rev. Lett.* **81**, 4444 (1998).

[157] Liu, Y., Weinert, M., and Li, L. *Phys. Rev. Lett.* **108**, 115501 (2012).

[158] Chen, X., Ma, X.-C., He, K., Jia, J.-F., and Xue, Q.-K. *Adv. Mater.* **23**, 1162 (2011).

[159] He, L., Kou, X., and Wang, K. L. *Phys. Stat. Sol. - RRL* **7**, 50 (2013).

[160] Kamins, T. I., Williams, R. S., Basile, D. P., Hesjedal, T., and Harris, J. S. *J. Appl. Phys.* **89**, 1008 (2001).

[161] Tournié, E. and Ploog, K. H. *Thin Solid Films* **231**, 43 (1993).

[162] Portavoce, A., Berbezier, I., and Ronda, A. *Phys. Rev. B* **69**, 155416 (2004).

[163] Omari, M., Kouklin, N., Lu, G. H., Chen, J. H., and Gajdardziska-Josifovska, M. *Nanotechnology* **19**, 105301 (2008).

[164] Kouklin, N., Sen, S., and Gajdardziska-Josifovska, M. *Appl. Phys. Lett.* **89**, 071901 (2006).

[165] Grap, T., Rieger, T., Blömers, C., Schäpers, T., Grützmacher, D., and Lepsa, M. I. *Nanotechnology* **24**, 335601 (2013).

[166] Takagi, M. *J. Phys. Soc. Jpn.* **9**, 359 (1954).

[167] Okamoto, H. *J. Phase Equilib.* **13**, 147 (1992).

[168] Westmore, J. B., Mann, K. H., and Tickner, A. W. *J. Phys. Chem.* **68**, 606 (1964).

[169] Schönherr, P. and Hesjedal, T. *Chem. Eur. J.* **22**, 13823 (2016).

[170] Yamazoe, N. *Sens. Actuator B-Chem.* **5**, 7 (1991).

[171] Kolmakov, A., Zhang, Y., Cheng, G., and Moskovits, M. *Adv. Mater.* **15**, 997 (2003).

[172] Tiwana, P., Docampo, P., Johnston, M. B., Herz, L. M., and Snaith, H. J. *Energy Environ. Sci.* **5**, 9566 (2012).

[173] Chen, X., Wong, C. K. Y., Yuan, C. A., and Zhang, G. *Sens. Actuator B-Chem* **177**, 178 (2013).

[174] Feng, H., Huang, J., and Li, J. *Chem. Commun.* **49**, 1017 (2013).

[175] Jin, C., Park, S., Kim, C.-W., Choi, M.-S., Lee, C., and Lee, D. *Mater. Lett.* **158**, 5 (2015).

[176] Wang, J. X., Liu, D. F., Yan, X. Q., Yuan, H. J., Ci, L. J., Zhou, Z. P., Gao, Y., Song, L., Liu, L. F., Zhou, W. Y., Wang, G., and Xie, S. S. *Solid State Commun.* **130**, 89 (2004).

[177] Wang, D., Qian, F., Yang, C., Zhong, Z., and Lieber, C. M. *Nano Lett.* **4**, 871 (2004).

[178] Hsu, Y.-J., Lu, S.-Y., and Lin, Y.-F. *Small* **2**, 268 (2006).

[179] Nam, C.-Y., Tham, D., and Fischer, J. E. *MRS Proc.* **1058**, JJ04–03 (2007).

[180] Kawashima, T., Mizutani, T., Nakagawa, T., Torii, H., Saitoh, T., Komori, K., and Fujii, M. *Nano Lett.* **8**, 362 (2008).

[181] Earley, J. W. *Am. Mineral.* **35**, 337 (1950).

[182] Kuznetsov, V. G. and Palkina, K. K. *Russ. J. Inorg. Chem.* **8**, 624 (1963).

[183] Neumann, G. and Scheidegger, R. *Helv. Phys. Acta* **40**, 293 (1967).

[184] Zhao, J., Liu, H., Ehm, L., Dong, D., Chen, Z., and Gu, G. *J. Phys. Condens. Matter* **25**, 125602 (2013).

[185] Vereshchagin, L. F., Itskevich, E. S., Atabaeva, E. Y., and Popova, S. V. *Sov. Phys. - Solid State* **6**, 1763 (1965).

[186] Cook, N. J., Ciobanu, C. L., Wagner, T., and Stanley, C. J. *Can. Mineral.* **45**, 665 (2007).

[187] Caracas, R. and Gonze, X. *Phys. Chem. Miner.* **32**, 295 (2005).

[188] Vadapoo, R., Krishnan, S., Yilmaz, H., and Marin, C. *Nanotechnology* **22**, 175705 (2011).

[189] Zhai, T., Ye, M., Li, L., Fang, X., Liao, M., Li, Y., Koide, Y., Bando, Y., and Golberg, D. *Adv. Mater.* **22**, 4530 (2010).

[190] Ivanova, Z., Cernoskova, E., Vassilev, V., and Boycheva, S. *Mater. Lett.* **57**, 1025 (2003).

[191] Chen, Y. L., Chu, J.-H., Analytis, J. G., Liu, Z. K., Igarashi, K., Kuo, H.-H., Qi, X. L., Mo, S. K., Moore, R. G., Lu, D. H., Hashimoto, M., Sasagawa, T., Zhang, S. C., Fisher, I. R., Hussain, Z., and Shen, Z. X. *Science* **329**, 659 (2010).

[192] Liu, W., Peng, X., Tang, C., Sun, L., Zhang, K., and Zhong, J. *Phys. Rev. B* **84**, 245105 (2011).

[193] Efthimiopoulos, I., Zhang, J., Kucway, M., Park, C., Ewing, R. C., and Wang, Y. *Sci. Rep.* **3**, 2665 (2013).

[194] Wang, L.-L. and Johnson, D. D. *Phys. Rev. B* **83**, 241309 (2011).

[195] Xu, H., Chen, G., Jin, R., Chen, D., Pei, J., and Wang, Y. *CrystEngComm* **15**, 5626 (2013).

[196] Bland, J. A. and Basinski, J. S. *Can. J. Phys.* **39**, 1040 (1961).

[197] Kristukat, C. *Peak-o-mat 1.1.9* (2013). curve fitting program.

[198] Richter, R. and Becker, C. R. *Phys. Stat. Sol. (b)* **84**, 619 (1977).

[199] Fang, L., Jia, Y., Miller, D. J., Latimer, M. L., Xiao, Z. L., Welp, U., Crabtree, G. W., and Kwok, W.-K. *Nano Lett.* **12**, 6164 (2012).

[200] Park, W. I., Zheng, G., Jiang, X., Tian, B., and Lieber, C. M. *Nano Lett.* **8**, 3004 (2008).

[201] Sheehan, P. E. and Whitman, L. J. *Nano Lett.* **5**, 803 (2005).

[202] Peng, K., Parkinson, P., Fu, L., Gao, Q., Jiang, N., Guo, Y.-N., Wang, F., Joyce, H. J., Boland, J. L., Tan, H. H., Jagadish, C., and Johnston, M. B. *Nano Lett.* **15**, 206 (2015).

[203] Andzane, J., Kunakova, G., Charpentier, S., Hrkac, V., Kienle, L., Baitimirova, M., Bauch, T., Lombardi, F., and Erts, D. *Nanoscale* **7**, 15935 (2015).

[204] Goldsmid, H. J. *Proc. Phys. Soc.* **71**, 633 (1958).

[205] Hamdou, B., Beckstedt, A., Kimling, J., Dorn, A., Akinsinde, L., Bäler, S., Pippel, E., and Nielsch, K. *Nanotechnology* **25**, 365401 (2014).

[206] Kojda, D., Mitdank, R., Weidemann, S., Mogilatenko, A., Wang, Z., Ruhhammer, J., Kroener, M., Töllner, W., Woias, P., Nielsch, K., and Fischer, S. F. *Phys. Stat. Sol. (a)* **213**, 557 (2016).

[207] Biswas, S. and Bhattacharya, R. *Phys. Stat. Sol. (a)* **114**, 277 (1989).

[208] Chi, H., Liu, W., Sun, K., Su, X., Wang, G., Lošťák, P., Kucek, V., Drašar, C., and Uher, C. *Phys. Rev. B* **88**, 045202 (2013).

[209] Wang, Y., Xiu, F., Cheng, L., He, L., Lang, M., Tang, J., Kou, X., Yu, X., Jiang, X., Chen, Z., Zou, J., and Wang, K. L. *Nano Lett.* **12**, 1170 (2012).

[210] Ning, W., Du, H., Kong, F., Yang, J., Han, Y., Tian, M., and Zhang, Y. *Sci. Rep.* **3**, 1564 (2013).

[211] Hamdou, B., Gooth, J., Dorn, A., Pippel, E., and Nielsch, K. *Appl. Phys. Lett.* **103**, 193107 (2013).

[212] Fu, L. and Kane, C. L. *Phys. Rev. Lett.* **100**, 096407 (2008).

[213] Adam, A. *Mater. Res. Bull.* **42**, 1986 (2007).

[214] Kushwaha, S. K., Gibson, Q. D., Xiong, J., Pletikosic, I., Weber, A. P., Fedorov, A. V., Ong, N. P., Valla, T., and Cava, R. J. *J. Appl. Phys.* **115**, 143708 (2014).

[215] Zhang, Y., Xu, J., Xu, P., Zhu, Y., Chen, X., and Yu, W. *Nanotechnology* **21**, 285501 (2010).

[216] Dobrokhotov, V. V., McIlroy, D. N., Norton, M. G., Abdelrahaman, R., Safir, A., and Berven, C. A. *Nanotechnology* **20**, 135504 (2009).

[217] Wang, Y.-Q., Wu, X., Wang, Y.-L., Shao, Y., Lei, T., Wang, J.-O., Zhu, S.-Y., Guo, H., Zhao, L.-X., Chen, G.-F., Nie, S., Weng, H.-M., Ibrahim, K., Dai, X., Fang, Z., and Gao, H.-J. *Adv. Mater.* **28**, 5013 (2016).

[218] Neupane, M., Xu, S.-Y., Sankar, R., Alidoust, N., Bian, G., Liu, C., Belopolski, I., Chang, T.-R., Jeng, H.-T., Lin, H., Bansil, A., Chou, F., and Hasan, M. Z. *Nature Comms.* **5**, 3786 (2014).

[219] Liang, T., Gibson, Q., Ali, M. N., Liu, M., Cava, R. J., and Ong, N. P. *Nat. Mater.* **14**, 280 (2014).

[220] Schlom, D. G. and Pfeiffer, L. N. *Nat. Mater.* **9**, 881 (2010).

[221] Steigman, G. A. and Goodyear, J. *Acta Crystallogr. Sect. B* **24**, 1062 (1968).

[222] Jandl, S., Desgreniers, S., Carlone, C., and Aubin, M. J. *J. Raman Spectros.* **15**, 137 (1984).

[223] Weszka, J., Renucci, M., and Zwick, A. *Phys. Stat. Sol. (b)* **133**, 57 (1986).

[224] Narayanan, A., Watson, M. D., Blake, S. F., Bruyant, N., Drigo, L., Chen, Y. L., Prabhakaran, D., Yan, B., Felser, C., Kong, T., Canfield, P. C., and Coldea, A. I. *Phys. Rev. Lett.* **114**, 117201 (2015).

[225] Zhang, E., Liu, Y., Wang, W., Zhang, C., Zhou, P., Chen, Z.-G., Zou, J., and Xiu, F. *ACS Nano* **9**, 8843 (2015).

[226] Bardeen, J. and Brattain, W. H. *Phys. Rev.* **74**, 230 (1948).

[227] Bosi, M. and Attolini, G. *Prog. Cryst. Growth Charact. Mater.* **56**, 146 (2010).

[228] Ahn, Y. H. and Park, J. *Appl. Phys. Lett.* **91**, 162102 (2007).

[229] Wang, D., Wang, Q., Javey, A., Tu, R., Dai, H., Kim, H., McIntyre, P. C., Krishnamohan, T., and Saraswat, K. C. *App. Phys. Lett.* **83**, 2432 (2003).

[230] Jacoboni, C., Nava, F., Canali, C., and Ottaviani, G. *Phys. Rev. B* **24**, 1014 (1981).

[231] Simanullang, M., Usami, K., Kodera, T., Kawano, Y., and Oda, S. *J. Crys. Growth* **384**, 77 (2013).

[232] Simanullang, M., M. Wisna, G. B., Usami, K., Cao, W., Kawano, Y., Banerjee, K., and Oda, S. *J. Mater. Chem. C* **4**, 5102 (2016).

[233] Zakharov, N. D., Werner, P., Gerth, G., Schubert, L., Sokolov, L., and Gösele, U. *J. Crys. Growth* **290**, 6 (2006).

[234] Schmidtbauer, J., Bansen, R., Heimburger, R., Teubner, T., and Boeck, T. *J. Crys. Growth* **406**, 36 (2014).

C List of figures

D List of tables

E Publications

1. Schönherr, P., Tilbury, T., Wang, H., Haghighirad, A. A., Srot, V., Aken, P. A. van, and Hesjedal, T. *Step-flow growth of Bi_2Te_3 nanobelts* Cryst. Growth. Des. **16**, 6961 (2016).

2. Schönherr, P. and Hesjedal, T. *One-step SnO_2 nanotree growth.* Chem. Eur. J. **22**, 13823 (2016).

3. Schönherr, P., Zhang, F., Kojda, D., Mitdank, R., Fischer, S., and Hesjedal, T. *Free-standing millimetre-long Bi_2Te_3 sub-micron belts catalyzed by TiO_2 nanoparticles.* Nanoscale Res. Lett. **11**, 308 (2016).

4. Srot, V., Schönherr, P., Bussmann, B., Harrison, S. E., van Aken, P. A., and Hesjedal, T. *High Resolution STEM Study of Dy-doped Bi_2Te_3 Thin Films.* Microsc. Microanal. **22**, 1516 (2016).

5. Schönherr, P. and Hesjedal, T. *Structural properties and growth mechanism of Cd_3As_2 nanowires.* Appl. Phys. Lett. **106**, 13115 (2015).

6. Schönherr, P., Zhang, S., Liu, Y., Kusch, P., Reich, S., Giles, T., Daisenberger, D., Prabhakaran, D., Chen, Y., and Hesjedal, T. *A new topological insulator built from quasi one-dimensional atomic ribbons.* Phys. Stat. Sol. RRL **9**, 130 (2015).

7. Harrison, S. E., Collins-McIntyre, L. J., Schönherr, P., Vailionis, A., Srot, V., van Aken, P. A., Kellock, A. J., Pushp, A., Parkin, S. S. P., Harris, J. S., Zhou, B., Chen, Y. L., and Hesjedal, T. *Massive Dirac fermion observed in lanthanide-doped topological insulator thin films.* Sci. Rep. **5**, 15767 (2015).

8. Schönherr, P., Prabhakaran, D., Jones, W., Dimitratos, N., Bowker, M., and Hesjedal, T. *Comparison of Au and TiO_2 based catalysts for the synthesis of chalcogenide nanowires.* Appl. Phys. Lett. **104**, 253103 (2014).

9. Schönherr, P., Collins-McIntyre, L. J., Zhang, S., Kusch, P., Reich, S., Giles, T. Daisenberger, D., Prabhakaran, D., and Hesjedal, T. *Vapour-liquid-solid growth of ternary Bi_2Se_2Te nanowires.* Nanoscale Res. Lett. **9**, 127 (2014).

10. Schönherr, P., Baker, A. A., Kusch, P., Reich, S., and Hesjedal, T. *Engineering of Bi_2Se_3 nanowires by laser cutting.* Eur. Phys. J. Appl. Phys. **66**, 10401 (2014).

11. Figueroa, A. I., van der Laan, G., Collins-McIntyre, L. J., Zhang, S.-L., Baker, A. A., Harrison, S. E., Schönherr, P., Cibin, G., and Hesjedal, T. *Magnetic Cr doping of Bi_2Se_3: evidence for divalent Cr from x-ray spectroscopy.* Phys. Rev. B **90**, 134402 (2014).

12. Collins-McIntyre, L. J., Harrison, S. E., Schönherr, P., Steinke, N.-J., Kinane, C. J., Charlton, T. R., Alba-Veneroa, D., Pushp, A., Kellock, A. J., Parkin, S. S. P., Harris, J. S., Langridge, S., Laan, G. van der, and Hesjedal, T. *Magnetic ordering in Cr-doped Bi_2Se_3 thin films.* EPL **107**, 57009 (2014).

13. Harrison, S. E., Schönherr, P., Huo, Y., Harris, J. S., and Hesjedal, T. *Catalyst-free growth of Bi_2Te_3 nanostructures by molecular beam epitaxy.* Appl. Phys. Lett. **105**, 153114 (2014).

F Acknowledgements

Professor Thorsten Hesjedal has constantly supported me in framing my research goals on *quantum materials* nanowire growth. On top of a wealth of experience and technical knowledge he has a creative spirit, a remarkably tolerant attitude to failure, and is exceptionally generous with his time spent with his students. I would also like to thank my examiners Professor Michael Johnston (University of Oxford) and Dr Vlado Lazarov (University of York).

I came into a very young group when I started at Oxford and enjoyed the entrepreneurial atmosphere leading to a variety of internal and external collaborations and contributions to this thesis.

Oxford Thin Film Quantum Materials Group: Thanks to my colleagues Dr Alexander Baker for critical proof-reading, conversational training, and countless lifts home from the lab; Dr Liam Collins-McIntyre for a jolly good time; and Dr Shilei Zhang for crazy beamtimes. Thanks also to my students Fengyu Zhang (Princeton University) for excellent work on Sn-doped Bi_2Te_3, Thomas Tilbury (University of Oxford) for his work on the growth mechanism, and Haobei Wang (Brown University) for systematic growth studies.

Clarendon laboratory: Thanks to Dr Amir Abbas Haghighirad for discussions, Dr Arjun Narayanan for electronic transport measurements, Dr Dharmalingam Prabhakaran for precursor crystal growth, Dr Hannah Joyce for mentoring, Dr Jack Alexander-Webber for training on electronic transport measurements, Dr Jason Brown for cleanroom training, Dr Jessica Boland and team for terahertz spectroscopy measurements, Dr Jian Huang for wirebonder training, Niels Schröter for proof reading, Professor Yulin Chen for angle-resolved photoelectron spectroscopy measurements, and Office 103.2 (Drs Ani Nersisyan, Einar Magnússon, Francesca Foronda, Michael Peterer, and Riccardo Manenti) for fantastic trips to the countryside.

Collaborators: A detailed list of collaborators can be found in Table F .1. Thanks to Dr Danny Kojda (Humboldt Universität zu Berlin), Dr Roman Giraud (Leibniz-Institut für Festkörper- und Werkstoffforschung Dresden), Angadjit Singh (University of Cambridge) and their teams for electronic transport measurements, Dr Dominik Daisenberger and team (Diamond Light Source) for help with x-ray diffraction measurements, Dr Kay Sowoidnich and team (RCaH) for help with Raman spectroscopy measurements and proof reading, Patryk Kusch and team (Freie Universität Berlin) for Raman spectroscopy measurements, Dr Sara Harrison (Stanford University) for nanowire samples, Dr Vesna Srot and team (Stuttgart Center for Electron Microscopy) for electron microscopy measurements, Dr Wilm Jones and team (UK Catalysis Hub) for providing catalyst solutions, and Professor Stanley Botchway (RCaH) for being open for new collaborations in the life sciences.

Thanks also to Patrick Meyer Higgins (University of Oxford) who has kindly provided the photos used for the cover pages of Chapter 1,Chapter 2, Chapter 3, Chapter 5, and Chapter 7. The aerial shot for Chapter 6 is at the courtesy of STFC by Stephen Kill.

Funding: Thanks to Corinna Dahnke (University of Oxford) for help with funding, Corpus Christi College (University of Oxford) for generous scholarships, Dr Amalia Coldea (University of Oxford) for mentoring and three months research work, Dr Hrand Mamigonian (Zedsen) for a two month consulting project, EPSRC (UK) for funding my study fees, ESTEEM2 for partly funding my journeys to Stuttgart, and the German *Studienstiftung* for their initial bursary.

Meine Eltern und meine Partnerin haben mich kontinuierlich unterstützt und zum Spaß an dieser Arbeit erheblich beigetragen. Danke für alles.

Table F .1: List of experimenters who contributed to this thesis.

Reference	Description	Experimenter	Location
Fig. 3.2.2	sample preparation and imaging	Ulrike Eigenthaler	MPI IS, Stuttgart, Germany
Fig. 4.1.3(b)	sample preparation	Ulrike Eigenthaler	MPI IS, Stuttgart, Germany
Fig. 4.1.3(b)	imaging	Dr Vesna Srot	StEM, Stuttgart, Germany
Fig. 4.2.6(c)	sample preparation and imaging	Ulrike Eigenthaler	MPI IS, Stuttgart, Germany
Fig. 4.2.6(d,e)	sample preparation	Ulrike Eigenthaler	MPI IS, Stuttgart, Germany
Fig. 4.2.6(d,e)	imaging	Dr Vesna Srot	StEM, Stuttgart, Germany
Fig. 4.2.9(e)	imaging	Thomas Tilbury	RCaH, Didcot, UK
Section 4.3	sample growth	Dr Sara Harrison	Stanford University, California, US
Fig. 4.3.1	imaging	Dr Sara Harrison	Stanford University, California, US
Fig. 4.3.4(a,b,d)	imaging	Dr Sara Harrison	Stanford University, California, US
Fig. 5.2.3	help with experiment	Dr Patryk Kusch	Freie Universität Berlin, Germany
Fig. 5.2.4	sample preparation and experiment	Professor Yulin Chen	Elettra Sincrotrone Trieste, Italy
Fig. 6.1.3(a)	help with experiment	Dr Patryk Kusch	Freie Universität Berlin, Germany
Fig. 6.2.1(a)	imaging	Fengyu Zhang	RCaH, Didcot, UK
Fig. 6.2.2	imaging	Fengyu Zhang	RCaH, Didcot, UK
Fig. 6.2.3	imaging	Fengyu Zhang	RCaH, Didcot, UK
Fig. 6.2.4(a,b)	imaging and EDS	Fengyu Zhang	RCaH, Didcot, UK
Section 6.2.3	experiment and data analysis	Dr Danny Kojda	Humboldt Universität zu Berlin, Germany
Fig. 6.3.2(b)	imaging	Ulrike Eigenthaler	MPI IS, Stuttgart, Germany
Fig. 6.3.2(e,f)	sample preparation	Ulrike Eigenthaler	MPI IS, Stuttgart, Germany
Fig. 6.3.2(e)	imaging	Dr Vesna Srot	StEM, Stuttgart, Germany
Fig. 6.3.2(f)	imaging and EDS	Dr Vesna Srot	StEM, Stuttgart, Germany
Fig. 6.3.2(g)	EDS	Dr Vesna Srot	StEM, Stuttgart, Germany
Fig. 7.1.2(c)	help with experiment	Dr Patryk Kusch	Freie Universität Berlin, Germany
Fig. 7.2.2	measurement and data analysis	Dr Jessica Boland	Oxford University, UK

G Glossary

1D	one-dimensional
2D	two-dimensional
3D	three-dimensional
AFM	atomic force microscopy
ARPES	angle-resolved photoemission spectroscopy
CVD	chemical vapour deposition
EDS	energy-dispersive x-ray spectroscopy
FIB	focused ion beam
HSA	high surface area anatase
MBE	molecular beam epitaxy
P-25	catalyst mixture from TiO_2 nanoparticles
PLL	poly-L-lysine
SEM	scanning electron microscope
STEM	scanning transmission electron microscopy
TEM	transmission electron microscopy
THz	terahertz
TI	topological insulator
TSS	topological surface state
VLS	vapour-liquid-solid
XRD	x-ray diffraction